

SUPERCONDUCTIVITY, MAGNETISM AND TOPOLOGICAL PROPERTIES OF
SEVERAL QUASI-1D MATERIALS

by

Xiaoyuan Liu

APPROVED BY SUPERVISORY COMMITTEE:

Bing Lv, Chair

Robert Glosser

Lindsay J. King

Xiaoyan Shi

Fan Zhang

Copyright 2020

Xiaoyuan Liu

All Rights Reserved

To my parents

SUPERCONDUCTIVITY, MAGNETISM AND TOPOLOGICAL PROPERTIES OF
SEVERAL QUASI-1D MATERIALS

by

XIAOYUAN LIU, BS, MS

DISSERTATION

Presented to the Faculty of
The University of Texas at Dallas
in Partial Fulfillment
of the Requirements
for the Degree of

DOCTOR OF PHILOSOPHY IN
PHYSICS

THE UNIVERSITY OF TEXAS AT DALLAS

May 2020

ACKNOWLEDGMENTS

I would like to thank the people who helped me to achieve this dissertation with mentorship, advice, and assistance. First and foremost, I would like to express my gratitude to my advisor and mentor, Dr. Bing Lv, for offering me the opportunity and support to pursue higher level education in applied physics. I joined his group when the laboratory was setting up and have been fortunate to be supported as a research assistant in the group. His mentorship and advice in research have been significant to me. I would also like to express my gratitude to Dr. Sheng Li, as a friend and colleague, for teaching me the operation of lab equipment and experimental techniques. I would also like to thank my other group members: Hanlin Wu, Wenhao Liu, Huifei Zhai, Nikhil Dhale, Pawan Koirala, Aswin Kondusamy, Rashad Kadado, Daniel Peirano, Davis Zackaria, Gareth Ofenstein, and Wyatt Clemons for providing me with guidance and assistance.

I would like to thank Dr. Robert Glosser, Lindsay King, Xiaoyan Shi, Fan Zhang, and Min Chen for serving on my dissertation committee and reviewing my dissertation; and Julie Welch, Phyllis Jean, Barbara Burbey and Amanda Hunter for their administrative work in the physics department.

March 2020

SUPERCONDUCTIVITY, MAGNETISM AND TOPOLOGICAL PROPERTIES OF SEVERAL QUASI-1D MATERIALS

Xiaoyuan Liu, PhD
The University of Texas at Dallas, 2020

Supervising Professor: Bing Lv

This dissertation focuses on the investigation of several material systems with distinct quasi-one-dimensional (quasi-1D) or pseudo-quasi-1D structural features and hosting rather interesting magnetic, superconducting, and topological properties. High quality of powders or single crystals have been synthesized through various methods and carefully characterized through X-ray diffraction, magnetic, electrical transport and thermal transport studies at low temperature and under high magnetic fields. Their unique magnetic, superconducting, and possible topological properties are presented with their future implications further discussed.

Firstly, we investigated the magnetic property and superconductivity in two iron-based chalcogenides with quasi-1D structure: BaFe_2Se_4 and $\text{K}_3\text{Fe}_2\text{Se}_4$. Both compounds consist of 1D chains of iron chalcogenide with FeSe_4 tetrahedra, similar to the fundamental building block FeAs_4 in the iron-based superconductors. However, these FeSe_4 tetrahedra is edge-shared along one specific crystallographic axis and forms 1D chain structure, rather than the two-dimensional layered Fe_2As_2 structure seen in the common iron-based superconductors. X-ray powder pure phases of both compounds are synthesized and found to be semiconducting and magnetic.

Intuitively doping studies based on the nominal iron valence charges are also carried out, however, no superconductivity is detected yet at this stage in the doped samples.

Secondly, we carried out systematical doping studies aiming to induce superconductivity in the Zr_5Ge_3 system with Mn_5Si_3 -type structure and pseudo-quasi-1D Zr_3Ge_3 chain along the c axis. Different transition metal doping at different crystallographic sites in this Zr_5Ge_3 system have been thoroughly investigated. Interestingly, superconductivity was successfully induced through Ru and Pt doping, but only at the Ge site. Superconductivity is found to be absent with same amount of carrier doping at the Zr site or interstitial site. The highest superconducting T_c is found to be at 5.7 K for Ru doping, and 2.8 K for Pt doping. Detailed transport and magnetic studies have suggested bulk superconductivity, high upper critical field, enhanced electron correlation, and extremely small electron-phonon coupling, indicating possible unconventional superconductivity in this system. In addition, we also investigated the superconductivity properties of the $\text{A}_2\text{Mo}_3\text{As}_3$ ($\text{A} = \text{K}, \text{Rb}$), which has a more 1D-like Mo_3As_3 chain structure but structurally very close to the Zr_5Ge_3 compound. The superconducting T_c is ~ 10.6 K, and the electrical transport studies suggested a much higher upper critical field ~ 27 T, exceeding the Pauli limit based on conventional criteria. Thirdly, we present a study of synthesis and crystal growth of $\alpha, \beta\text{-Bi}_4\text{X}_4$ ($\text{X} = \text{I}, \text{Br}$) materials with different stacking of 1D BiX chains and various interesting topological properties. Different types of synthetic methods have been tested for the high quality crystal growth, and crystals as large as 8 mm size of Bi_4X_4 was successfully synthesized. A hypothetical growth mechanism was proposed for Bi_4Br_4 . The transport measurements have revealed a topological phase transition from $\beta\text{-Bi}_4\text{I}_4$ as a strong topological insulator to $\alpha\text{-Bi}_4\text{I}_4$ with high ordered hinge states around room temperature at 300 K. The exact origin of several transport anomaly in the $\alpha\text{-Bi}_4\text{I}_4$ and $\alpha'\text{-Bi}_4\text{Br}_4$ remain elusive

at this stage. Single crystals of mixed $\text{Bi}_4\text{I}_{4-x}\text{Br}_x$ ($0.1 \leq x \leq 3$) were also synthesized and a rather interesting structural transformations upon Br doping have been observed, and further studies are needed to fully understand the topological phase transitions in this system. Last but not least, chemical intercalation studies were also carried out, and preliminary data suggests superconductivity is successfully induced in these materials.

The last part of this dissertation focus on a two-dimensional material Black phosphorus (Black-P). We carried out thorough experimental studies to investigate the growth mechanism for Black-P aiming to facilitate its future layer-by-layer thin film growth. A new synthetic strategy to grow large size of Black-P crystals through a ternary clathrate $\text{Sn}_{24}\text{P}_{22-x}\text{I}_8$ under lower temperature and pressure was reported. The chemical vapor transport mechanism was found not play a critical role for the growth of Black-P, but rather the vapor-solid-solid (VSS)-like growth mechanism is found to be crucial for the quality growth. The ternary clathrate $\text{Sn}_{24}\text{P}_{22-x}\text{I}_8$ acts as the solid catalyst and the P vacancies in $\text{Sn}_{24}\text{P}_{22-x}\text{I}_8$ was found plays an important role in this mechanism.

TABLE OF CONTENTS

ACKNOWLEDGMENTS	v
ABSTRACT	vi
LIST OF FIGURES	x
LIST OF TABLES	xv
CHAPTER 1 GENERAL INTRODUCTION	1
CHAPTER 2 MATERIALS SYNTHESIS AND CHARACTERIZATION TOOLS	15
CHAPTER 3 MAGNETISM IN SEVERAL COMPLEX QUASI-1D IRON CHALCOGENIDES SYSTEMS.....	28
CHAPTER 4 SUPERCONDUCTIVITY IN QUASI-1D ZR_5GE_3 AND $A_2MO_3AS_3$ (A=K, RB) SYSTEMS	43
CHAPTER 5 SYNTHESIS AND CRYSTAL GROWTH OF QUASI-1D TOPOLOGICAL BI_4X_4 (X=I, BR) MATERIALS.....	65
CHAPTER 6 MECHANISM AND FILM GROWTH FOR 2D MATERIAL BLACK PHOSPHORUS.....	76
CHAPTER 7 GENERAL CONCLUSIONS AND FUTURE PROSPECTS	92
REFERENCES	97
BIOGRAPHICAL SKETCH	108
CURRICULUM VITAE	

LIST OF FIGURES

1.1	The M-H diagram of Type-I and II superconductors, type-I superconductor has one critical field H_c , while type-II superconductor has two critical field H_{c1} and H_{c2}	3
1.2	The individual type family of Fe-based superconductors is defined by the different layer which separates the FePn_4 tetrahedra layers: (a) 1111-type, separated by positively single tetrahedra LnO or LaF layers (b) 122-type, separated by a single layer of alkaline earth metal (c) 111-type, separated by double layers of alkali metals (d) 11-type, with no separating layers.	5
1.3	The inverse of χ as a function of T for Paramagnetic, Antiferromagnetic, and Ferromagnetic materials, their x intercept is 0, T_N , and T_c , respectively.	11
2.1	Photos of different container used in this work: (a) silica quartz tube (b) alumina crucible (c) Nb tube closed on one side.	15
2.2	Photos of the furnace used in this work (a) tube furnace (b) box furnace.	18
2.3	Scheme of chemical vapor transport reaction for crystals growth in a temperature gradient.	20
2.4	Photo of the arc melting unit used in this work.	21
2.5	Photo of the Rigaku SmartLab XRD diffractometer used in this work.	22
2.6	Photo of the PPMS (Quantum Design) used in this work.	25
2.7	Photo of the MPMS (Quantum Design) used in this work.	26
3.1	Crystal Structure of (a) layered $\text{K}_x\text{Fe}_2\text{Se}_2$ compound (b) quasi-1D BaFe_2Se_3 compound. Both compounds consist of edge sharing FeSe_4 tetrahedra, forming 2D square lattice along ab plane in $\text{K}_x\text{Fe}_2\text{Se}_2$ while 1D double chain along b-axis in BaFe_2Se_3	30
3.2	XRD pattern for (a) BaFe_2Se_4 (b) $\text{K}_3\text{Fe}_2\text{Se}_4$ samples, no impurity was observed within the resolution of the measurement.	34
3.3	Crystal Structure of (a) BaFe_2Se_4 , contains single chain of edge sharing FeSe_4 tetrahedra along the c-axis separated by Ba atoms (b) $\text{K}_3\text{Fe}_2\text{Se}_4$, it contains zig-zag infinite chains of edge sharing FeSe_4 tetrahedra along the b-axis separated by K atoms.	34

3.4	The side view 1D chains of FeSe_4 tetrahedra in (a) BaFe_2Se_4 (b) $\text{K}_3\text{Fe}_2\text{Se}_4$ with respect to b- and c-axis, respectively. The chains are propagated along the c-axis in BaFe_2Se_4 , while the edge sharing FeSe_4 tetrahedra are slightly distorted in $\text{K}_3\text{Fe}_2\text{Se}_4$, forming zig-zag chains propagating along the b-axis.....	35
3.5	Temperature dependence of resistivity on (a) BaFe_2Se_4 and (b) $\text{K}_3\text{Fe}_2\text{Se}_4$ samples. Both samples show insulating behavior. The activation energy extrapolated using Arrhenius temperature dependence equation are ~ 27.5 meV and ~ 239.6 meV for BaFe_2Se_4 and $\text{K}_3\text{Fe}_2\text{Se}_4$, respectively. Insets show 1D VRH behavior at low-temperature regime.....	36
3.6	Magnetic moment as a function of temperature $M(T)$ of BaFe_2Se_4 measured with ZFC and FC methods. Typical irreversible behavior for a ferromagnetic order was observed in $M(T)$ measured with ZFC and FC histories.	38
3.7	Magnetic moment as a function of field $M(H)$ of BaFe_2Se_4 measured at different temperatures from 20 K to 350 K. The magnetic hysteresis loop is suppressed with increasing temperature and eventually disappear and become a straight line when temperature reaches 350 K.	38
3.8	Phase diagram of the electron and hole doped cuprate and iron pnictides superconductors, the parent compounds typically exhibit magnetic ordering near zero doping, superconductivity emerges through either electrons or holes doping.	41
3.9	Superconducting phase diagram of KFe_2As_2 , Chemical doping that changes the Fe oxidation state to 2.75+ (hole doping) or 2.25+ (electron doping) has the highest possibility to make the compound superconducting.	41
3.10	XRD patterns of doped samples (a) $\text{Ba}_{0.5}\text{Ce}_{0.5}\text{Fe}_2\text{Se}_4$, the impurity phase was identified as CeSe_2 (*) (b) $\text{Ba}_{0.5}\text{Eu}_{0.5}\text{Fe}_2\text{Se}_4$, the impurities are EuSe (#) and few unidentified peaks (c) $\text{K}_{2.5}\text{Ba}_{0.5}\text{Fe}_2\text{Se}_4$, the impurity phase was identified as Base (*).....	42
3.11	Normalized temperature dependence of resistivity on doped samples (a) $\text{Ba}_{0.5}\text{Ce}_{0.5}\text{Fe}_2\text{Se}_4$, $\text{Ba}_{0.5}\text{Eu}_{0.5}\text{Fe}_2\text{Se}_4$ (c) $\text{K}_{2.5}\text{Ba}_{0.5}\text{Fe}_2\text{Se}_4$	42
4.1	Projection of Zr_5Ge_3 structure along c directions. The small green circles at the corners of the unit cell show the octahedral interstitial 2b site formed by the trigonal antiprismatic Zr_6Ge_6 chain.....	45
4.2	XRD patterns for four samples, small impurity peaks are marked by blue stars (as ZrGe_2) for Zr_5Ge_3 sample and red stars (as ZrRuGe) for Ru-doped Zr_5Ge_3 samples.	46
4.3	The normalized temperature dependent resistivity data for four different samples with a clear superconducting transition at 5.7 K observed in the $\text{Zr}_5\text{Ge}_{2.5}\text{Ru}_{0.5}$ sample. Two dotted straight lines were used as the guidance to compare normal state temperature dependence resistivity changes upon doping for parent Zr_5Ge_3 and doped $\text{Zr}_5\text{Ge}_{2.5}\text{Ru}_{0.5}$ samples.	49

4.4	(a) Temperature dependence of the DC magnetization measured in the ZFC mode and the FC mode at 10Oe. (b) The MH Loop measured with a field sweeping rate of 50 Oe/s at 2 K, which shows a type-II superconductor behavior.	49
4.5	Temperature dependence of resistivity at different magnetic fields: 0, 0.5, 1.0, 2.0, 3.0, 4.0, 5.0, 6.0, and 7.0 T. The inset shows the WHH fitting of the temperature dependence of the critical field with $H_{c2}(T)$ ($90\%\rho_n$), where the straight line shows the Pauli limitation.	50
4.6	Field dependence of the heat capacity data, the inset shows the electronic specific data.	51
4.7	XRD patterns for (a) Zr_5Ge_3 , (b) $Zr_5Ge_{2.5}Pt_{0.5}$, (c) $Zr_5Ge_{2.5}Ir_{0.5}$, and (d) $Zr_5Ge_{2.5}Pd_{0.5}$ samples. The small impurity peaks are marked by * (as $ZrGe_2$) in Zr_5Ge_3 sample, and # (as $ZrPd$ phase) for $Zr_5Ge_{2.5}Pd_{0.5}$ sample.....	53
4.8	Normalized temperature dependent resistivity data for different transition metal doped $Zr_5Ge_{3-x}M_x$ samples where only a Pt doped sample shows a superconducting behavior, (b) normalized temperature dependent resistivity data for different doped Zr_5Ge_3 samples with the same Pt amount but at a different site.	53
4.9	(a) Normalized temperature dependent resistivity data for Pt doped $Zr_5Ge_{3-x}Pt_x$ samples with different doping level ($x=0, 0.2, 0.5$ and 1.0); (b) the superconducting transition for different samples on an enlarged scale between 1 and 5K; (c) magnetization measurement data in ZFC and FC modes at 10 Oe for the $Zr_5Ge_{2.5}Pt_{0.5}$ sample, the inset shows the M-H loop at 1.8 K, (d) superconducting phase diagram of $Zr_5Ge_{3-x}Pt_x$. The superconductivity might already be induced in the gradient yellow area ($x < 0.2$), with T_c below 2 K which is below our lowest measurable temperature.	54
4.10(a)	Field dependence resistivity data at low temperature for $Zr_5Ge_{2.5}Pt_{0.5}$ sample, and (b) the upper critical field $H_{c2}(T)$ and its fitting by the WHH theory.	56
4.11(a)	Heat capacity data of $Zr_5Ge_{2.5}Pt_{0.5}$ sample at different magnetic field where a clear specific heat jump is visible below 3 K at zero-field; (b) the difference of electronic specific heat data between the normal state and superconducting state of $Zr_5Ge_{2.5}Pt_{0.5}$ sample.	56
4.12	Crystal structure of (a) Zr_5Ge_3 (b) $K_2Mo_3As_3$ (c) $K_2Mo_6Se_6$ (d) $PbMo_6S_6$. Zr_5Ge_3 , $K_2Mo_3As_3$, and $K_2Mo_6Se_6$ all adopt very similar hexagonal quasi-1D structure, which can be transformed from the crystal structure of well-known Chevrel phases.	58
4.13	XRD patterns of $K_2Mo_3As_3$ and $Rb_2Mo_3As_3$ samples.....	61
4.14	Temperature dependence of the DC magnetization measured in the ZFC and FC mode at 10 Oe for (a) $K_2Mo_3As_3$ (b) $Rb_2Mo_3As_3$ samples.	62

4.15	The temperature dependence of resistance for $\text{Rb}_2\text{Mo}_3\text{As}_3$ compound, clear superconducting transition can be observed at $T_c \sim 10.6$ K. The inset of figure shows the four-probe technique for the resistance measurement.	63
4.16	(a) The temperature dependence of resistivity at different fields from 0 T to 9 T with 1 T interval. (b) the WHH fitting of the temperature dependence of the critical field with $H_{c2}(T)$ ($90\% \rho_n$), where the straight line shows the Pauli limitation.	64
5.1	Crystal structure of (a) α - Bi_4I_4 , (b) β - Bi_4I_4 and (c) α - Bi_4Br_4 , both are composed of 1D molecular chains long b-axis held together by weaker non-covalent interactions. α -, β - Bi_4I_4 are consist of packing of normal single layer, while combined packing of normal and mirror-reflected single layer along c-axis in α - Bi_4Br_4	69
5.2	Photos of typical size (a) β - Bi_4I_4 and (b) α - Bi_4Br_4 crystals.	69
5.3	XRD pattern of obtained β - Bi_4I_4 crystal. The main diffraction peaks can be indexed as the (00l) preferred orientation of β - Bi_4I_4	69
5.4	Temperature dependence of the electrical resistivity for Bi_4I_4 and α - Bi_4Br_4 crystals along the chain direction. A hysteresis was observed around 300 K for Bi_4I_4 , showing the phase transition between α - Bi_4I_4 and β - Bi_4I_4 . (c) temperature dependence of the electrical resistivity for Bi_4I_4 from [52]. (d) the hysteresis around 300 K from [52].	71
5.5	(a) Photo of typical size $\text{Bi}_4\text{I}_3\text{Br}$ crystal. (b) EDAX spectrum for $\text{Bi}_4\text{I}_3\text{Br}$ crystal.	73
5.6	Temperature dependence of the electrical resistivity for $\text{Bi}_4\text{I}_{3.9}\text{Br}_{0.1}$ crystal. A hysteresis was observed around 320 K.	74
5.7	Temperature dependence of dc magnetization from 2 K to 3 K for Li intercalated (a) Bi_4I_4 and (b) α - Bi_4Br_4 crystals. A clear superconducting transition can be observed at 2.45 K and 2.5 K for Bi_4I_4 and α - Bi_4Br_4 , respectively.	75
6.1	Crystal structure of Black-P. (a) Side view of the Black-P crystal lattice. The interlayer spacing is 5.3 Å. (b) Top view of the lattice of single-layer Black-P. x and z correspond to the zigzag and armchair directions of Black-P.	77
6.2	The mobility/on-off ratio spectrum of nanomaterials with corresponding performance regions indicated for Graphene, Black-P and TMDs. The shaded regions are the approximate possible ranges of performance reported for the respective materials in the literature.	78
6.3	Crystal structure of $\text{Sn}_{24}\text{P}_{22-x}\text{I}_8$. (a) Pentagonal dodecahedra and tetrakaidekahedron framework formed by Sn and P atoms in the clathrate $\text{Sn}_{24}\text{P}_{22-x}\text{I}_8$, where two different types of I atoms (2a and 6d) are located at the centers of each polyhedron. (b, c) The crystal structure of $\text{Sn}_{24}\text{P}_{22-x}\text{I}_8$, where the vacancy □ caused by partially occupied P2 atom is highlighted.	85

6.4 Hypothesis for three different growth models for Black-P crystal growth.....	86
6.5 Photo of Black-P crystals in the ampule tube grown directly from ternary $\text{Sn}_{24}\text{P}_{22-x}\text{I}_8$ compound; (b) enlarged view of Black-P crystals on the mm scale. (c) Top view of SEM image of selected crystals showing ribbon-sharp morphology; (d) side view of SEM image showing the layered nature of the grown crystal. (e) XRD patterns, and (f) Raman spectrum of the grown Black-P crystals.	89
6.6 Proposed growth mechanism. The orange part represents the ternary compound of $\text{Sn}_{24}\text{P}_{22-x}\text{I}_8$; the black part represents Black-P; the purple dots represent P atoms; the colorful dots represent P vacancies; the green dots represent I atoms; and gray dots represent Sn atoms. The green arrows indicate the possible diffusion path of P atoms with the assistance of P vacancies. ...	91
7.1 The preliminary result of dc magnetic susceptibility measurement for Si-added $\text{Zr}_5\text{Ge}_{2.5}\text{Ru}_{0.5}\text{Si}_{0.5}$ compound. The transition temperature was enhanced from 5.7 K to 9.2 K.	95

LIST OF TABLES

2.1 List of all the chemicals used in this dissertation.	17
4.1 Rietveld refinement data of the four samples.	47
5.1 Normalized formula for mixed $\text{Bi}_4\text{I}_{4-x}\text{Br}_x$ crystals obtained from EDAX. $\beta\text{-Bi}_4\text{I}_4$ and $\alpha\text{-Bi}_4\text{Br}_4$ crystals were used as standard.	73
6.1 Control experiments for the investigation of the necessity of chemicals.	81
6.2 Control experiments for further investigation of the necessity of chemicals.	82
6.3 Control experiments for the formation of Black-P at different quenching temperature.	83
6.4 Control experiments for required synthetic temperature.	84
6.5 Control experiments to verify the three different hypothetical growth models for Black-P..	88

CHAPTER 1

GENERAL INTRODUCTION

1.1 Superconductivity

1.1.1 Basic properties of superconductors

In 1911, H. Kamerlingh Onnes discovered the first superconductor in Mercury (Hg) [1]. The resistivity of Hg will suddenly drop to zero when the temperature was cooled down below 4 K. The temperature that a material becoming superconducting is called superconducting transition temperature T_c . In the superconducting state, electrical current can flow through superconductors with zero energy losses, the upper limit for current that would flow at zero resistivity is called the critical current J_c [2]. Below the transition temperature, superconductors have the ability to exclude the external magnetic field, which was characterized as the Meissner effect [3]. Above the critical field H_c , the superconductor will lose its superconductivity and become normal metal [2]. Such interesting properties make superconductors very promising material and a great candidate for application in many areas, such as magnets for Magnetic Resonance Imaging (MRI), low and high field magnets for Nuclear Magnetic Resonance (NMR), low and high field magnets for physical research, accelerators for high-energy physics, the field of power supply and high speed transportation.

Depends on how superconductors react to the external magnetic field, a superconductor can be classified as Type-I or Type-II [2]. The field dependence of magnetization of the type-I and II superconductors are shown in Figure 1.1. The type-I superconductor has a single critical field, the superconductor will lose its superconductivity and become normal metal above the critical field,

while the magnetic field will be expelled from the superconductor below the critical field. By contrast, the type-II superconductor has two critical fields, it allows partial penetration of the magnetic field through some isolated points, which are called mixed state or vortex state in between two critical fields. In the mixed state, there is a phenomenon known as flux pinning, where a superconductor is pinned in space by the magnetic field above a magnet. This phenomenon makes a magnet levitating on a superconductor, there is no direct contact and energy loss, makes superconductor a great candidate for high-speed rail and airplanes. Above the upper critical field H_{c2} , the type-II superconductor will lose its superconductivity and become normal metal. Most of the high-temperature superconductors belong to the type-II superconductors which have attracted a lot of attention from researchers in the past few decades and many compounds in this category have already been synthesized and characterized. Many type-II superconductors were reported exhibiting unconventional superconductivity that cannot be well explained by the Classic BCS Theory (Bardeen-Cooper-Schrieffer) [4], which describes low temperature superconductivity well. In conventional superconductors, superconductivity results from zero interaction between lattice and electron pairs that coupled through electron-phonon coupling, which is called Copper pair [5]. In unconventional superconductors, the Copper pairs are not coupled through electron-phonon coupling but instead of some other kind, such as spin fluctuations. The key interests of superconductors are to find the origin of the superconductivity and materials with higher superconducting transition temperature even the room temperature superconductors. However, the origin of superconductivity with high superconducting transition temperature is still unclear and controversial up to date.

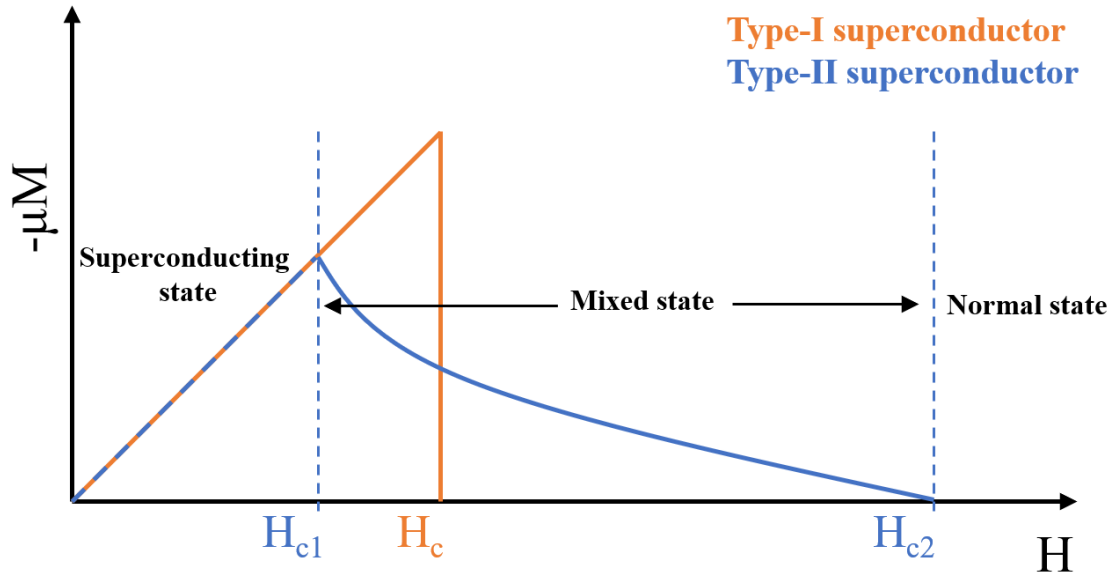


Figure 1.1: The M-H diagram of Type-I and II superconductors, type-I superconductor has one critical field H_c , while type-II superconductor has two critical field H_{c1} and H_{c2} .

1.1.2 Iron-based superconductors

Iron-based superconductors is the second-generation high temperature superconductors after the cuprate superconductors which was discovered back in 1986. One of the most famous cuprate superconductors is the Yttrium barium copper oxide (YBCO) which was discovered by C. W. Chu with his colleagues in 1987 with a high transition temperature of 93 K [6] soon after the discovery of the cuprate superconductor by A. Muller and G. Bednorz [7]. YBCO is the first high temperature superconductor that has transition temperature above the boiling point of liquid nitrogen (77 K). iron-based superconductors are iron-containing compounds whose superconductivity was firstly discovered in 2006 by the Hosono's group, they discovered superconductivity in iron pnictides LaFePO with transition temperature $T_c \sim 4$ K [8]. In 2008, doping fluorine (F) to the oxygen (O) site in LaFeAsO_{1-x}F_x with doping level of $x = 0.12$ could enhance the superconducting temperature to 26 K was reported [9] and 43 K under pressure of ~ 4 GPa [10] and the topic caught world-wide

attention. Superconducting T_c is raised rapidly by different rare earth analogs, with the highest reported T_c up to 55 K in the $\text{SmFeAsO}_{0.9}\text{F}_{0.1}$ [11]. This is exceeding the BCS-limit and further triggered the non-conventional superconductivity research in these iron-based superconductor research. In the same year, superconductivity up to 38K is discovered in a completely different family of 122 phase compounds in $(\text{A}_{1-x}\text{Sr}_x)\text{Fe}_2\text{As}_2$ ($\text{A} = \text{K}, \text{Cs}$) and $\text{Ba}_{0.6}\text{K}_{0.4}\text{Fe}_2\text{As}_2$ simultaneously by two different groups [12,13].

Meanwhile, Superconductivity is discovered in the 111-phase LiFeAs with transition temperature of 18 K [14-16]. Fe-chalcogenide superconductors were also discovered, but with only two phase types, i.e. the 122-phase $(\text{A}_{1-x}\text{Fe}_2\text{Se}_2)$ where $\text{A} = \text{alkaline}$; and the 11-phase (FeSe) with the PbO structure (P4/nmm). FeSe that adopts the simplest structure among all iron-based superconductors was discovered to be superconducting at 8 K [17] and 36.7 K under high pressure [18]. Later on, Alkali metal intercalated FeSe with transition temperature up to 30 K was also reported [19-23]. Moreover, single-layer FeSe films on doped SrTiO_3 was observed exhibiting transition temperature above 65 K [24-29]. These discoveries made the new family of iron pnictide high temperature superconductors to be the most interesting topics back at that time. Within few years of investigation, a lot of superconductors in this family have been discovered.

All iron pnictide superconductors adopt the structure that tetrahedral layers stacked along the c -axis. The tetrahedral layers have the Fe atoms surrounded by 4 pnictide/chalcogenide forming FePn_4 ($\text{Pn} = \text{pnictide}$) or FeCh_4 ($\text{Ch} = \text{Chalcogenide}$) tetrahedra with shared edges in the ab -plane. The layers are separated by different layer which define the individual type family: 1111, 122, 111, and 11-types, the abbreviation of the stoichiometry coefficient for the structure types, as shown in Figure 1.2.

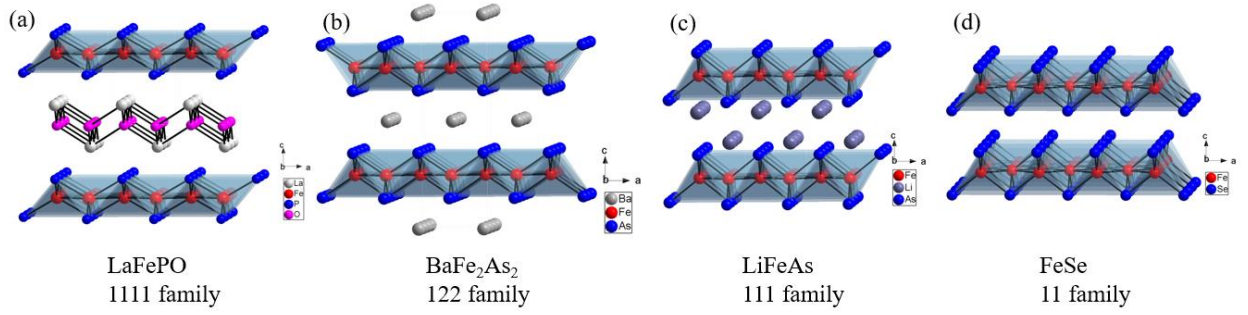


Figure 1.2: The individual type family of iron-based superconductors is defined by the different layer which separates the FePn_4 tetrahedra layers: (a) 1111-type, separated by positively single tetrahedra LnO or LaF layers (b) 122-type, separated by a single layer of alkaline earth metal (c) 111-type, separated by double layers of alkali metals (d) 11-type, with no separating layers.

The crystal structure of 1111-type compounds contain negatively charged tetrahedra FeP or FeAs layers which are separated alternatingly by positively charged tetrahedra LnO or LaF layers and electron are conducting in FeP or FeAs layers. The 1111-type family includes the first iron-based superconductor LaFePO [8], the F doped compound $\text{LaFeAsO}_{1-x}\text{F}_x$ [9], and quite a few compounds with transition temperature higher than 50 K, such as $\text{SmFeAsO}_{0.9}\text{F}_{0.1}$ [11] and GdFeAsO_{1-y} [30].

The crystal structure of 122-type ($\text{K}_{0.4}\text{Sr}_{0.6}\text{Fe}_2\text{As}_2$) and 111-types (LiFeAs) families are simpler than 1111-type family. All three type families contain FeP or FeAs tetrahedra layers but the blocking layer which separates FeP or FeAs is different for each type: single LnO or LnF layer for 1111-type family, single layer of alkali (e.g. K, Rb or Cs) or alkaline earth metal (e.g. Ca, Sr, Ba) for 122-type family, and double layers of alkali metals (e.g. Li, Na) for 111-type. Superconducting transition temperature of 37 K in $\text{K}_{0.4}\text{Sr}_{0.6}\text{Fe}_2\text{As}_2$ and $\text{Cs}_{0.4}\text{Sr}_{0.6}\text{Fe}_2\text{As}_2$ [12], 38 K in $\text{Ba}_{0.6}\text{K}_{0.4}\text{Fe}_2\text{As}_2$ [13], 22 K in $\text{BaFe}_{1.8}\text{Co}_{0.2}\text{As}_2$ [31], and 30 K in $\text{BaFe}_2(\text{As}_{0.68}\text{P}_{0.32})_2$ [32] belong to 122-type family.

The tetrahedral layer was formed by either edge-shared or corner-shared FeAs_4 tetrahedra unit and this unit plays an important role for the appearance of superconductivity in this family. 11-type family contains FeSe with no separating unit between them. Superconducting transition

temperature of 14 K in $\text{FeTe}_{0.5}\text{Se}_{0.5}$ [33], 2 K in $\text{Fe}_{1.13}\text{Te}_{0.85}\text{S}_{0.1}$ [34] and 10 K in $\text{FeTe}_{0.8}\text{S}_{0.2}$ [35] belong to this family.

The iron pnictide/chalcogenide system features a complex interplay of superconductivity, structure distortion, magnetic order and nematic order. The undoped parent compound of iron-based superconductors typically exhibits antiferromagnetic order, which is intimately coupled to a nematic order characterized by electronic in-plane anisotropy and an orthorhombic structural distortion, whereas the high temperature paramagnetic phase is typically tetragonal. The structural transition occurs during cooling followed by the magnetic transition. Superconductivity is induced when structural and magnetic transitions are fully suppressed by chemical doping or pressure. It is commonly believed that two electrons are paired by electron-phonon coupling to form Cooper pairs and are responsible for the conventional superconductivity. But for the unconventional superconductivity, the pairing mechanism is still unsettled and controversial after the intensive investigation in the past few decades, and one commonly accepted pairing mechanism is S^{\pm} -wave pairing driven by the exchange of the antiferromagnetic spin fluctuation.

1.1.3 Superconductivity in quasi-1D system

The high temperature iron-based superconductors is one of the most significant discoveries in modern condensed matter physics. Many materials with unconventional superconductivity were discovered in this family in the past few decades. The common iron-based superconductors adopt quasi-two-dimensional (Quasi-2D) layered structure formed by edge shared FePn_4 or FeCh_4 tetrahedra, which is the fundamental building block in the iron-based superconductors. The correlated d electrons are believed to be essential for the appearance of unconventional superconductivity. As the dimensionality of structure is further decreased to quasi-one-

dimensional (quasi-1D) type, where the edge shared FePn_4 or FeCh_4 tetrahedra forming 1D chains instead of 2D square lattice, superconductivity was rarely discovered in this type of structure. Thus, investigation on the quasi-1D iron pnictides or chalcogenides with significant electron correlations may be beneficial for the understanding of the mechanism of the unconventional superconductivity. Until now, there are several iron chalcogenides with quasi-1D structure formed by edge shared FeSe_4 have been reported. However, transport or magnetic studies are still lacking for the majority of these compounds.

Superconductivity in quasi-1D system has been extensively explored in organic compounds, such as organic Bechgaard salts which exhibit charge density wave (CDW) or spin density wave (SDW) transition and superconductivity arise once the transition is suppressed by external pressure [36-38], As well as the fullerenes system M_3C_{60} (M = alkali metal), such as K_3C_{60} with $T_c \sim 18$ K [39] and Rb doped $\text{Cs}_2\text{RbC}_{60}$ with $T_c \sim 33$ K under ambient pressure [40]. In addition to an organic system, the inorganic quasi-1D system also have attracted considerable attention. For example, $\text{Li}_{0.9}\text{Mo}_6\text{O}_{17}$, which has been reported to exhibit a Tomonaga-Luttinger-liquid (TLL) state at high temperature and undergo a dimensional crossover from 1D to 3D metal at 24 K. The dimension crossover destabilizes the TLL fixed point and induce CDW or SDW transition, superconductivity is induced as the temperature decrease further with transition temperature at 1.9 K [41,42].

Back to the early 1970s, there were a large number of molybdenum chalcogenide superconductors $\text{M}_x\text{Mo}_6\text{X}_8$ ($\text{X} = \text{S}, \text{Se}, \text{or Te}$) discovered, as known as the Chevrel phases, where M can be monovalent, divalent or trivalent metallic elements with x varying from 0 to 4 [43-53]. The crystal structure of $\text{M}_x\text{Mo}_6\text{X}_8$ compounds contains Mo_6X_8 cluster, which six Mo atoms form an octahedron and eight X atoms are connected to the triangular facets from outside, and M atoms

can be inserted between the clusters. These quasi-1D Chevrel phase superconductors attracted great attention back that time due to their high transition temperature and high upper critical field, for example, PbMo_6S_8 with $T_c \sim 15$ K and $H_{c2} \sim 60$ T [45,54]. When Mo_6X_8 clusters are linearly connected to form a 1D chain structure, a new compound family $\text{M}_2\text{Mo}_6\text{X}_6$ was discovered. $\text{M}_2\text{Mo}_6\text{X}_6$ is another quasi-1D system that contains conducting Mo_6X_6 chains along the c axis that separated by M cations in ab -plane. The interaction between chains depends on the size of the M cations. Some compounds in this family were reported to be superconducting, for example, $\text{Na}_2\text{Mo}_6\text{Se}_6$, $\text{In}_2\text{Mo}_6\text{Se}_6$, and $\text{Tl}_2\text{Mo}_6\text{Se}_6$, superconductivity arises with transition temperature T_c of ~ 1.5 , 2.8 , and 4.2 K, respectively [55,56]. Interestingly, the crystal structure of $\text{M}_2\text{Mo}_6\text{X}_6$ is very close to another big compound family A_5B_3 (A = transition metals, B = main group elements) with pseudo-quasi-1D Mn_5Si_3 -type structure. Cation/anion sites and interstitial sites various doping possibilities in this type of structure have made it a rich playground searching for novel superconductors.

1.2 Magnetism

1.2.1 Basic properties of the magnetic materials

The discovery of antiferromagnetic order in the parent compound of iron-based superconductors have shown that magnetism plays a critical role in superconductivity with charge carriers doped to the parent compound. Many efforts have been made to understand the mechanism of interplay between magnetism and superconductivity. Many materials exhibit magnetic order, the different types of magnetic materials can be observed and classified based on the magnetic behavior of materials in response to magnetic fields at different temperatures. This response is described by its magnetic susceptibility χ , which is defined as $\chi = \frac{M}{H}$, the ratio of magnetization M (magnetic

moment per unit volume) to the applied magnetic field H . Two principal magnetic measurements of magnetic materials are the temperature dependence of magnetization $M(T)$, or $\chi(T)$, and the field dependence of magnetization $M(H)$.

1.2.2 Different types of magnetism

Depends on how magnetic materials react to the external applied field, magnetism can be classified into Diamagnetism, Paramagnetism, Ferromagnetism, Antiferromagnetism. Diamagnets exhibit small and negative magnetic susceptibility $\chi \approx -10^{-5}$. Their magnetic response opposes the applied magnetic field and does not retain the magnetic properties with the removal of the external magnetic field. Examples of diamagnets are copper (Cu), silver (Ag), gold (Au), bismuth (Bi), and beryllium (Be). Superconductors are the perfect diamagnets with magnetic susceptibility $\chi = -1$.

Paramagnets exhibit small and positive magnetic susceptibility and typically $\chi \approx 10^{-3} \sim 10^{-5}$. The magnetization of paramagnets is weak but aligned parallel with the direction of the magnetic field. Examples of paramagnets are aluminum (Al), platinum (Pt), and manganese (Mn). The temperature dependence of magnetic susceptibility $\chi(T)$ in paramagnet can be described by Curie's law, after Pierre Curie: $\chi(T) = \frac{C}{T}$, where C is a material-specific Curie constant and T is temperature.

A special case of paramagnet is called Pauli-paramagnet, which is usually metal because it describes the tendency of free electrons in an electron gas to align with an applied magnetic field. Paramagnetism is much stronger than pauli-paramagnetism because in the former, all of the magnetic atoms in the material contribute, while in the latter, only the tiny minority of electrons near the Fermi level contribute. χ_{pauli} is a very small positive value (10^{-5}), and independent of temperature.

The most widely recognized magnetic materials are the ferromagnets, which has positive susceptibility and much greater than 1, the typical value can reach $\chi \approx 50 \sim 10000$. Ferromagnetism occurs when the magnetic moments in a magnetic material line up spontaneously at a temperature below the so-called Curie temperature – named after Pierre Curie, who showed that ferromagnetism was lost at a critical temperature. Above the Curie temperature, the magnetic moments are aligned randomly, and the materials are typically paramagnetic. In a ferromagnet, magnetic moments of equal magnitude arrange themselves in parallel to each other. Examples of these materials are iron (Fe), cobalt (Co), nickel (Ni), and several rare earth metals and their alloys. The magnetic susceptibility χ of a ferromagnet in the paramagnetic region above the Curie temperature can be described by the Curie-Weiss law, $\chi(T) = \frac{C}{T - T_c}$, where T_c is the Curie temperature. The $M(H)$ of ferromagnetism exhibit the distinct hysteresis behavior which is a phenomenon that refers to the irreversibility of the magnetization and demagnetization process.

Antiferromagnets also exhibit positive magnetic susceptibility which increases with decreasing temperature and shows a maximum at the Neel temperature. Antiferromagnetic order exists below the Neel temperature but vanishes at and above the Neel temperature – named after Louis Neel, who had first identified this type of magnetic ordering. Above the Neel temperature, the material is typically paramagnetic. In an antiferromagnet, magnetic moments are equal in magnitude but aligned antiparallel to give zero net magnetization. Antiferromagnetic materials occur commonly among transition metal compounds, especially oxides. Examples include hematite (Fe_2O_3), metals such as chromium (Cr), alloys such as iron manganese (FeMn), and oxides such as nickel oxide (NiO). The magnetic susceptibility χ of an antiferromagnet in the paramagnetic region above the Curie point can also be described by the Curie-Weiss law, $\chi(T) = \frac{C}{T + T_N}$, where T_N is the Neel

temperature. The temperature dependence of the inverse of χ for paramagnetism, ferromagnetism, and antiferromagnetism is presented in Figure 1.3, reproduced from [57], they are parallel linear lines with x intercept at 0 , T_N , and T_c respectively.

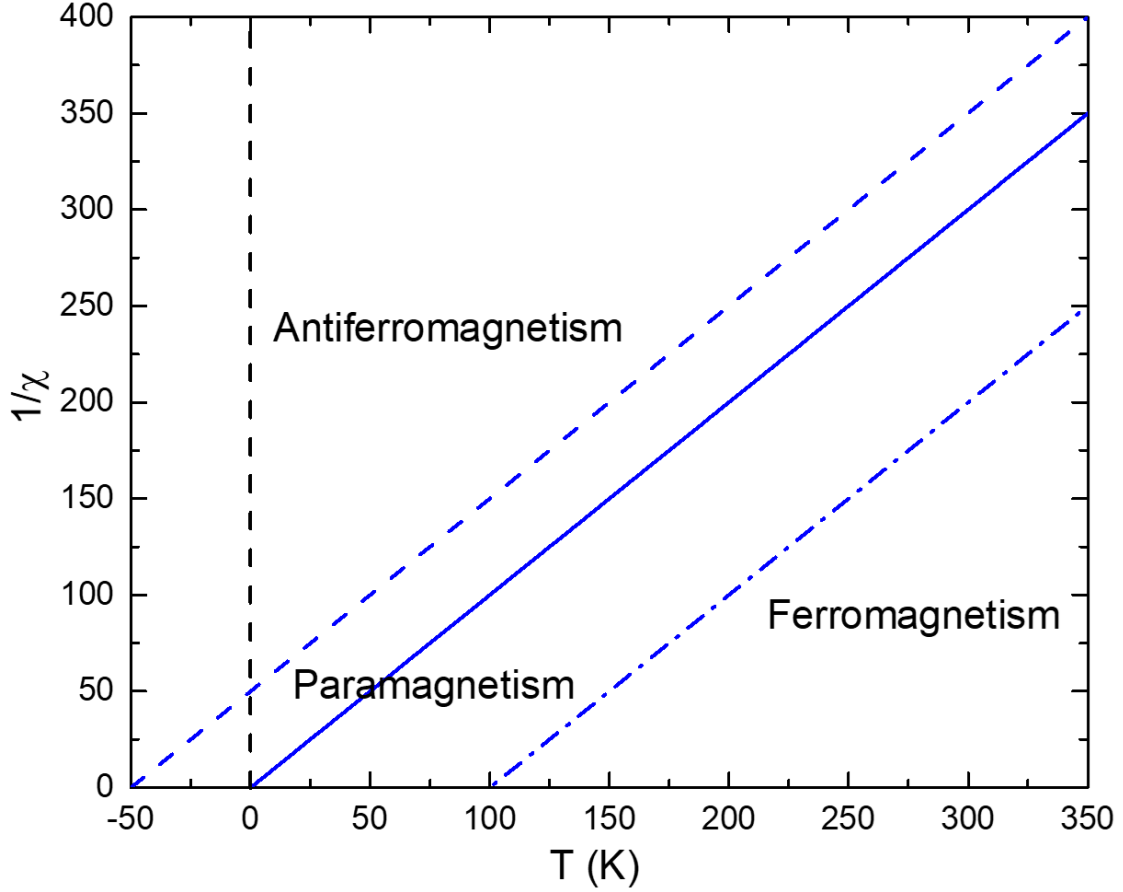


Figure 1.3: The inverse of χ as a function of T for Paramagnetic, Antiferromagnetic, and Ferromagnetic materials, their x intercept is 0 , T_N , and T_c respectively. (Figure reproduced from Ref. [57]).

1.3 Topological insulator

The aforementioned novel properties of superconductors make it one of the most interested and well-investigated systems in modern condensed matter physics. There is another new type of materials, topological insulator, that attracted tremendous research interest in recent decades due

to its unique physical properties. A topological insulator is a material that behaves as an insulator in its interior, but its surface remains as conducting, therefore the electron can only pass through the surface of the material. The gapless conductive surface states of topological insulators are protected by the time-reversed symmetry. The 2D and 3D topological insulator can be characterized by the Z_2 topological invariant, which define the ground state. In a 2D topological insulator, there is a single Z_2 invariant distinguishing the normal insulator (NI) from the quantum spin hall insulator (QSHI), while in a 3D topological insulator, there are four Z_2 invariants ($\nu_0; \nu_1 \nu_2 \nu_3$) that classified the insulator into weak and strong topological insulator (STI and WTI, respectively). An STI has a nontrivial ν_0 and an odd number of Dirac surface states, while a WTI with vanishing ν_0 has nontrivial ($\nu_1 \nu_2 \nu_3$) indices and even number of Dirac surface states. The electronic band structure of bulk topological insulator is similar to an ordinary insulator, with Fermi level falling between the conduction band and valence band. There are gapless conductive states on the surface of topological insulator that fall within the bulk energy gap and allow surface metallic conduction. The energy-momentum dispersion of surface states assumes a conical shape called a Dirac cone. The surface states in both strong and weak topological insulators are robust against defects and impurities which result in no energy loss transport. Such properties make topological insulators a great candidate for the future electronic devices or quantum computing applications.

Most of the topological insulators discovered so far are either 3D bulk materials such as $\text{Bi}_{1-x}\text{Sb}_x$ system [58-60] or layered materials such as Bi_2Se_3 family compounds [61,62]. The surface state in topological insulators is mainly investigated by angle-resolved photoemission spectroscopy (ARPES), however, since the topological surface state is mainly emerging on specific side

surfaces, which is usually extremely hard to be detected in 3D bulk materials. Recently, a new family of topological insulators with quasi-1D structure attracted tremendous research interest due to the unique surface properties related to its special quasi-1D structure. These quasi-1D compounds are typically consisted with stacking of building block of 1D molecule chains, the intrachain interaction is much weaker than the interchain interaction, making it easily to be cleaved with clean and flat surface without breaking the 1D molecular chains, providing some natural cleavage planes, enabling respective observations of stabilization and annihilation of distinct surface states, which is great candidates for the experimental realization of the WTI state. Due to the quasi-1D structure, the surface state also exhibits strong anisotropy, the surface electrons move much faster parallel to the molecule chain direction than perpendicular to it, which is significantly different from bulk or layered topological insulators. Moreover, the 1D molecule chains can stack in different patterns to form various topological phases exhibiting distinct topological properties, for example, α -Bi₄I₄ was predicted to exhibit hinges states while β -Bi₄I₄ is strong topological insulator [63], providing a rich playground for investigating topological properties in the distinct topological phases.

1.4 Motivation and scope of this work

The key interests of superconductors are to understand the mechanism of superconductivity and find materials with higher superconducting transition temperature. Although it is commonly believed that Cooper pairs coupled by electron-phonon coupling is responsible for conventional superconductivity, the pairing mechanism for unconventional superconductivity of high temperature superconductors is still controversial. The strongly correlated iron-based superconductors adopt quasi-2D layered structure and show a complex interplay among structural

transformation, magnetism and superconductivity. Thus investigation on another strongly correlated material systems with unique quasi-1D structure may be beneficial for us to understand the mechanism of unconventional superconductivity. Under this motivation, we investigated several materials system with distinct quasi-1D structure and hosting rather interesting magnetic, superconducting, and topological properties: iron chalcogenides, Mn_5Si_3 -type Zr_5Ge_3 , and topological materials Bi_4X_4 ($\text{X} = \text{I}, \text{Br}$). High quality of powders or single crystals have been synthesized through various methods, and characterized by XRD, EDAX, transport and magnetic studies. Chemical doping or intercalation has been done to search for superconductivity in these materials. The discovered new superconductors with unconventional superconductivity or topological superconductors could warrant further theoretical and experimental investigation of this system and have great potential applications in quantum computing or future electronic devices.

CHAPTER 2

MATERIALS SYNTHESIS AND CHARACTERIZATION TOOLS

2.1 Apparatus

2.1.1 Materials handling and reaction container

All manipulations were performed inside a purified argon (Ar) atmosphere glove box (MBraun) with total oxygen (O_2) and moisture (H_2O) levels < 0.1 ppm to prevent unwanted chemical reaction such as oxidation and hydrolysis that is degrading the sample. Different types of containers are used based on the synthetic conditions and starting materials for the materials synthesis. In most of the time, fused silica (quartz), alumina crucible, and inert metals (Nb or Ta) containers are used for the materials in this dissertation. Proper cleaning and drying of the containers prior to their usage is found to be crucial for the quality synthesis of the materials. Figure 2.1 shows a typical silica quartz tube, alumina crucible and Nb tube with one side closed that was used as a reaction container in the furnace.

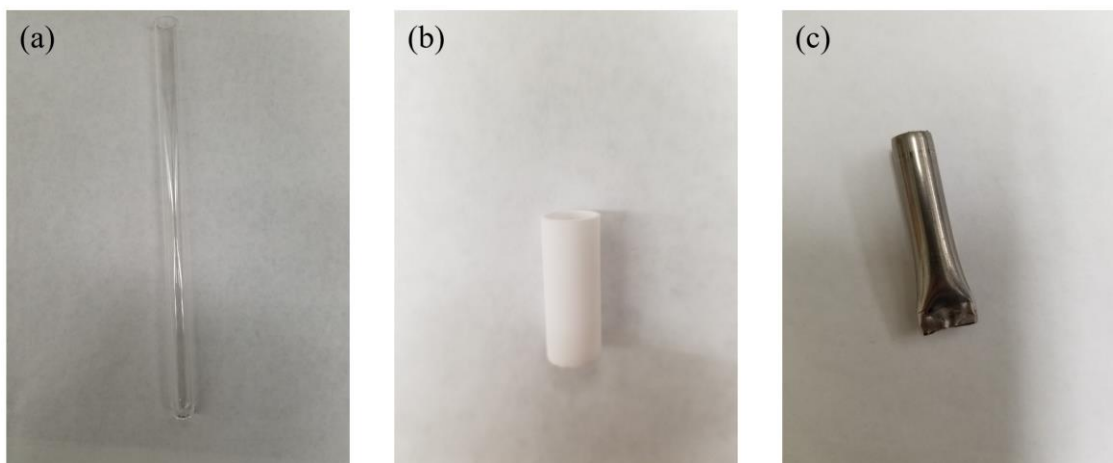


Figure 2.1: Photos of different containers used in this work: (a) silica quartz tube (b) alumina crucible (c) Nb tube closed on one side.

Typically, the silica quartz tubes were closed on one side using an H_2/O_2 torch flame system in the laboratory. They were cleaned first with acid to remove the surface oxide residue, then with a cleaner in an ultrasonic bath, washed with water and then acetone thoroughly, and then dried in an oven for at least overnight to avoid interior moisture residue. The tubes typically are left inside the glovebox for a week to be completely degassed before usage. For the reactions that involve Alkali metal (e.g. Potassium (K), Rubidium (Rb)) or Alkaline earth metal (e.g. Barium (Ba)) which are more corrosive to quartz tube at high temperature, inert containers such as alumina crucible or Niobium (Nb)/Tantalum (Ta) tube container are used to prevent the reaction of source materials with silica quartz tube at high temperature. The Nb/Ta tube containers were prepared in the laboratory from raw Nb/Ta tubes. The raw tubes were cut into ~ 4 cm long pieces, and then cleaned using a combined acid solution made from concentrated Sulfuric acid (H_2SO_4), concentrated Nitric acid (HNO_3), and diluted Hydrofluoric acid (HF) (55 : 25 : 20 by volume). The tubes then were thoroughly cleaned with water, dried in an oven, and then crimped on one end. The crimped end was then arc-welded under the Ar atmosphere using the arc-welding unit. All the reactants were loaded into the half-open either quartz tube, alumina crucible or Nb/Ta tube inside the glovebox, and then reaction vessels were taken out of the glovebox, and quickly sealed either under H_2/O_2 flame torque or arc-welder. For materials using Nb/Ta tubes as container, the sealed metal tubes with materials inside, were placed in an evacuated quartz tube and sealed to protect them from oxidation from the air before reaction taking place at high temperature.

Chemicals that is been used in this work are listed in Table 2.1. For the highly reactive alkali metals, such as K and Rb, the surface is carefully scraped to completely remove the oxidation before weighing. K/Rb is then cut into small pieces with the desired amount using a scraper and

loaded into an alumina crucible or Nb tube. The rest of the reacting chemicals were put on the top of K/Rb to prevent possible oxidation during transfer from glovebox to vacuum sealing line or arc-welded unit.

Table 2.1: List of all the chemicals used in this dissertation

Chemicals	Form	Purity (%)	Source (catalog number)	Melting point (°C)
Na	Pieces	99.8	Alfa Aesar (10342)	180.5
K	Pieces	99.5	Alfa Aesar (46687)	63.5
Rb	Pieces	99.75	Alfa Aesar (10315)	39.3
Ba	Pieces	99+	Alfa Aesar (10103)	727
Zr	Foils	99.9+	Alfa Aesar (43409)	1855
Mo	Powders	99.9	Alfa Aesar (00932)	2623
Fe	Granules	99.98	Alfa Aesar (39708)	1538
Fe	Powders	99+	Alfa Aesar (00737)	1538
Ru	Powders	99.95	Alfa Aesar (12061)	2334
Eu	Pieces	99.9	Alfa Aesar (12394)	822
Ce	Pieces	99	Alfa Aesar (43972)	799
Ir	Powders	99.95	Alfa Aesar (12070)	2446
Pd	Pieces	99.8	Alfa Aesar (12237)	1554.8
Pt	Powders	99.9	Alfa Aesar (36704)	1768.2
Si	Lumps	99.9999	Alfa Aesar (43006)	1414
Ge	Lumps	99.99	Alfa Aesar (10191)	938.25
Sn	Shots	99.99+	Alfa Aesar (36641)	231.93
P	Lumps	99.999	Alfa Aesar (10670)	44.15
As	Lumps	99.999	Alfa Aesar (00590)	817
Bi	Pieces	99.999	Alfa Aesar (14442)	271.4
Se	Shots	99.999	Alfa Aesar (10603)	220.8
Te	Lumps	99.999+	Alfa Aesar (10362)	449.51
I ₂	Pieces	99.8	Alfa Aesar (41955)	113.7
HgI ₂	Powders	99+	Alfa Aesar (16130)	259
HgBr ₂	Powders	99+	Acros Organics (190491000)	236
SnI ₂	Powders	99	Alfa Aesar (71112)	320
SnI ₄	Powders	95	Alfa Aesar (71114)	144

2.1.2 Furnace

After loading the starting chemicals into the silica quartz tube, the tube will be taken out of the glovebox and vacuum sealed under the vacuum sealing line, then placed in a furnace for the high

temperature reaction. Two types of furnaces with programmable controllers were used in this work. One type is the tube furnace, which consists of a cylindrical cavity surrounded by heating elements which consist of heating coils that are embedded in a thermally insulating matrix, temperature can be controlled by a K type thermocouple placed in the middle of the furnace. The tube furnace typically has two (or more) heating zones that exhibit temperature gradient along the heating zones, which can be used for the reactions that require temperature gradient along the tube, such as the chemical vapor transport reaction. The other type is the box furnace, which consists of a large volumes cubic cavity surrounded by heating elements, the temperature can be controlled by a K type thermocouple placed at the side of the furnace, and the temperature is almost uniform inside the box furnace. For those reactions that does not require temperature gradient, such as solid-state reaction and flux method, the box furnace is a great candidate because of its large volume, so multiple samples can be placed in the furnace simultaneously. Both furnaces are calibrated prior to use which is necessary in order to determine the accurate temperature inside the furnace. Figure 2.2 shows two types of furnace used in this work, the highest temperature that can be reached for both tube and box furnaces used in this work is 1100°C.



Figure 2.2: Photos of the furnace used in this work (a) tube furnace (b) box furnace

2.2 Synthesis

For the sample synthesis and crystal growth, various synthetic methods such as solid-state reaction, flux method, chemical transport reaction and arc melting technique were used in this work.

2.2.1 Solid-state reaction

The solid-state reaction is the most widely used method for material synthesis and crystal growth. The source elements were mixed together with a required stoichiometric ratio, and vacuum sealed in a silica quartz tube. For some reactions, the reaction mixture may need be finely ground to powder in an agate mortar, pressed into a pellet inside the glove box with a hydraulic press up to 5 Tons using tungsten carbide (WC) press matrices to increase contact area, and sintered for prolonged periods for better homogeneity of the reaction products.

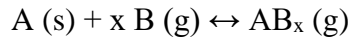
2.2.2 Flux method

The flux method was used to grow single crystals or carry out a reaction at a temperature much lower than what is normally used in the solid-state reaction. Salt fluxes and low melting metal fluxes are the most widely used solvents in the flux method. Many salts have high melting temperatures, but the eutectic combinations of binary salts often have much lower melting points and well below the solid-state reaction, making the possible synthesis of new compounds at intermediate temperatures [64]. Some metals have a low melting point, good solubility of desired materials, and does not form compounds with the reacting materials at the desired temperature range can also be used as flux, for example, Tellurium (Te), Sn, Pb, and Ga metals. During the flux method, a very slow cooling rate (typically less than 2 °C/hour) of the melt is necessary for the quality and large size of crystal growth. In order to separate the crystals from the flux being

used, typically high speed centrifuge at elevated temperature ($> 100\text{ }^{\circ}\text{C}$ higher than the flux melting temperature) is performed after the reaction is completed.

2.2.3 Chemical vapor transport reaction

For materials that volatile elements or gaseous species could be formed, chemical vapor transport reactions will be utilized. In a chemical transport reaction, a nonvolatile solid compound A reversibly reacts with a gaseous transport agent B (e.g. I_2 , HgI_2 , HgBr_2) to form a gaseous species AB_x at one temperature, transport to another temperature region, and to form crystals from the gaseous phase at another temperature [65].



The thermal gradient provides the driving forces for the mass transport and thermodynamic stability of each phase formed at different temperature regions. Typically, The closed silica quartz tube containing the source materials A and B is placed in a tube furnace where a temperature gradient T_1 and T_2 exists inside the tube, as shown in Figure 2.3 [66].

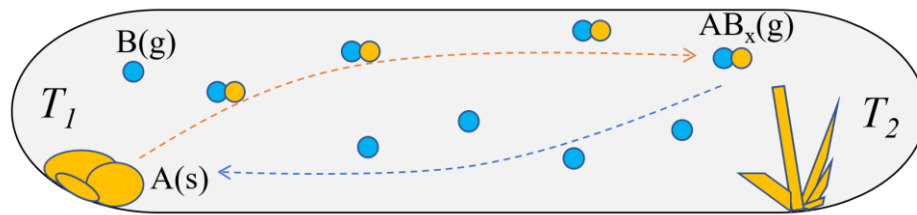


Figure 2.3: Scheme of chemical vapor transport reaction for crystals growth in a temperature gradient (Figure reproduced from Ref. [66]).

Whether the transport is from lower temperature T_1 to higher temperature T_2 or from T_2 to T_1 , depending on the thermo-chemical equilibrium of the reaction. If the formation of AB_x is endothermic ($\Delta H > 0$), the transport takes place from higher temperature to lower temperature. If

the formation of AB_x is exothermic ($\Delta H > 0$), AB_x will form at lower temperature and decompose at higher temperature.

2.2.4 Arc melting

Arc melting technique is used to melt metal to form alloy at high temperature which can be higher than 2000 °C. The arc-furnace is a home-built system using tungsten (W) tip as the electrode, a whole water-cooled copper block as chamber and hearth (which have better cooling efficiency comparing to commercial products), and current source up to 160 A. The starting elements were placed on a water-cooled copper hearth in the arc melting unit, as shown in Figure 2.4.

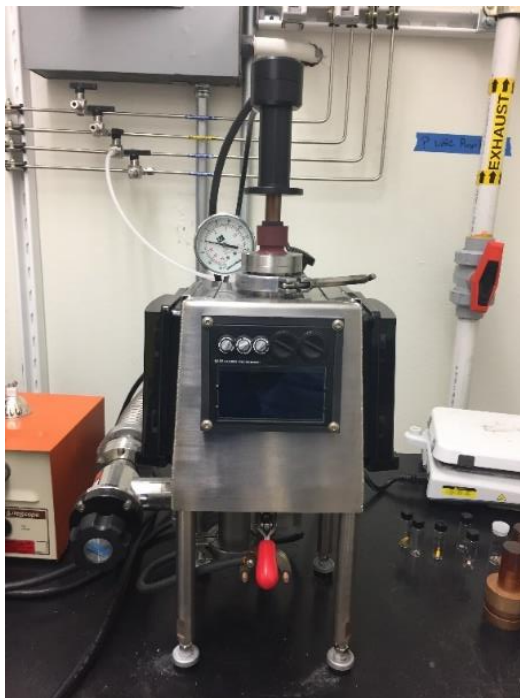


Figure 2.4: Photo of the arc melting unit used in this work

The chamber is evacuated and then refilled with Ar gas, and the process is repeated several times, hence, melting is performed in Ar atmosphere. A Zirconium (Zr) piece is used as O_2 getter by melting it to further remove the residue O_2 in the chamber. Electric arc is induced by applying

current and struck between a tungsten electrode and metals. During the arc melting process, the melted sample will be flipped and remelted several times to ensure the homogeneity of the sample.

2.3 Analytical methods

2.3.1 X-ray diffraction

2.3.1.1 Powder X-ray diffraction

X-ray powder diffraction (XRD) has been used to check for the crystal structure of the samples. It was performed on a Rigaku SmartLab diffractometer at room temperature, as shown in Figure 2.5.



Figure 2.5: Photo of the Rigaku SmartLab XRD diffractometer used in this work

Relative intensities and Bragg positions (2θ) of each reflection were measured by a position sensitive detector (PSD). The measurement has been done in the range $2\theta = 10^\circ - 90^\circ$ for 10 – 45 minutes. The samples were ground to fine powder prior to the measurements to ensure homogeneity and even sizes of the crystallites of the samples and were placed on a glass slide

during the measurement. Precise measurements used for Rietveld refinement were performed on a silicon zero-background holder to eliminate background noise. For the samples that are air or moisture sensitive, they are protected by applying an overlayer film of vacuum grease. This vacuum grease will have a broad hump in the XRD pattern in the range of 15° to 25° and two extra grease peaks around 21° and 23°. The theoretical patterns that used to evaluate the powder patterns were obtained from Inorganic Crystal Structure Databank (ICSD). Peak search, indexing, cell refinement, calculations of theoretical patterns and identification of the sample with the Powder Diffraction File (PDF) [67] were carried out with the programs of MDI Jade. Rietveld refinements of the powder pattern were done through the JANA 2006 package.

2.3.1.1 Single crystal X-ray diffraction

The phase identification and crystal structure of single crystals were determined by single crystal X-ray diffraction. Small single crystals were picked up under a microscope. Air sensitive crystals were picked inside an Ar filled glovebox while stable crystals were picked outside. Single crystals were then mounted to glass fibers with two-part epoxy. The fibers were mounted on a Bruker APEX DUO diffractometer equipped with an Apex II area detector and an Oxford Cryosystems 700 Series temperature controller. The collected data set was integrated with Bruker SAINT and scaled with Bruker SADABS (multiscan absorption correction) [68]. A starting model was obtained using the intrinsic phasing method in SHELXT [69], and atomic sites were refined anisotropically using SHELXL2014 [70].

2.3.2 Neutron powder diffraction

Neutron powder diffraction was performed on the HB-2A Neutron powder diffractometer (NPDF) at Oak Ridge National Laboratory (ORNL) equipped with 44 ³He detectors with 2×10^{-3} Δd/d

resolution. Measurable temperature is 0.03 ~ 1800 K, magnetic field up to 8 T and pressure up to 2 GPa. The Neutron powder diffraction is similar to the XRD powder diffraction in terms of principles. However, the scattering of neutrons primarily occurs at atom nuclei, different from the x-ray which primarily interacts with the electron cloud surrounding each atom. Thus, Neutron powder diffraction can provide more complementary information that cannot be obtained by XRD powder diffraction. Since neutron carries magnetic moment, which makes it a great candidate to determine the magnetic structure of a given material.

2.3.3 Scanning Electron Microscope (SEM) and Energy Dispersive X-ray Spectroscopy (EDAX)

Morphology of the crystals was checked by SEM, and elemental composition was examined by EDAX using Zeiss-LEO model 1530 variable pressure field effect scanning electron microscope. The operation voltage was set to 19 kV for all measurements (30 seconds collection time). The crystals were placed onto a carbon tape which was glued on top of an aluminum sample holder. Crystals were tested qualitatively to verify the chemical composition of elements, and internal standards using known crystals with fixed stoichiometry are used for the quantitative composition analysis.

2.3.4 Transport measurements

Resistivity and heat capacity measurements were performed on PPMS (Quantum Design). The powder samples are hot-pressed into a pellet using hydraulic press before the measurements. The temperature and field dependence of the electrical resistivity $\rho(T,H)$ was measured by the standard four-probe technique using highly conductive silver paste and gold wires from 1.8 K to 400 K. The specific heat was measured down to 1.8 K and up to 9 T on the PPMS at constant pressure.

Typical weight 1 ~ 200 mg of sample is mounted to a platform with grease, which provides thermal contact to the platform. A heater and thermometer are attached to the bottom of platform connected with thermal bath by wires. The heat capacity of addenda (platform, heater, thermometer and the grease) is measured prior to the sample heat capacity. After performing the total heat capacity measurement, the sample heat capacity is obtained through subtraction of the heat capacity of addenda from the total heat capacity. The purity and overall quality of the sample can be evaluated by the Residual-resistivity ratio (RRR) from the resistivity measurement, which is defined as the ratio of the resistivity of the sample at room temperature and at the lowest measured temperature. The RRR value depends on the impurities or defects in the sample, a higher RRR value indicates a better quality of the sample [71]. Figure 2.6 shows the PPMS used in this work.

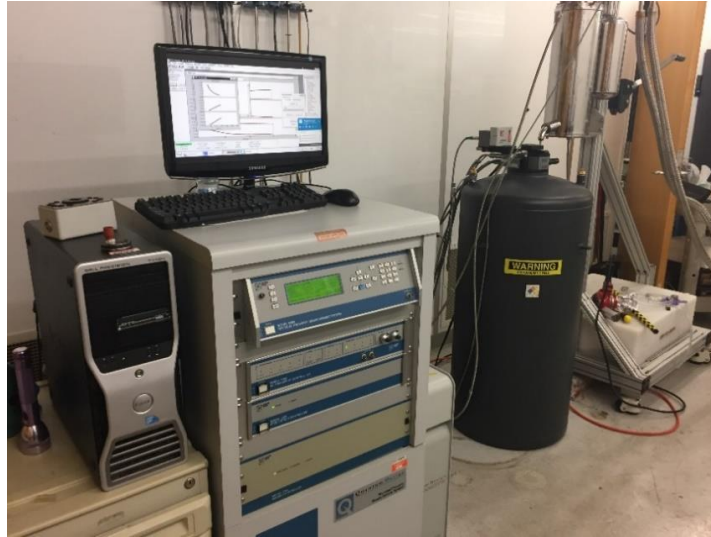


Figure 2.6: Photo of the PPMS (Quantum Design) used in this work.

2.3.5 Magnetic measurements

Magnetic measurements were performed on MPMS (Quantum Design) superconducting quantum interference device (SQUID) magnetometer with liquid Helium cooling. Figure 2.7 shows the MPMS used in this work. The measurable temperature range is from 1.8 K to 400 K and the

magnetic field can reach up to 70000 Oe (7 Tesla). Typical weight of 20 ~ 100 mg sample was placed into a gelatin capsule. The closed capsule was then fixed in a plastic straw which was then attached to the sample rod of the SQUID. The sample position in the SQUID was adjusted with the automatic DC center scan technique. Superconducting materials were tested in the range of 1.8 – 30 K using the zero-field cooled (ZFC) and field cooled (FC) modes with a stable applied field of 10 Oe and step size of 1 K in sweep mode. Other materials were tested in the range of 5 – 350 K using the ZFC / FC modes with stable applied field range from 100 ~ 50000 Oe and step size of 5 K in sweep mode.



Figure 2.7: Photo of the MPMS (Quantum Design) used in this work.

ZFC and FC measurements are a method where the sample is cooled to the lowest measured temperature without an applied field. A field is applied, and measure a temperature dependence of magnetization up to the highest measured temperature (ZFC), and then repeat the measurement

during cooling down to the lowest temperature with field applied (FC) [72]. With this method, we can detect the magnetic order transitions in a material. For a superconductor, the superconducting transition temperature T_c is the temperature where ZFC and FC curve start to split upon cooling. The superconducting shielding volume fraction can be obtained from the ZFC curve, which is given as $S = \frac{4\pi M}{VH}$, where M is the magnetization at the lowest measured temperature, V is the sample's volume and H is the applied magnetic field. The shielding volume fraction is an important parameter that indicates what is the percentage of the sample is superconducting, in other words, whether the superconductivity is coming from bulk. A perfect superconductor should have a 100% shielding volume fraction after the correction of the demagnetization factor.

CHAPTER 3

MAGNETISM IN SEVERAL COMPLEX QUASI-1D IRON CHALCOGENIDES SYSTEMS

3.1 Introduction

Among all the iron-based superconductors, the FeSe and its related systems are of particular interest due to its simplest crystal structure and peculiar electronic and physical properties. The compound consists only of the essential FeSe superconducting layers without any other charge reservoir layer in between, which is ideal for both theoretical and experimental study for the superconducting mechanism. The bulk FeSe undergoes a structural transition from tetragonal to orthorhombic around 90 K but without a magnetic transition [73,74], and is superconducting with $T_c \sim 8$ K [17]. Under high pressure, both static magnetic order and short range spin fluctuation are observed, and the T_c is dramatically enhanced to 37 K [18]. Interestingly, the close-related compound, FeTe with the same structure, possesses a unique antiferromagnetic ground state but is non-superconducting. Gradually replacing the Se by Te for FeSe_{1-x}Te_x system has resulted in a nice superconducting phase diagram with maximum $T_c \sim 15$ K [75-77]. Later on, alkali metal (A = K, Rb, Cs, and Tl) intercalated A_{1-x}Fe_{2-y}Se₂ superconductors, a chalcogenide analog to the BaFe₂As₂ 122-type iron pnictide superconductors, were reported with $T_c \sim 30$ K [19-23]. Chemical intercalation in the liquid ammonia media by the ammonothermal method at room temperature also succeeds to intercalate the series of metals, Li, Na, Ba, Sr, Ca, Yb, and Eu in between FeSe layers with enhanced $T_c = 30 \sim 46$ K [78-81]. What most striking is that superconductivity above 65 K are found in the ultra-thin monolayer FeSe on the SrTiO₃ (STO) substrate grown by the MBE technique [24-29]. The reported T_c , although mainly by spectroscopy tools, far exceeds the 8 K T_c

found in the bulk crystal [17], 15 K T_c in the Te-doped Fe (Se,Te) crystal [75], and even much higher than the T_c under high pressure [18]. Further ARPES studies suggest the Fermi surface for monolayer FeSe films consists of only an electron pocket near the zone corner M without any Fermi surface crossing near the zone center Γ (i.e. no electron-hole nesting) [24,26,27]. This is completely different from the Fermi surface of the bulk FeSe. Therefore, proximity effect through FeSe and STO interfaces is attributed to much enhanced T_c . These results further trigger worldwide research in the iron chalcogenides and interfacial superconductivity in heterostructures.

All the iron chalcogenides superconductors discovered so far have charge-carrier layers consisting of the tetragonally-coordinated FeCh₄ layers and Fe-Fe square lattice within the layers, and very similar to the iron pnictide compounds. However, the T_c so far is saturated below 60 K except for the case in the monolayer FeSe/STO system. In order to further enhance the T_c , different types of materials, with similar FeAs₄ or FeCh₄ building blocks but different types of layered structures, need to be explored. It has been shown that the T_c of cuprates increases with n, the number of CuO₂-layers per unit cell, for n up to 3. If one can find similar compounds in the Fe-based systems, it is likely he will be able to further enhance the T_c if proper doping and modification of the structures can be achieved. This approach appears to be infeasible for pnictide-based compounds, as the double layered Fe-As structure requires additional bond formation of adjacent Fe₂As₂ layers. As a consequence, there will be unpaired electrons from the FeAs₄ tetrahedra will form additional bonds with others, thus breaking the decidedly balanced tetrahedrally coordinated Fe₂As₂ layers, as exemplified in the CaFe₄As₃, and REFe₄Sb₅ (RE = Rare earth elements) structures. On the other hand, Se is electron-poorer than the pnictide. Such electron deficiency has caused the existence of Fe defects in the associated K_{1-x}Fe_{2-y}Se₂ compounds to satisfy the electron and valence balance.

Alternatively, the FeCh_4 building blocks could link with each other, form edge-shared quasi-1D double chains along certain crystallographic axis showing interesting properties.

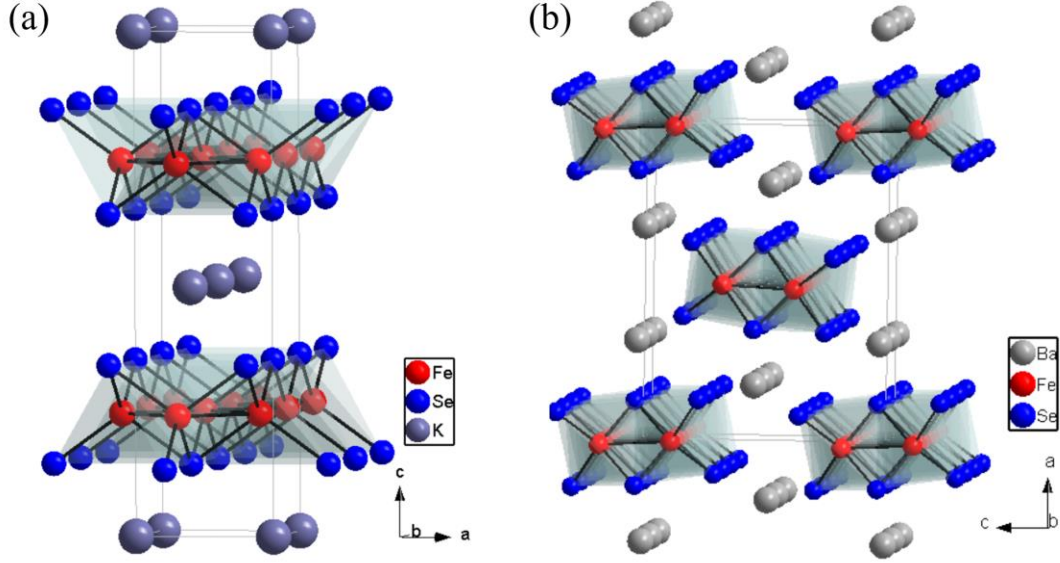


Figure 3.1: Crystal Structure of (a) layered $\text{K}_x\text{Fe}_2\text{Se}_2$ compound (b) quasi-1D BaFe_2Se_3 compound. Both compounds consist of edge sharing FeSe_4 tetrahedra, forming 2D square lattice along ab plane in $\text{K}_x\text{Fe}_2\text{Se}_2$ while 1D double chain along b -axis in BaFe_2Se_3 .

BaFe_2Se_3 is an example as a consequence of such structural packing. In contrast to the case for alkali metal intercalated chalcogenides (like $\text{K}_x\text{Fe}_2\text{Se}_2$), the Fe-Se layers are not two dimensional but consist of quasi-1D double chains of $[\text{Fe}_2\text{Se}_3]$ formed by edge shared FeSe_4 tetrahedra along b -axis and separating by Ba atoms. The distinct crystal structure of $\text{K}_x\text{Fe}_2\text{Se}_2$ and BaFe_2Se_3 is shown in Figure 3.1. BaFe_2Se_3 crystallizes in the orthorhombic space group $Pnma$ (62), the 1D $[\text{Fe}_2\text{Se}_3]$ chains in BaFe_2Se_3 can be achieved by removing every third Fe atom from the 2D $[\text{FeSe}]$ layers in $\text{A}_x\text{Fe}_2\text{Se}_2$. BaFe_2Se_3 was reported to exhibit unique spin ladder magnetic structure and long-range-ordered antiferromagnetic order below $T_N \sim 256$ K or $T_N \sim 240$ K, and short-range magnetic correlations at room temperature [82,83]. Fe lattice distortion below Neel temperature is also reported [84], indicating the lattice and magnetism are strongly coupled. In addition,

BaFe₂Se₃ was reported to be superconducting under high pressure above 10 GPa with transition temperature $T_c \sim 11$ K [85], similar to its analog BaFe₂S₃, which is superconducting with $T_c \sim 14$ K under the pressure of 11 GPa [86]. These reports further motivate us to search for new superconductors that built of FeSe₄ tetrahedra and adopt the quasi-1D structure in the iron chalcogenides system.

BaFe₂Se₄ and K₃Fe₂Se₄ are another two iron chalcogenides with FeSe₄ tetrahedra building blocks adopting different quasi-1D structures than the BaFe₂Se₃. BaFe₂Se₄ consists of single chains of edge sharing FeSe₄ tetrahedra along the c-axis, which is even simpler than the double chain structure of BaFe₂Se₃. K₃Fe₂Se₄ consists of zig-zag infinite chains of edge sharing FeSe₄ tetrahedra along the b-axis separated by K atoms. Up to date, no XRD pure phases have been achieved, nor systematical transport and magnetic characterizations have been carried out on these compounds. Small amounts of magnetic FeSe₂ and Fe_{1-x}Se impurities phases were identified and difficult to eliminate in BaFe₂Se₄ from the previous report [87]. These impurities will affect significantly to probe the intrinsic properties of BaFe₂Se₄. for K₃Fe₂Se₄, only one report describes its crystal structures based on sub-micro size x-ray crystal diffraction [88]. We therefore, synthesized the pure phase BaFe₂Se₄ and K₃Fe₂Se₄ polycrystalline power sample and performed the transport and magnetic measurements. chemical doping studies were also carried out to induce possible superconductivity on these compounds.

3.2 Experimental procedures

The BaFe₂Se₄ and K₃Fe₂Se₄ polycrystalline sample was prepared by the conventional solid-state reaction method. For the synthesis of BaFe₂Se₄, elemental Ba pieces (Alfa Aesar, 99+%), Fe granule (Alfa Aesar, 99.98%) and Se shot(Alfa Aesar, 99.999%) were used as starting materials

and mixed with stoichiometry ratio with ~ 5 % excess of Se to compensate the Se lose during the reaction. The reactants then were sealed under vacuum in the quartz tube. The reaction was carried out at 700 °C for 2 days, then the tube was cooled to room temperature in 10 hours. Several times regrounding and annealing at 600 °C for two weeks are necessary to improve the homogeneities of the samples. Polycrystalline $K_3Fe_2Se_4$ samples were synthesized in three steps, precursor FeSe was obtained first by mixing elemental Fe granule and Se shot with 1 : 1 ratio and then sealed into the evacuated quartz tube. The reaction was carried out at 800 °C for 1 day, then FeSe was finely ground to powder. Precursor KSe was synthesized by mixing elemental K pieces and Se shot with a stoichiometric ratio of 1:1 in an alumina crucible and then sealed into an evacuated quartz tube. The quartz tube was very slowly heated (20 hours) to 200 °C and kept at 200 °C for 20 hours followed by furnace cooling down to room temperature. It should be noted that the drastic reaction of K and Se will release a large amount of heat and may potentially cause tube breaking, so the maximum amount of KSe is limited to ~ 300 mg in one alumina crucible. The obtained KSe was ground into fine powder and mixed with Fe powder (Alfa Aesar, 99+%) and previously obtained FeSe powder with a ratio of 3 : 1 : 1. The mixture was finely ground and pressed into a pellet. The pellet was placed into an alumina crucible and vacuum sealed into a quartz tube. The sample was heated at 700 °C for 2 days before cooled down to room temperature. After that, polycrystalline samples of $BaFe_2Se_4$ and $K_3Fe_2Se_4$ were obtained for structural and physical characterizations. All doped samples are synthesized at 700 °C by mixing the starting materials at a stoichiometric ratio with 5% excess of Se. The obtained $BaFe_2Se_4$ is stable in air while $K_3Fe_3Se_4$ is sensitive to air. All experimental procedures mentioned above except sealing and high temperature heat treatment were carried out in an Ar-filled glove box to avoid the possible oxidation of the samples. The

exposure to air should be kept as minimum when performing measurements on $\text{K}_3\text{Fe}_2\text{Se}_4$ sample. Au leads are placed on sample inside the glovebox and then quickly transferred to PPMS for the transport measurement. The gelatin capsule is also prepared inside the glovebox and transferred to MPMS in an airtight vial for the magnetic measurement. The crystal structure was characterized at room temperature by powder x-ray diffraction on the Rigaku Smartlab, and the Rietveld refinement of the XRD patterns were done through the JANA 2006 package. Resistivity as a function of temperature was measured with a PPMS-9T (Quantum Design) down to 1.8 K using a standard four-probe technique. The dc magnetic susceptibility $\chi(T)$ were carried out using the MPMS (Quantum Design) down to 5 K and up to 5 T.

3.3 Results and discussion

The synthesized BaFe_2Se_4 compound is black, while $\text{K}_3\text{Fe}_2\text{Se}_4$ compound is dark brown. The XRD pattern of the synthesized BaFe_2Se_4 and $\text{K}_3\text{Fe}_2\text{Se}_4$ samples are presented in Figure 3.2. Both XRD patterns do not indicate any impurity phase within the resolution of the measurement. All peaks can be indexed with the results from the theoretical pattern. The hump in the XRD pattern of $\text{K}_3\text{Fe}_2\text{Se}_4$ between 15° and 25° is due to the vacuum grease that used to protect the sample from air during measurement. The high intensity of peaks of XRD pattern indicates good quality of BaFe_2Se_4 sample, While the peaks intensity on the XRD patterns of $\text{K}_3\text{Fe}_2\text{Se}_4$ sample is relatively weaker. The crystallinity of $\text{K}_3\text{Fe}_2\text{Se}_4$ sample is deteriorated by the amorphous substance that was contained in the powder sample, although $\text{K}_3\text{Fe}_2\text{Se}_4$ sample has been reground and annealed several times with long total annealing time ($>$ two weeks) and the XRD peaks intensity got slightly improved after every regrounding and annealing. Even longer annealing times may be needed for this material to completely eliminate the amorphous substance in the sample.

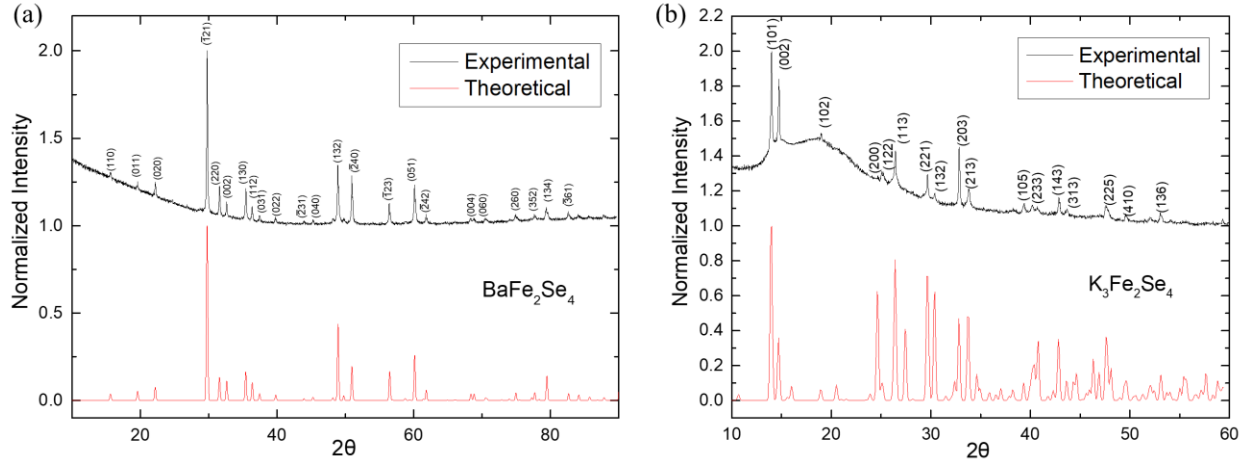


Figure 3.2: XRD pattern for (a) BaFe_2Se_4 (b) $\text{K}_3\text{Fe}_2\text{Se}_4$ samples, no impurity was observed within the resolution of the measurement.

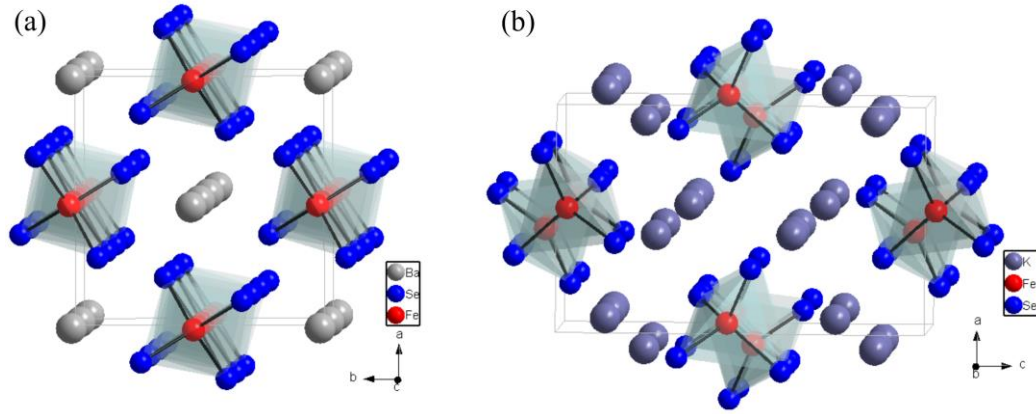


Figure 3.3: Crystal Structure of (a) BaFe_2Se_4 , contains single chains of edge sharing FeSe_4 tetrahedra along the c -axis separated by Ba atoms (b) $\text{K}_3\text{Fe}_2\text{Se}_4$, it contains zig-zag infinite chains of edge sharing FeSe_4 tetrahedra along b -axis separated by K atoms.

Crystal structure of BaFe_2Se_4 and $\text{K}_3\text{Fe}_2\text{Se}_4$ are shown in Figure 3.3. BaFe_2Se_4 is isotypic to its sulfide counterpart BaFe_2S_4 crystallizing in the tetragonal space group $I4/m$ (87) with $a = b = 8.009(1) \text{ \AA}$, and $c = 5.483(2) \text{ \AA}$ [87]. The crystal structure of $\text{K}_3\text{Fe}_2\text{Se}_4$ is isotypic with $\text{Na}_3\text{Fe}_2\text{Se}_4$ and $\text{Rb}_3\text{Fe}_2\text{Se}_4$ crystallizing in the orthorhombic space group $Pnma$ (62) with $a = 7.433(2) \text{ \AA}$, $b = 11.341(3) \text{ \AA}$ and $c = 12.016(3) \text{ \AA}$ [88]. Both compounds consist of 1D infinite chains of edge sharing FeSe_4 tetrahedra. The chains are propagated along the c -axis in BaFe_2Se_4 , while the edge

sharing FeSe_4 tetrahedra are slightly distorted in $\text{K}_3\text{Fe}_2\text{Se}_4$, forming zig-zag chains propagating along the b -axis, as shown in Figure 3.4. The Fe-Fe distance within the chain are $2.865(7) \text{ \AA}$ and $3.015(7) \text{ \AA}$ in $\text{K}_3\text{Fe}_2\text{Se}_4$, in contrast to $2.742(9) \text{ \AA}$ in BaFe_2Se_4 . Individual Fe-Se bond distances are: $\text{Fe-Se}_3 = 2.402(4) \text{ \AA}$, $\text{Fe-Se}_1 = 2.407(4) \text{ \AA}$, $\text{Fe-Se}_2 = 2.441(3) \text{ \AA}$, $\text{Fe-Se}_1 = 2.465(3) \text{ \AA}$, in contrast to $\text{Fe-Se} = 2.349(5) \text{ \AA}$ in BaFe_2Se_4 .

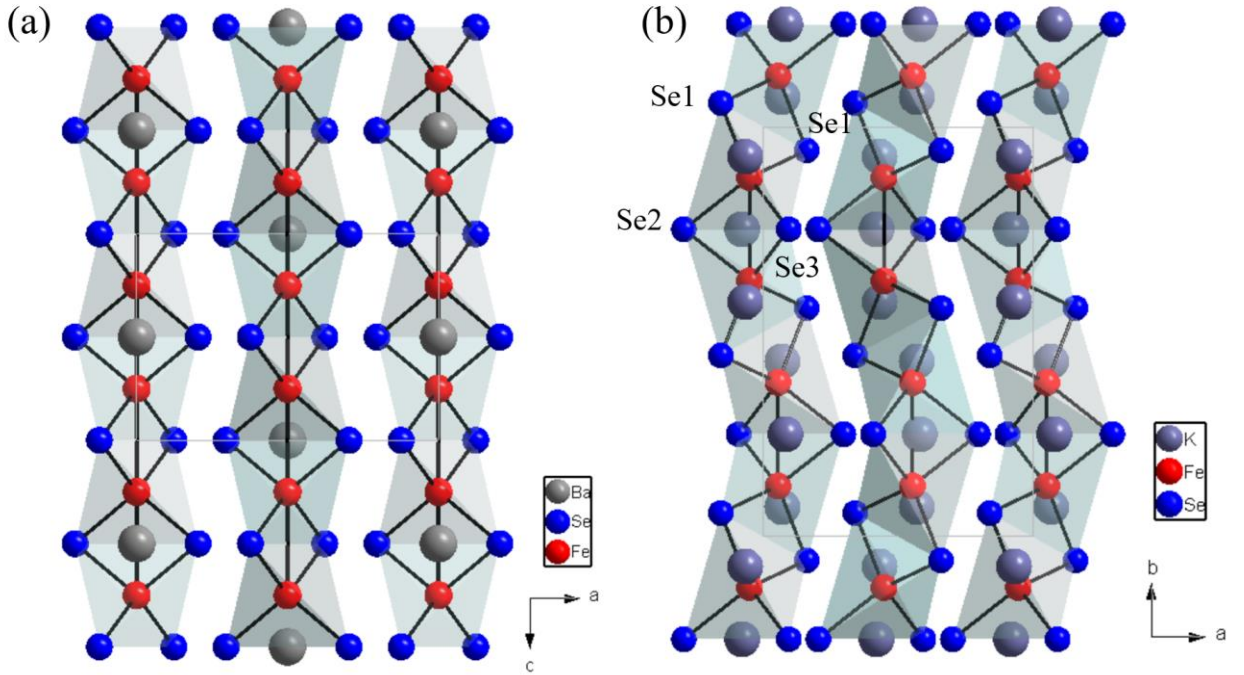


Figure 3.4: the side view 1D chains of FeSe_4 tetrahedra in (a) BaFe_2Se_4 (b) $\text{K}_3\text{Fe}_2\text{Se}_4$ with respect to b - and c -axis, respectively. The chains are propagated along the c -axis in BaFe_2Se_4 , while the edge sharing FeSe_4 tetrahedra are slightly distorted in $\text{K}_3\text{Fe}_2\text{Se}_4$, forming zig-zag chains propagating along the b -axis.

The temperature dependences of electrical resistivity for BaFe_2Se_4 and $\text{K}_3\text{Fe}_2\text{Se}_4$ samples are shown in Figure 3.5. The resistivity of both samples increases with decreasing temperature, which is the typical insulating behavior. The resistivity can be described by an Arrhenius temperature dependence, $\rho = \rho_0 \exp(E_a/K_B T)$, where K_B is the Boltzmann constant [89,90]. The activation energy E_a was estimated to be $\sim 27.5 \text{ meV}$ and $\sim 239.6 \text{ meV}$ for BaFe_2Se_4 and $\text{K}_3\text{Fe}_2\text{Se}_4$,

respectively. The activation energy of BaFe_2Se_4 is much smaller than BaFe_2Se_3 , which is also insulating with activation energy ~ 130 meV [84]. The activation energy of $\text{K}_3\text{Fe}_2\text{Se}_4$ is larger than BaFe_2Se_4 , showing $\text{K}_3\text{Fe}_2\text{Se}_4$ exhibit more insulating nature than BaFe_2Se_4 . The resistivity data obtained for BaFe_2Se_4 is in agreement with the measurement reported for its isostructural counterpart BaFe_2S_4 which also exhibits insulating behavior [91]. Both samples show a variable-range-hopping-type (VRH) behavior at low-temperature regime, The data are fitted to $\rho = \exp(A/T^{1/(1+d)})$, where A is a constant and d denotes dimension of the VRH model. The VRH in the 1D model fits better on both samples rather than the higher dimensions, as shown in inset of Figure 3.5, which are more natural and reasonable for these materials with quasi-1D structure.

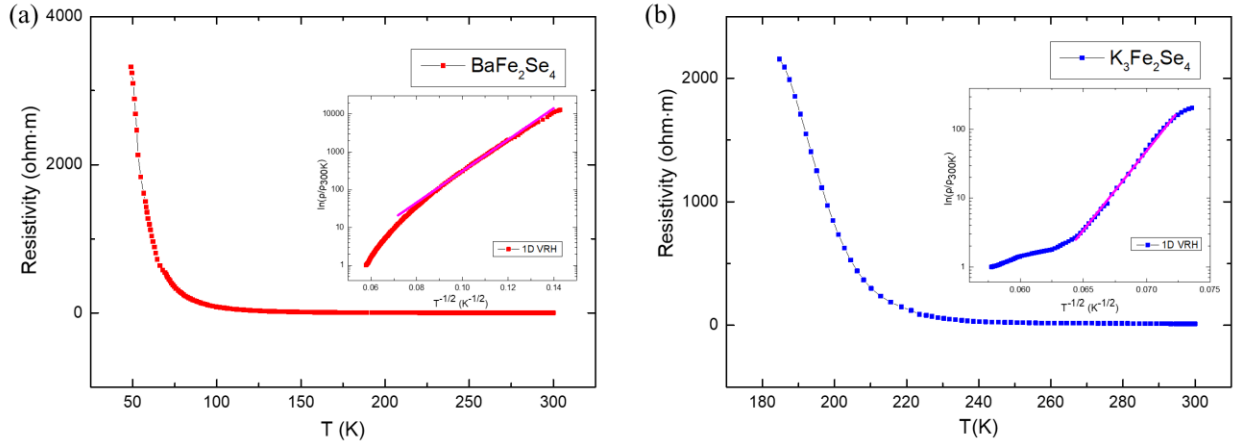


Figure 3.5: Temperature dependence of resistivity on (a) BaFe_2Se_4 and (b) $\text{K}_3\text{Fe}_2\text{Se}_4$ samples. Both samples show insulating behavior. The activation energy extrapolated using Arrhenius temperature dependence equation are ~ 27.5 meV and ~ 239.6 meV for BaFe_2Se_4 and $\text{K}_3\text{Fe}_2\text{Se}_4$, respectively.

Although BaFe_2Se_4 adopts a similar tetragonal structure as other iron pnictides and chalcogenides, which typically exhibit antiferromagnetic order and superconductivity. The magnetic order of BaFe_2Se_4 was observed to be ferromagnetic which is in sharp contrast with those materials. The temperature dependence of the magnetic moment of BaFe_2Se_4 from 5 K to 350 K with ZFC and

FC measurements under stable magnetic fields of 100 Oe and 1000 Oe are displayed in Figure 3.6. Typical irreversible behavior for a ferromagnetic order was observed in $M(T)$ measured with ZFC and FC histories. The transition temperature is estimated to be ~ 320 K from the derivative dM/dT . This result is significantly distinct to the aforementioned spin-ladder compound BaFe_2Se_3 , although they adopt similar crystal structures: single chain of FeSe_4 tetrahedra in BaFe_2Se_4 while double chain in BaFe_2Se_3 . BaFe_2Se_3 exhibits block-type antiferromagnetic order ~ 255 K, four Fe atoms along the chain form a Fe_4 ferromagnetic block, and each Fe_4 stacks antiferromagnetically. The Ferromagnetic nature of BaFe_2Se_3 indicates that Fe atoms are ferromagnetically correlated along and perpendicular to the chain direction.

The field dependence of magnetic moment for BaFe_2Se_4 from -5 T to 5 T at different temperature from 20 K to 350 K are presented in Figure 3.7. At temperature below 350 K, the magnetic hysteresis loops can be clearly observed, which further proves the ferromagnetic nature in this compound. The magnetic moments do not saturate with applied field up to 5 T, indicating large magneto-crystalline anisotropy in this compound. The magnetic hysteresis loop is suppressed with increasing of temperature and eventually disappear and become a straight line when temperature reaches 350 K. This result is consistent with the curie temperature $T_c \sim 320$ K we obtained from the $M(T)$ measurements since BaFe_2Se_4 should exhibit paramagnetic order when the temperature is higher than 320 K. From the $M(H)$ measurements, when under the same magnetic field, the value of magnetic moment increases with increasing of temperature from 20 K to 100 K, then decreases with further increasing of temperature up to 350 K. This result is also consistent with the $M(T)$ curves we showed in Figure 3.6.

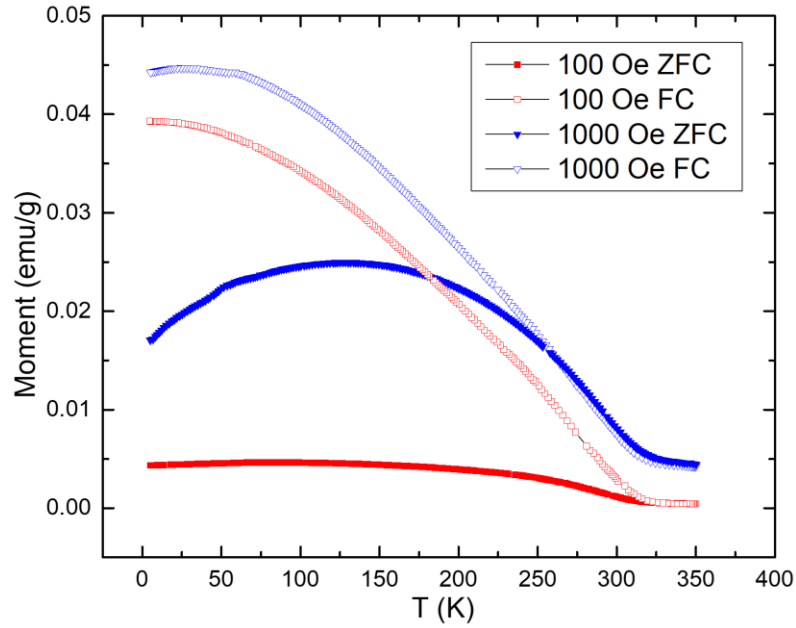


Figure 3.6: Magnetic moment as a function of temperature $M(T)$ of BaFe_2Se_4 measured with ZFC and FC methods. Typical irreversible behavior for a ferromagnetic order was observed in $M(T)$ measured with ZFC and FC histories.

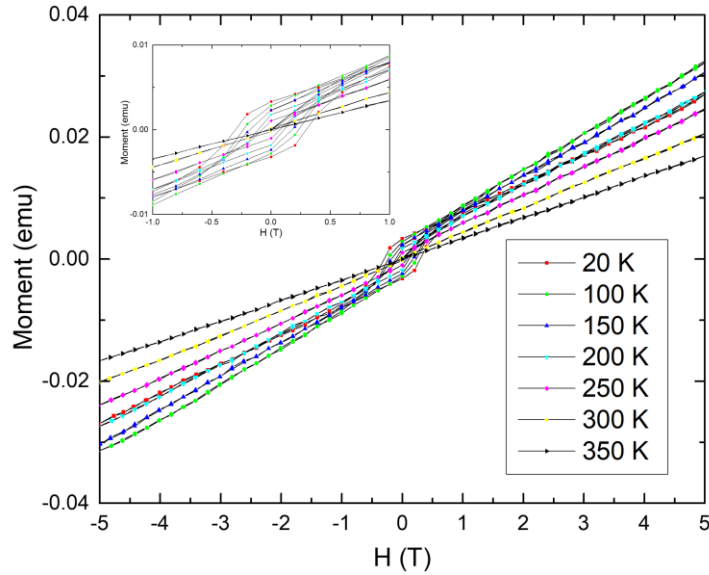


Figure 3.7: Magnetic moment as a function of field $M(H)$ of BaFe_2Se_4 measured at different temperatures from 20 K to 350 K. The magnetic hysteresis loop is suppressed with increasing temperature and eventually disappear and become a straight line when temperature reaches 350 K.

Based on the phase diagrams of electrons and holes doped cuprates iron-based superconductors reproduced from A. Charnukha's work [92]. The parent compounds typically exhibit antiferromagnetic ordering near zero doping, superconductivity emerges through either electrons or holes doping. As far as we know, no ferromagnetism has been reported so far in any iron-based superconductors, so if superconductivity can be induced in a material with ferromagnetic ground state, which will greatly broaden the understanding of the mechanism of unconventional superconductivity. Taking K doped BaFe_2As_2 compound $\text{Ba}_x\text{K}_{1-x}\text{Fe}_2\text{As}_2$ superconductors into consideration, the undoped parent compound BaFe_2As_2 is non-superconducting, superconductivity emerges through K doping to the Ba site (Holes doping) with $x \geq 0.15$, the transition temperature T_c increase with increasing of the K doping level x , reaches the maximum at $x = 0.4$ with $T_c \sim 38$ K before slowly decreasing to 3 K for the end member KFe_2As_2 [93]. Considering the Fe valence states in this system, which are $2+$ and $2.5+$ for two end members BaFe_2As_2 and KFe_2As_2 , respectively. If we plot the phase diagram of $\text{Ba}_x\text{K}_{1-x}\text{Fe}_2\text{As}_2$ systems with transition temperatures versus Fe valence count, as shown in Figure 3.9. Superconductivity emerges through holes doping in the region between Fe valence state of $2+$ (BaFe_2As_2) and $2.5+$ (KFe_2As_2). If we now take KFe_2As_2 as the parent compound, then either holes doping ($2.5+$ to $3+$) or electrons doping ($2.5+$ to $2+$) could possibly induce superconductivity in this compound. This phase diagram sheds a light on how to induce superconductivity in our BaFe_2Se_4 and $\text{K}_3\text{Fe}_2\text{Se}_4$ compounds, where Fe valence state is $3+$ and $2.5+$ for BaFe_2Se_4 and $\text{K}_3\text{Fe}_2\text{Se}_4$, respectively. According to the phase diagram, electrons doping with a medium doping level that decrease Fe valence states to the region between $3+$ and $2.5+$ for BaFe_2Se_4 , or $2.5+$ to $2+$ for $\text{K}_3\text{Fe}_2\text{Se}_4$, could possibly induce superconductivity. To test this hypothesis, we carried out electrons doping on these compounds. We doped Europium

(Eu) or Cerium (Ce) to the Ba site in BaFe_2Se_4 , and Ba to the K site in $\text{K}_3\text{Fe}_2\text{Se}_4$. We chose Eu and Ce, because of their relatively low and easier manipulated melting point ($T_m = 822\text{ }^\circ\text{C}$ and $799\text{ }^\circ\text{C}$, respectively), and similar atomic size with Ba atom which offers more chances to be doped to the parent compound. Superconductivity induced in $\text{Ba}_x\text{K}_{1-x}\text{Fe}_2\text{As}_2$ system makes Ba a good and natural candidate as electron carriers dopant for the $\text{K}_3\text{Fe}_2\text{Se}_4$ compound. We synthesized $\text{Ba}_{0.5}\text{Eu}_{0.5}\text{Fe}_2\text{Se}_4$, $\text{Ba}_{0.5}\text{Ce}_{0.5}\text{Fe}_2\text{Se}_4$, and $\text{K}_{2.5}\text{Ba}_{0.5}\text{Fe}_2\text{Se}_4$ samples, the Fe valence state in these doped compounds are $2.75+$, $2.75+$, $2.25+$, respectively, which all lie in the superconducting region in the phase diagram. However, all samples were found not superconducting from the resistivity measurements, as shown in Figure 3.11, which may due to the poor quality of the samples since the peaks in XRD patterns are broad and short, as shown in Figure 3.10. Some impurities were identified: CeSe_2 in $\text{Ba}_{0.5}\text{Ce}_{0.5}\text{Fe}_2\text{Se}_4$, EuSe and small amounts of unknown phases in $\text{Ba}_{0.5}\text{Eu}_{0.5}\text{Fe}_2\text{Se}_4$, and BaSe in $\text{K}_{2.5}\text{Ba}_{0.5}\text{Fe}_2\text{Se}_4$. The reaction temperature for all doped samples is set at $700\text{ }^\circ\text{C}$, which may not be sufficiently high, and the starting materials tend to form the more stable impurity phases at this temperature, which can be evidenced by the high intensity of impurity peaks in all doped samples. Preheated at much higher temperature ($\sim 1000\text{ }^\circ\text{C}$) prior to reaction temperature could be an essential step for a successful synthesis of doped samples. An optimized synthesis method needs to be developed in the future in order to successfully dope charge carriers to these compounds. The activation energy estimated from the resistivity measurements are $\sim 17.6\text{ meV}$ and $\sim 156.4\text{ meV}$ for $\text{Ba}_{0.5}\text{Ce}_{0.5}\text{Fe}_2\text{Se}$ and $\text{K}_{2.5}\text{Ba}_{0.5}\text{Fe}_2\text{Se}_4$, respectively, which is suppressed from $\sim 27.5\text{ meV}$ and $\sim 239.6\text{ meV}$ on parent compounds. Indicating that both doped samples become closer to a metallic state. We believe with the development of an optimized synthesis method superconductivity can be induced in these

compounds. $\text{Ba}_{0.5}\text{Eu}_{0.5}\text{Fe}_2\text{Se}_4$ is found to be more insulating than the parent compound which may be due to the isovalent substitution, since Eu is also common in 2+ valence state, so Eu doping does not shift the iron valence state into the superconducting region on the phase diagram.

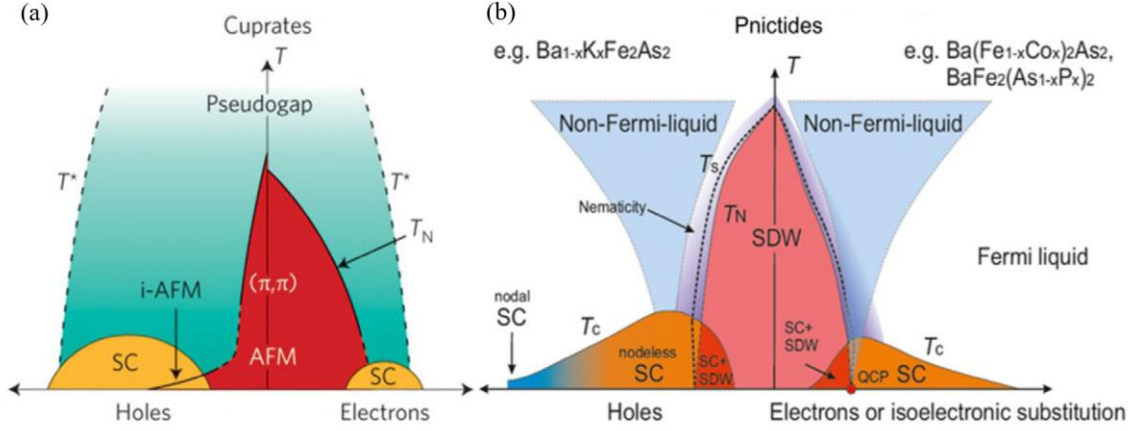


Figure 3.8: Phase diagram of the electron and hole doped cuprates and iron pnictides superconductors (Figure reproduced from Ref. [92]). The parent compounds typically exhibit magnetic ordering near zero doping, superconductivity emerges through either electrons or holes doping.

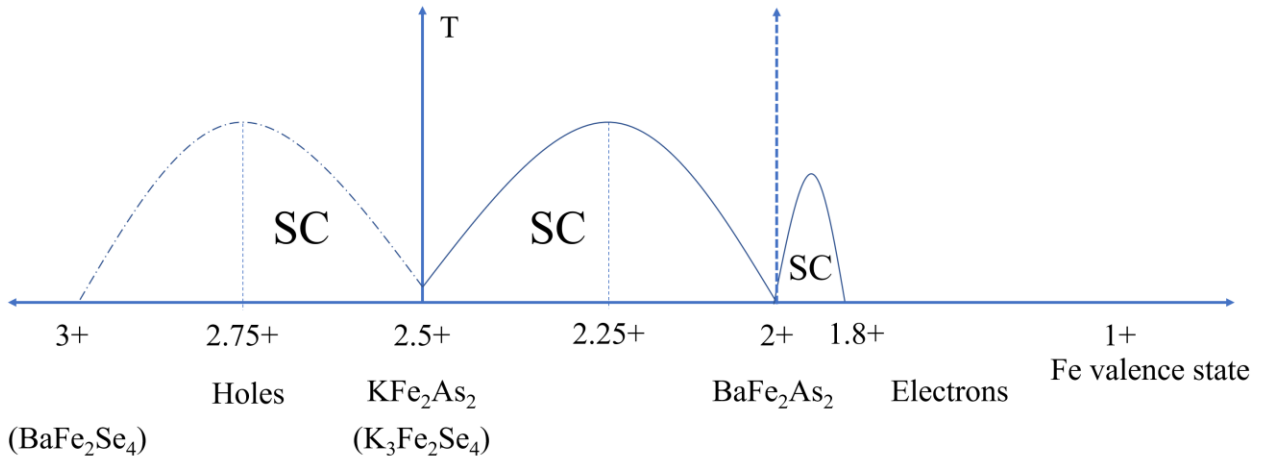


Figure 3.9: Superconducting phase diagram of KFe_2As_2 , Chemical doping that changes the Fe oxidation state to 2.75+ (hole doping) or 2.25+ (electron doping) has the highest possibility to make the compound superconducting.

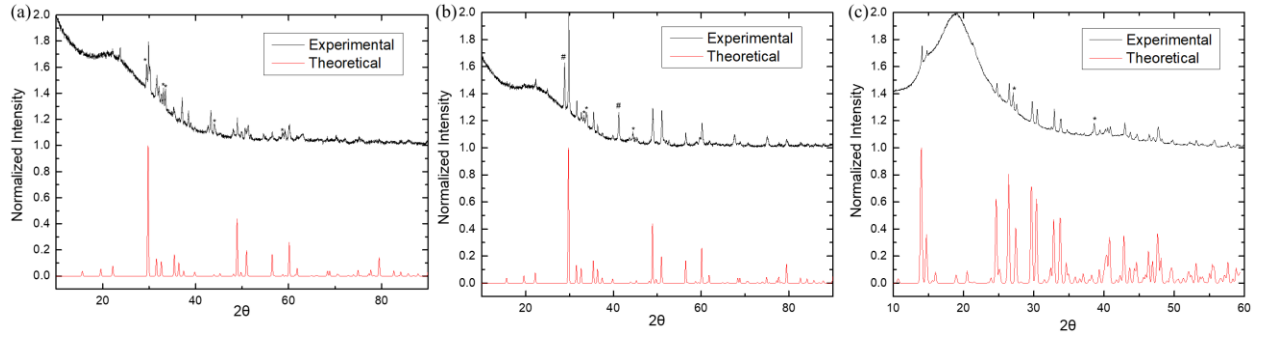


Figure 3.10: XRD patterns of doped samples (a) $\text{Ba}_{0.5}\text{Ce}_{0.5}\text{Fe}_2\text{Se}_4$, the impurity phase was identified as CeSe_2 (*) (b) $\text{Ba}_{0.5}\text{Eu}_{0.5}\text{Fe}_2\text{Se}_4$, the impurities are EuSe (#) and few unidentified peaks (c) $\text{K}_{2.5}\text{Ba}_{0.5}\text{Fe}_2\text{Se}_4$, the impurity phase was identified as BaSe (*).

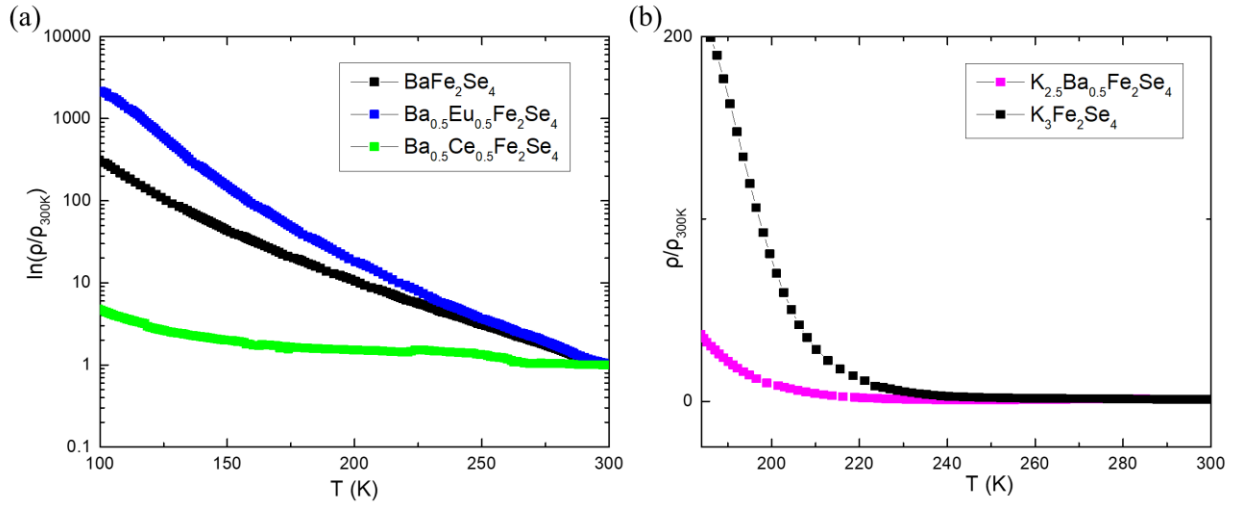


Figure 3.11: Normalized temperature dependence of resistivity on doped samples (a) $\text{Ba}_{0.5}\text{Ce}_{0.5}\text{Fe}_2\text{Se}_4$, $\text{Ba}_{0.5}\text{Eu}_{0.5}\text{Fe}_2\text{Se}_4$ (c) $\text{K}_{2.5}\text{Ba}_{0.5}\text{Fe}_2\text{Se}_4$.

CHAPTER 4

SUPERCONDUCTIVITY IN QUASI-1D Zr_5Ge_3 AND $A_2MO_3As_3$ ($A=K, RB$) SYSTEMS¹

4.1 Doping studies and superconductivity in transition metal doped Zr_5Ge_3 system

4.1.1 Introduction

Superconductivity was not observed at the current stage in the two quasi-1D iron chalcogenide materials we discussed in the previous chapter. We investigated another quasi-1D system family that contains large amounts of compounds. The early transition metal metal-rich compounds binary A_5B_3 compound, where A represents the transition metals and B represents the main group elements. This is a large family that contains tetragonal Cr_5B_3 -type and W_5Si_3 -type, orthorhombic Nb_5As_3 -type and Y_5Bi_3 -type, and hexagonal Mn_5Si_3 -type structures. The many A_5B_3 phases that exhibit the hexagonal Mn_5Si_3 -type structure and similar structural derivatives, will be an ideal model system for such searching attempts. In addition, cation/anion sites and interstitial sites various doping possibilities in this type of structure have made it to be a rich playground for a variety of physical phenomena such as superconductivity, ferro/antiferromagnetism. The Mn_5Si_3 -type structure features capped trigonal antiprismatic A_6B_6 chains interconnected by another linear chain of A. It is a quasi-one-dimensional (1D) system and has a nearly unique ability to bind diverse heteroatoms Z inside a 1D chain made from face sharing triangular antiprisms of A. In 2013, Lv et al first reported the discovery of superconductivity at 2.3 K in Zr_5Sb_3 [94], this is the first superconducting compound in the large compound family of Mn_5Si_3 -type structure. In 2015,

¹ Adapted with permission from S. Li, X. Liu, V. Anand, and B. Lv, Superconductivity and phase diagram in a transition metal doped Zr_5Ge_3 compound, *Supercond. Sci. Technol.* 31, 085001 (Published 19 June 2018). <https://doi.org/10.1088/1361-6668/aac6a1>. © IOP Publishing Ltd. All rights reserved.

Xie et al enhanced the superconducting transition temperature from 2.5 K to 5 K upon Ru doping at Sb site in Zr_5Sb_3 [95]. The doped compound $\text{Zr}_5\text{Sb}_{3-x}\text{Ru}_x$ has a structural transformation from the hexagonal Mn_5Si_3 -type to tetragonal W_5Si_3 -type. Moreover, several new $\text{A}_2\text{Cr}_3\text{As}_3$ ($\text{A} = \text{K}, \text{Rb}, \text{Cs}$) superconductors with the highest transition temperature ~ 6.1 K were reported [96-98]. These new $\text{A}_2\text{Cr}_3\text{As}_3$ superconductors crystalized in a similar structure, but without effective bonding between each Cr_6As_6 chain, thus making them quasi-one-dimensional superconductors having very high upper critical field. All these discoveries bring us the confidence that more superconductors will be discovered in this large Mn_5Si_3 -type structure family.

We had chosen Zr_5Ge_3 [99] as our parent compound to start with for inducing superconductivity in the Mn_5Si_3 -type family. Zr_5Ge_3 features capped trigonal antiprismatic Zr_6Ge_6 chains along the c-axis, which are subsequently interconnected by another linear chain of Zr, as shown in Figure 4.1. Different from $\text{A}_2\text{Cr}_3\text{As}_3$, where there is no effective bonding between Cr_6As_6 chains, in the Zr_5Ge_3 , the distance of Zr-Ge between the Zr_6Ge_6 and Zr linear chain is 2.83 Å, suggesting the weak but effective bonding between Zr_6Ge_6 and Zr linear chain, and the more pseudo-quasi-1D nature for Zr_5Ge_3 . Considering the crystal structure described above, there are three ways to change the electronic state at the Fermi surface of Zr_5Ge_3 through chemical doping. Firstly, directly dope transition metal to the Zr site, since Zr is also a transition metal, it should be compatible to do this replacement. Secondly, we can dope transition metals to the Ge site since Zr can form the same intermetallic structure with other transition metals like Zr_5Ir_3 and Zr_5Pt_3 [100]. Previous efforts have shown a successful example along this direction and a significant T_c enhancement in the Ru doped $\text{Zr}_5\text{Sb}_{3-x}\text{Ru}_x$ and $\text{Hf}_5\text{Sb}_{3-x}\text{Ru}_x$ system [101]. The last way is to take advantage of the octahedral interstitial sites formed by the Zr_6Ge_6 trigonal antiprism chains. Those unoccupied

interstitial $2b$ sites at the corner of the unit cell can host not only small atoms such as B, C, and O, but also bigger transition metal anions such as Bi, Zn, Ru, and Sb [102], which further add up the wide electronic tunability in this material.

We have doped Ru, Pt, Ir and Pd at three different sites (Zr site, Ge site and interstitial site) into the Zr_5Ge_3 system. We chose these elements because of inspiration from the successful enhancement of transition temperature through Ru doping in Zr_5Sb_3 system. Other elements such as Pt, Ir and Pd have very similar chemical properties and doping effects as Ru.

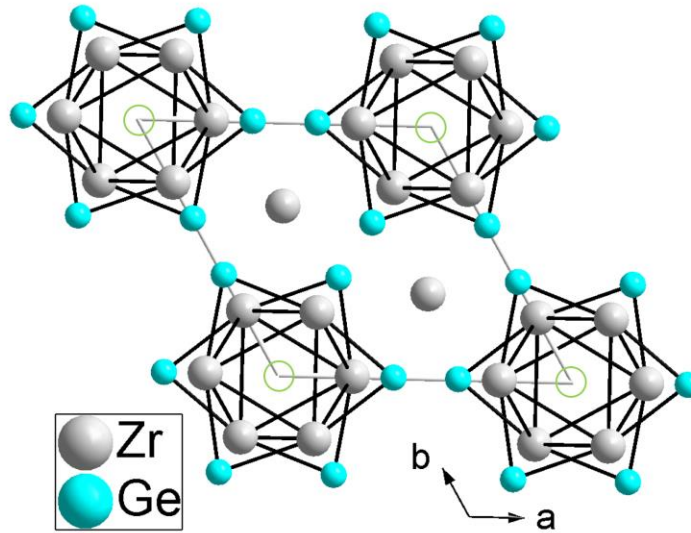


Figure 4.1: Projection of Zr_5Ge_3 structure along c directions. The small green circles at the corners of the unit cell show the octahedral interstitial $2b$ site formed by the trigonal antiprismatic Zr_6Ge_6 chain.

4.1.2 Experimental Procedures

Parent compound Zr_5Ge_3 and all transition metal doped compounds were synthesized by arc melting technique on a water-cooled copper hearth in a home-made arc furnace under argon-atmosphere, with Zr as oxygen getter. Zr foils (Alfa Aesar, 99.9+%), Ge lumps (Alfa Aesar, 99.99%), Ru powders (Alfa Aesar, 99.95%), Pt powders (Alfa Aesar, 99.9%), Ir powders (Alfa

Aesar, 99.95%), Pd pieces (Alfa Aesar, 99.8%) were used as starting chemicals. All samples were synthesized under the same condition. During the arc melting process, the melted samples were flipped and remelted several times to ensure the homogeneity of the samples. To avoid the formation of other binary or ternary compounds, the current was rapidly decreased to zero. The total weight loss is less than 1%, which indicates the successful synthesis of the samples. After the arc melting process, the sample ingots are sealed into the Nb tube first, and then sealed in an evacuated quartz tube then was heated in the furnace at 1100 °C for one week for further annealing to ensure the sample homogeneity.

4.1.3 Results and discussion

4.1.3.1 Ru doping

The XRD patterns and Rietveld refinement of Ru doped at different sites samples are shown in Figure 4.2 and Table 4.1.

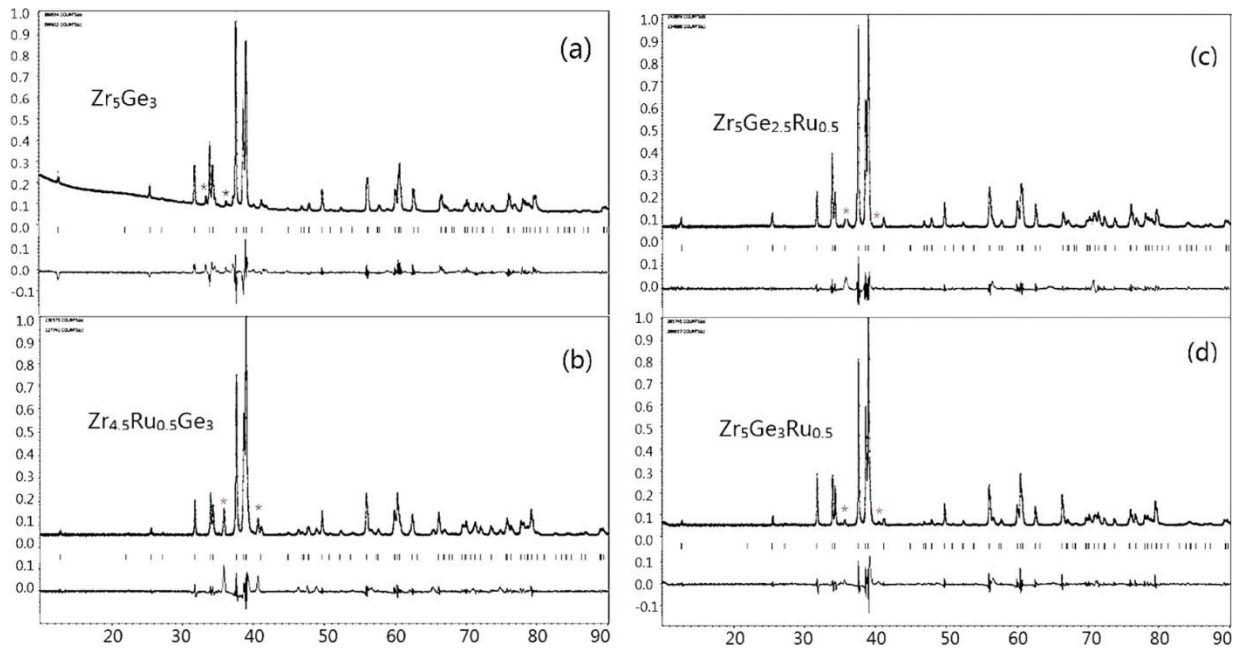


Figure 4.2: XRD patterns for four samples, small impurity peaks are marked by blue stars(as $ZrGe_2$) for Zr_5Ge_3 sample and red stars(as $ZrRuGe$) for Ru-doped Zr_5Ge_3 samples.

Table 4.1: Rietveld refinement data of the four samples

Compound	a (Å)	c (Å)	R_p	R_{wp}
Zr_5Ge_3	8.0485(9)	5.6127(6)	3.71%	5.87%
$Zr_{4.5}Ru_{0.5}Ge_3$	8.0832(6)	5.6511(5)	4.88%	8.20%
$Zr_5Ge_{2.5}Ru_{0.5}$	8.0445(5)	5.6105(4)	3.49%	6.28%
$Zr_5Ge_3Ru_{0.5}$	8.0556(7)	5.6234(5)	5.12%	9.75%

Our results show the synthesized samples adopt the hexagonal Mn_5Si_3 -type structure. The lattice parameters are increased significantly for Ru doped at the Zr site and interstitial site as expected, and slightly decreased when doped at the Ge site, which also indicate the successful doping of Ru atoms into the system. The high intensity and sharp peaks of XRD patterns, and the good refinement values of R_p and R_{wp} indicate the high sample quality of the materials. Small impurities of $ZrGe_2$ (less than 5%) were observed in the parent Zr_5Ge_3 samples. These impurities are suppressed with Ru doping, but a new impurity phase of $ZrRuGe$ arises in all of the $Zr_{4.5}Ru_{0.5}Ge_3$, $Zr_5Ge_{2.5}Ru_{0.5}$, and $Zr_5Ge_3Ru_{0.5}$ samples. The $ZrRuGe$ impurity is largest in the Zr site doped sample $Zr_{4.5}Ru_{0.5}Ge_3$ but is less than 5% in both $Zr_5Ge_{2.5}Ru_{0.5}$ and $Zr_5Ge_3Ru_{0.5}$ samples. SEM studies had been carried out on these samples and show rather homogeneous distribution of Ru in all of the samples. The Ru doping level is consistent with nominal composition from EDAX analysis for $Zr_{4.5}Ru_{0.5}Ge_3$, and $Zr_5Ge_{2.5}Ru_{0.5}$ samples.

The resistivity measurements of all four samples from 1.8 K to 300 K using a standard four-probe technique were performed on the PPMS-9T (Quantum Design), the results are shown in Figure 4.3. Resistivity is normalized to 300 K for a better comparison. The resistivity of all four samples

decreased with decreasing temperature as expected for a poor metal. With the additional Ru doping, the impurity scattering increased which causes the decrease of residual resistance ratio (RRR) value for the $\text{Zr}_{4.5}\text{Ru}_{0.5}\text{Ge}_3$, $\text{Zr}_5\text{Ge}_{2.5}\text{Ru}_{0.5}$, and $\text{Zr}_5\text{Ge}_3\text{Ru}_{0.5}$ samples. Both $\text{Zr}_5\text{Ge}_{2.5}\text{Ru}_{0.5}$ and $\text{Zr}_5\text{Ge}_3\text{Ru}_{0.5}$ samples show an almost linear relationship of resistivity with temperature, between 50 K to 250 K, which is different from the parent compound Zr_5Ge_3 , implying the possible enhancement of electron correlation upon doping where superconductivity may arise. Indeed, in the $\text{Zr}_5\text{Ge}_{2.5}\text{Ru}_{0.5}$ sample, a sudden resistivity drop below 5.7 K was observed, which is a characteristic of superconducting transition. Superconductivity, on the other hand, is absent in the $\text{Zr}_{4.5}\text{Ru}_{0.5}\text{Ge}_3$, $\text{Zr}_5\text{Ge}_3\text{Ru}_{0.5}$ samples. Since the impurity phase in the parent compound Zr_5Ge_3 is not superconducting and all the Ru doped samples do have the same impurity phase ZrRuGe , and no superconductivity signal is detected in the $\text{Zr}_{4.5}\text{Ru}_{0.5}\text{Ge}_3$ system which contains the highest amount of impurity phase, we excluded the possibility of that superconductivity is caused by ZrRuGe in the $\text{Zr}_5\text{Ge}_{2.5}\text{Ru}_{0.5}$ system.

The magnetic measurements of the superconducting $\text{Zr}_5\text{Ge}_{2.5}\text{Ru}_{0.5}$ sample was then carried out to check whether such superconductivity is coming from bulk sample, the results are shown in Figure 4.4. The temperature dependence of magnetic susceptibility was measured at 10 Oe using ZFC/FC methods. From ZFC curve, a large shielding volume fraction about 1.5 before the correction of demagnetization effect at 10 Oe was obtained, which indicate bulk superconductivity of the sample. As the magnetic field increases, a dramatic change of transition temperature at low fields was not observed. The M-H loop at 2 K shows the clear type-II superconductor characteristics, and the lower critical field H_{c1} is less than 100 Oe. The upper critical field of this newly discovered superconductor is noticeably much higher than the first known Zr-based superconductor with the

same Mn_5Si_3 -type found in Zr_5Sb_3 , however it is lower than the H_{c2} of $\text{A}_2\text{Cr}_3\text{As}_3$ ($\text{A}=\text{K}, \text{Rb}, \text{Cs}$) superconductors which are more quasi-one-dimensional.

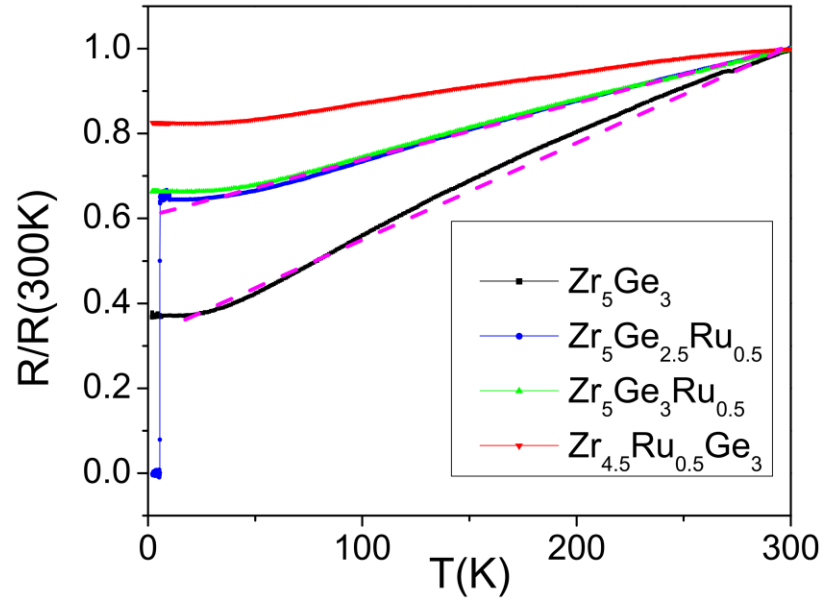


Figure 4.3: The normalized temperature dependent resistivity data for four different samples with a clear superconducting transition at 5.7 K observed in the $\text{Zr}_5\text{Ge}_{2.5}\text{Ru}_{0.5}$ sample. Two dotted straight lines were used as the guidance to compare normal state temperature dependence resistivity changes upon doping for parent Zr_5Ge_3 and doped $\text{Zr}_5\text{Ge}_{2.5}\text{Ru}_{0.5}$ samples.

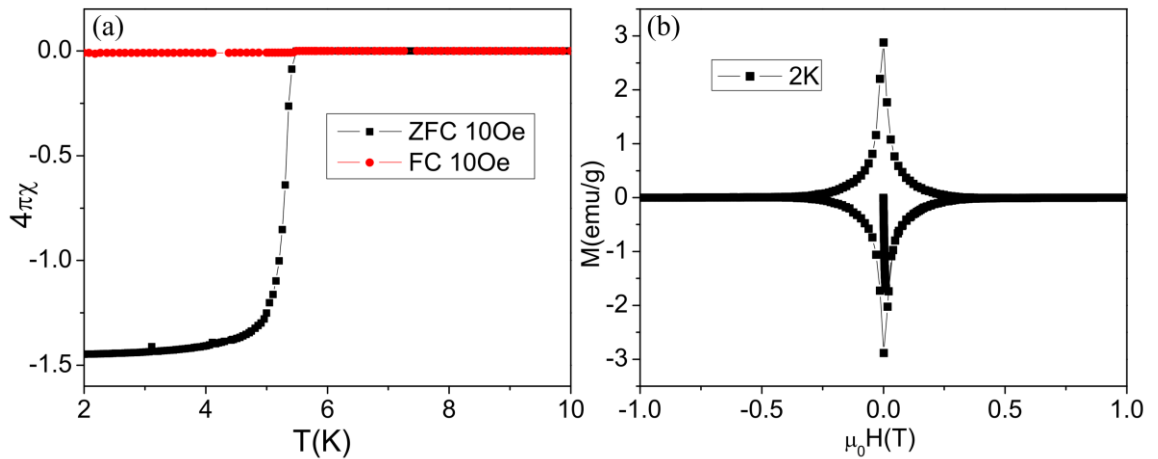


Figure 4.4: (a) Temperature dependence of the DC magnetization measured in the ZFC mode and the FC mode at 10 Oe. (b) The MH Loop measured with a field sweeping rate of 50 Oe/s at 2 K, which shows a type-II superconductor behavior.

Magnetoresistance $\rho(T,H)$ was further measured to determine the upper critical field. The magneto resistivity data is shown in Figure 4.5. It shows that with the highest applied magnetic field 7 T, a resistivity drop below 2 K is still visible. We took 10% resistivity drop as criteria, using the Werthamer-Helfand-Hohenberge (WHH) theory to extrapolate the H_{c2} . The calculated upper critical field is 8.2 T through the WHH fitting, shown as the inset of Figure 4.5, which is comparable with the Pauli limit about 10 T corresponding to $1.84T_c$. One possible reason for such a high upper critical field could be that the Ru doping to the Ge site has weakened the bonding between Zr2 atoms and Zr₆Ge₆ chains, thus making the structure more anisotropy/one dimensional.

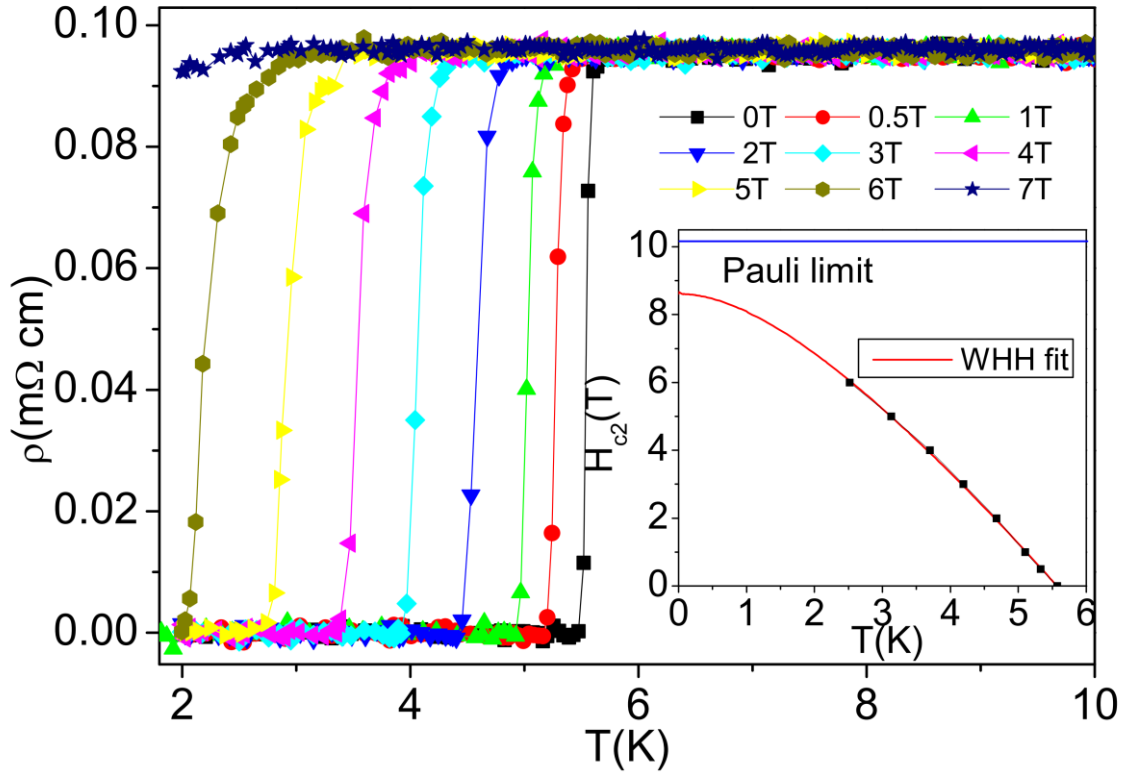


Figure 4.5: Temperature dependence of resistivity at different magnetic fields: 0, 0.5, 1.0, 2.0, 3.0, 4.0, 5.0, 6.0, and 7.0 T. The inset shows the WHH fitting of the temperature dependence of the critical field with $H_{c2}(T)$ ($90\% \rho_n$), where the straight line shows the Pauli limitation.

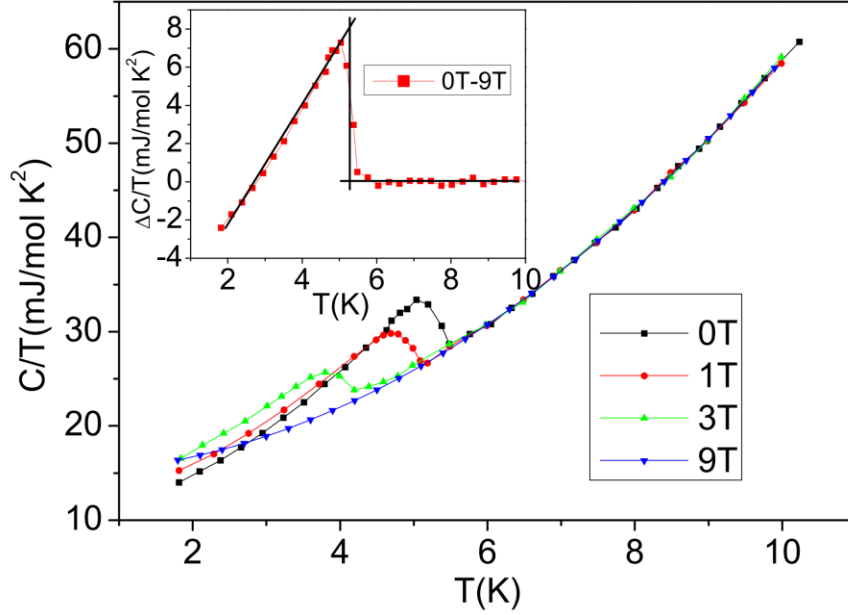


Figure 4.6: Field dependence of the heat capacity data, the inset shows the electronic specific data. The specific heat measurements of the superconducting $\text{Zr}_5\text{Ge}_{2.5}\text{Ru}_{0.5}$ sample are shown in Figure 4.6. The specific heat was measured from 1.8 K to 10 K at different magnetic field from 0 T to 9 T. The bulk superconductivity in $\text{Zr}_5\text{Ge}_{2.5}\text{Ru}_{0.5}$ can be further demonstrated by the pronounced specific heat anomaly in Figure 4.6. Through subtracting the specific heat data at 0 T with normal state specific heat data at 9 T, the electronic contributions in the superconducting state can be determined. A superconducting specific heat anomaly appears at 5.4 K with the specific heat jump of about $\Delta C/T_c = 8 \text{ mJ/mol K}^2$ at zero magnetic field. From the Debye fitting of normal specific heat data at 9 T using $C = \gamma_n T + \beta T^3$, $\gamma_n = 14.96 \text{ mJ/mol K}^2$ and $\beta = 0.44 \text{ mJ/mol K}^4$ can be obtained, which corresponds to the electronic Sommerfeld coefficient and Debye temperature respectively. The Debye temperature can be deduced from the β value through the relationship $\Theta_D = (12\pi^4 K_B N_A Z / 5\beta)^{1/3}$, where $N_A = 6.02 \times 10^{23} \text{ mol}^{-1}$ is the Avogadro constant, and Z is the number of atoms in the molecule. The obtained Debye temperature is about 314 K. From γ_n

and $\Delta C/T_c$, the value of $\Delta C/\gamma_n T_c$ is about 0.53, which is much smaller than the BCS value 1.43. The small value of $\Delta C/\gamma_n T_c$ reveals that the $\text{Zr}_5\text{Ge}_{2.5}\text{Ru}_{0.5}$ is a superconductor with a rather weak electron-phonon coupling. Consider the aforementioned enhancement of electron correction and high upper critical field. All these indicate possible unconventional superconductivity in this system.

4.1.3.2 Pt, Ir and Pd doping

Superconductivity was successfully induced through Ru-doped at Ge site in Zr_5Ge_3 system with superconducting transition temperature $T_c \sim 5.4$ K. This encouraged us to dope other elements that have very similar chemical properties and doping effects as Ru such as Pt, Ir, and Pd to the Zr_5Ge_3 system. The XRD patterns of doped compounds are shown in Figure 4.7. The high intensity peak in XRD patterns show high quality of the samples. Small impurities (ZrGe_2) were found in the parent compound Zr_5Ge_3 , as well as (ZrPd) in the $\text{Zr}_5\text{Ge}_{2.5}\text{Pd}_{0.5}$, and others are XRD pure phase. The good refinement value of R_p and R_{wp} indicate all samples adopt the hexagonal Mn_5Si_3 -type structure.

The resistivity measurements of all samples from 1.9 K to 300 K are shown in Figure 4.8 (a). Superconductivity is only observed in the Pt doped sample $\text{Zr}_5\text{Pt}_{0.5}\text{Ge}_{2.5}$, with superconducting transition temperature $T_c \sim 2.8$ K. Superconductivity remains absent in the Ir, Pd doped samples. Pt was then further doped at Zr site and interstitial site in Zr_5Ge_3 parent compound, but still only the Ge site doped sample shows superconductivity. The Zr site doped sample $\text{Zr}_{4.5}\text{Pt}_{0.5}\text{Ge}_3$ and the interstitial site doped sample $\text{Zr}_5\text{Ge}_3\text{Pt}_{0.5}$ were found to be non-superconducting at our lowest measured temperature (Figure 4.8 (b)). Consider our previous Ru doped at Ge site sample $\text{Zr}_5\text{Ge}_{2.5}\text{Ru}_{0.5}$ is also superconducting, which indicate that Pt, similar to Ru, is critical for the

induced superconductivity in Zr_5Ge_3 system. The Ge-Ru and Ge-Pt pairing could be essential for the superconductivity in the Zr_5Ge_3 compound, similar to the observation found in the $\text{Zr}_5\text{Sb}_{3-x}\text{Ru}_x$ and $\text{Hf}_5\text{Sb}_{3-x}\text{Ru}_x$ compounds.

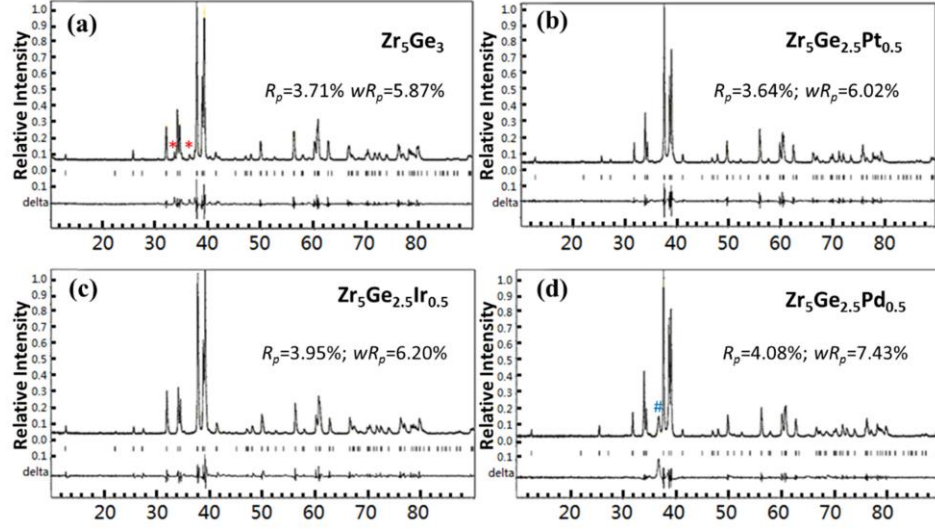


Figure 4.7: XRD patterns for (a) Zr_5Ge_3 , (b) $\text{Zr}_5\text{Ge}_{2.5}\text{Pt}_{0.5}$, (c) $\text{Zr}_5\text{Ge}_{2.5}\text{Ir}_{0.5}$, and (d) $\text{Zr}_5\text{Ge}_{2.5}\text{Pd}_{0.5}$ samples. The small impurity peaks are marked by * (as ZrGe_2) in Zr_5Ge_3 sample, and # (as ZrPd phase) for $\text{Zr}_5\text{Ge}_{2.5}\text{Pd}_{0.5}$ sample.

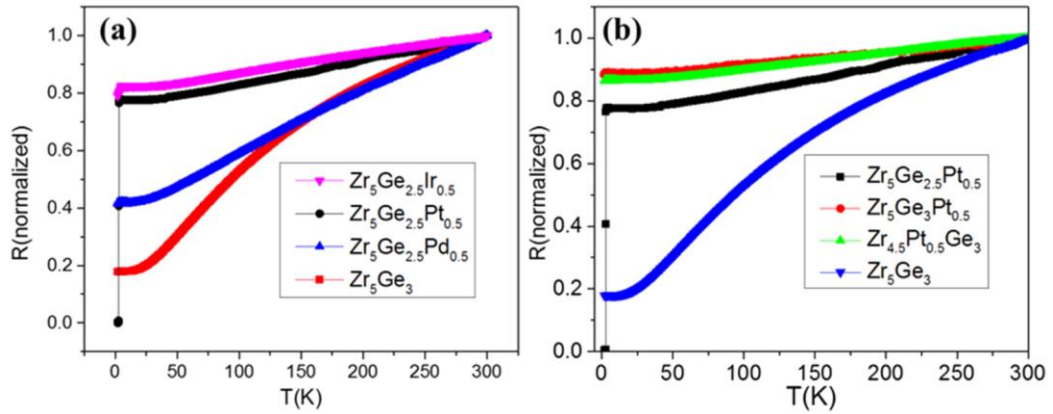


Figure 4.8: Normalized temperature dependent resistivity data for different transition metal doped $\text{Zr}_5\text{Ge}_{3-x}\text{M}_x$ samples where only a Pt doped sample shows a superconducting behavior, (b) normalized temperature dependent resistivity data for different doped Zr_5Ge_3 samples with the same Pt amount but at a different site.

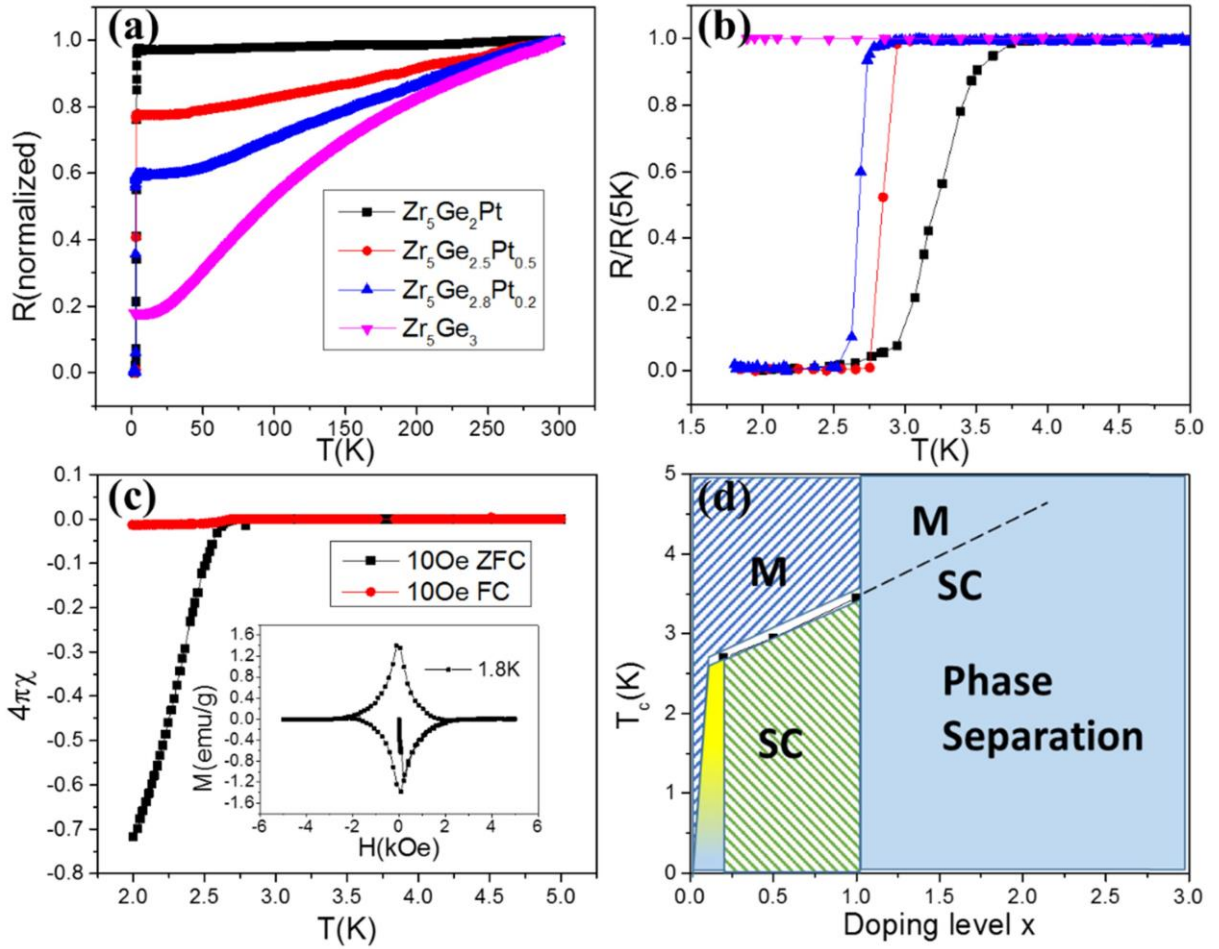


Figure 4.9: (a) Normalized temperature dependent resistivity data for Pt doped $\text{Zr}_5\text{Ge}_{3-x}\text{Pt}_x$ samples with different doping level ($x = 0, 0.2, 0.5$ and 1.0); (b) the superconducting transition for different samples on an enlarged scale between 1 and 5 K; (c) magnetization measurement data in ZFC and FC modes at 10 Oe for the $\text{Zr}_5\text{Ge}_{2.5}\text{Pt}_{0.5}$ sample, the inset shows the M - H loop at 1.8 K, (d) superconducting phase diagram of $\text{Zr}_5\text{Ge}_{3-x}\text{Pt}_x$. The superconductivity might already be induced in the gradient yellow area ($x < 0.2$), with T_c below 2 K which is below our lowest measurable temperature.

The fact that Zr_5Pt_3 crystallizes in the same Mn_5Si_3 -type structure as Zr_5Ge_3 has allowed us to carry out systematic doping studies and explore the superconducting phase diagram of the $\text{Zr}_5\text{Ge}_{3-x}\text{Pt}_x$ system. We synthesized several doped samples $\text{Zr}_5\text{Ge}_{3-x}\text{Pt}_x$ with $x = 0, 0.2, 0.5, 1$, and 1.2 , which are correspondent to doping levels of 0%, 6.7%, 16.7%, 33.3%, and 40% respectively. A clear peak broadening was observed, and some small impurities start to emerge at $x = 1$ for the

Zr₅Ge₂Pt sample, indicating that phase separation starts occurring beyond this doping level. The formation of Zr₅Pt₃ phase occurs when $x > 1$, The Zr₅Pt₃ is known as a superconductor with T_c at 7.2 K, which essentially affects our analysis. Therefore, we only focus on the doped samples with $x \leq 1$ for our following characterizations. From the resistivity measurements of all Pt doped samples, as shown in Figure 4.9 (a). They all show superconducting transition, and the transition temperature T_c of each sample increase as the doping level increases from 2.6 K in Zr₅Ge_{2.8}Pt_{0.2} to 3.5 K in Zr₅Ge₂Pt. The slight broader transition (~ 0.5 K) in the Zr₅Ge₂Pt as shown in Figure 4.9 (b) is likely due to the small impurities in the samples. From the temperature dependence of magnetic susceptibility of Zr₅Ge_{2.5}Pt_{0.5} at 10 Oe and 2 K as shown in Figure 4.9 (c), the shielding volume fraction derived from ZFC and FC curves is about 0.7, since the ZFC curve does not turn flat at the lowest temperature 2 K, so the actual shielding volume fraction value should be greater than 0.7. This indicate that the superconductivity does come from bulk sample. The M-H loop at 1.8 K shows this is a type-II superconductor, the lower critical field H_{c1} is less than 20 Oe. Based on the resistivity and magnetic measurements data, the phase diagram of Zr₅Ge_{3-x}Pt_x was proposed, as shown in Figure 4.9 (d). It shows only a small doping level ($x \leq 1$) is sufficient to induce superconductivity, the transition temperature T_c shows almost linear relation with the doping level x . When $x > 1$, the phase separation of Zr₅Pt₃ occurs. Since Zr₅Pt₃ is also a superconductor with transition temperature $T_c \sim 7.2$ K, the superconducting transition temperature will continue to increase with the increase of doping level x can be expected. The magnetoresistance measurement result of Zr₅Ge_{2.5}Pt_{0.5} is shown in Figure 4.10 (a). The upper critical field of Zr₅Ge_{2.5}Pt_{0.5} that we extrapolate from the magnetoresistance measurement using WHH fit is about 4.3 T, as shown in Figure 4.10 (b).

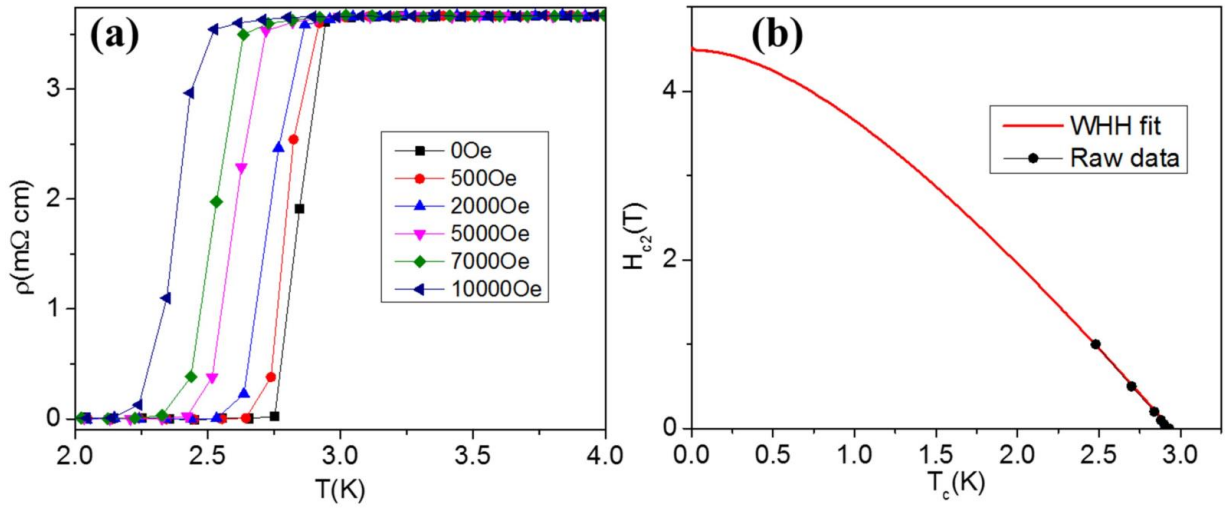


Figure 4.10: (a) Field dependence resistivity data at low temperature for $\text{Zr}_5\text{Ge}_{2.5}\text{Pt}_{0.5}$ sample, and (b) the upper critical field $H_{c2}(T)$ and its fitting by the WHH theory.

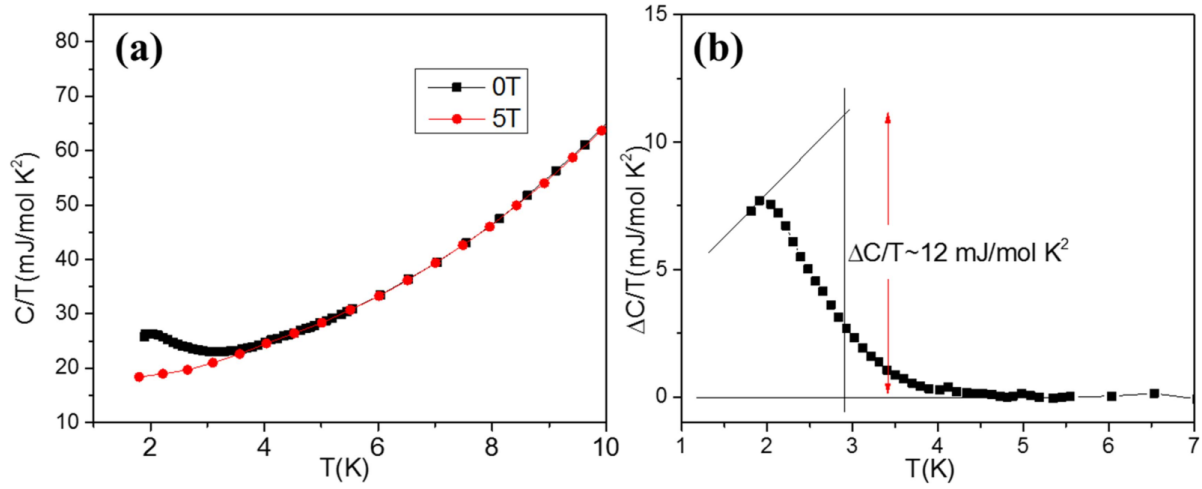


Figure 4.11: (a) Heat capacity data of $\text{Zr}_5\text{Ge}_{2.5}\text{Pt}_{0.5}$ sample at different magnetic field where a clear specific heat jump is visible below 3 K at zero-field; (b) the difference of electronic specific heat data between the normal state and superconducting state of $\text{Zr}_5\text{Ge}_{2.5}\text{Pt}_{0.5}$ sample.

The heat capacity of $\text{Zr}_5\text{Ge}_{2.5}\text{Pt}_{0.5}$ sample was further measured from 1.8 K to 10 K at 0 T and 5 T magnetic field, as shown in Figure 4.11. Through subtracting the superconducting state data at 0 T with the normal state data at 5 T. A specific heat anomaly around 2.5 K with the specific heat

jump of about $\Delta C/T_c = 12 \text{ mJ/molK}^2$ at zero magnetic field can be observed. From the Debye fitting of normal state data at 5 T using $C = \gamma_n T + \beta T^3$, $\gamma_n = 16.15 \text{ mJ/molK}^2$ and $\beta = 0.48 \text{ mJ/molK}^4$ can be obtained, which corresponds to the electronic Sommerfeld coefficient and Debye temperature respectively. The Debye temperature can be deduced from the β value through the relationship $\theta_D = (12\pi^4 K_B N_A Z / 5\beta)^{1/3}$, where $N_A = 6.02 \times 10^{23} \text{ mol}^{-1}$ is the Avogadro constant, and Z is the number of atoms in the molecule. The obtained Debye temperature is about 325 K. From γ_n and $\Delta C/T_c$, the value of $\Delta C/\gamma_n T_c$ is about 0.72, which is much smaller than the BCS value 1.43. The small value of $\Delta C/\gamma_n T_c$ also indicates that the $\text{Zr}_5\text{Ge}_{2.5}\text{Pt}_{0.5}$ is a superconductor with a rather weak electron-phonon coupling.

4.2 Synthesis and characterization of MoAs-based quasi-1D $\text{A}_2\text{Mo}_3\text{As}_3$ (A = K, Rb) compounds

4.2.1 Introduction

The Zr_5Ge_3 compound in the previous section has shown to be a rich playground searching for new superconductors. If we replace the Zr1 atoms with Mo atoms, Zr2 atoms with Alkali metal (K, Rb) atoms, and Ge atoms with As atoms in the crystal structure of Zr_5Ge_3 , the 1D chain of Zr_6Ge_6 will be transformed to 1D Mo_6As_6 chain, separated by alkali metal atoms. The obtained new structure is the crystal structure of a new family of quasi-1D compounds, the 233-type MoAs-based $\text{A}_2\text{Mo}_3\text{As}_3$ (A = Alkali metal) compounds. Different from Zr_5Ge_3 , there is no effective bonding between each Mo_6As_6 chain, thus making them more quasi-1D than Zr_5Ge_3 . Both Zr_5Ge_3 and $\text{A}_2\text{Mo}_3\text{As}_3$ compounds adopted hexagonal structure that shares many similarities with another well-known $\text{M}_2\text{Mo}_6\text{X}_6$ (X = S, Se, or Te, M = metal) (e.g. $\text{K}_2\text{Mo}_6\text{Se}_6$) compounds family [55,56,103-105]. Although the 1D chain Mo_6X_6 is isostructural to the 1D chain of Mo_6As_6 , the

Mo_6X_6 chain rotates a small angle around the c axis compared to the Mo_6As_6 chain. This leads to a different space group, $P6_3/m$ (176) for $\text{M}_2\text{Mo}_6\text{X}_6$ and $P\bar{6}m2$ (187) for $\text{A}_2\text{Cr}_3\text{As}_3$. Interestingly, the crystal structure of $\text{M}_2\text{Mo}_6\text{X}_6$ compounds can be transformed from the famous Chevrel phase compounds $\text{M}_x\text{Mo}_6\text{X}_8$ (x varying from 0 to 4) [43-51,53,106], which is a large family contains a large number of superconductors that were discovered back in 1970s. $\text{M}_2\text{Mo}_6\text{X}_6$ form when Mo_6X_8 clusters in $\text{M}_x\text{Mo}_6\text{X}_8$ linearly connecting to form a 1D chain structure. Figure 4.12 shows a similar structure among these four compounds family. These 233-type compounds have attracted great research interest due to the quasi-1D nature of their crystal structure. Unconventional superconductivity was also reported on some compounds belong to this family.

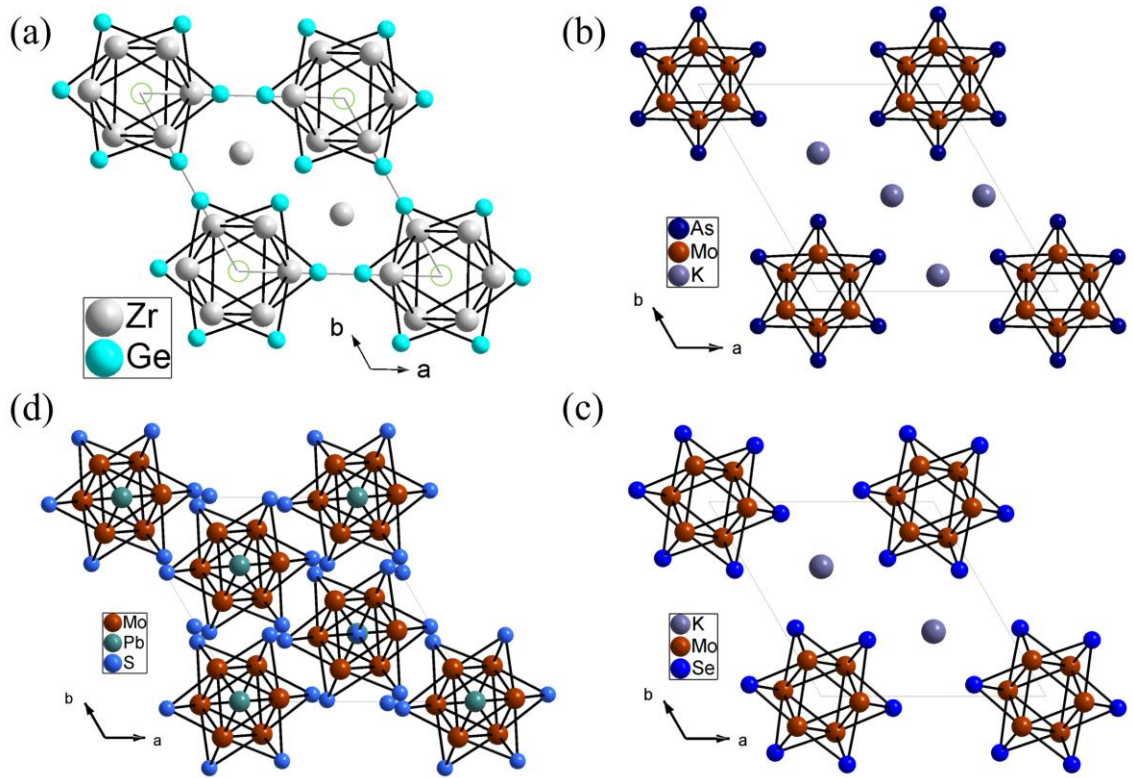


Figure 4.12: Crystal structure of (a) Zr_5Ge_3 (b) $\text{K}_2\text{Mo}_3\text{As}_3$ (c) $\text{K}_2\text{Mo}_6\text{Se}_6$ (d) PbMo_6S_6 . Zr_5Ge_3 , $\text{K}_2\text{Mo}_3\text{As}_3$, and $\text{K}_2\text{Mo}_6\text{Se}_6$ all adopt very similar hexagonal quasi-1D structure, which can be transformed from the crystal structure of well-known Chevrel phases.

Superconductivity was first discovered in 233-type CrAs-based compounds. In 2015, quasi-1D chromium pnictide $A_2Cr_3As_3$ ($A = K, Rb, \text{ or } Cs$) compounds were reported to be superconducting with $T_c \sim 6.1$ K [96-98]. Superconductivity was also discovered in $Na_2Cr_3As_3$ with $T_c \sim 8.6$ K in 2018 [107]. Some interesting phenomena and possible unconventional superconductivity were discovered from its physical property measurements. A strong electron correlation was indicated by the large electronic specific heat coefficient and linear temperature dependence of resistivity which is a typical behavior of non-fermi liquid. An upper critical field higher than the Pauli limit indicates possible unconventional superconductivity in such quasi-1D materials [108-115]. Later on, quasi-1D ACr_3As_3 (K, Rb) compounds, which have identical crystal structure with $M_2Mo_6X_6$ compounds were also reported to be superconducting with a transition temperature of 5 K and 7.3 K for KCr_3As_3 and $RbCr_3As_3$, respectively [116,117] through de-intercalation of alkali metal from the $K_2Cr_3As_3$ and $Rb_2Cr_3As_3$ compounds. Very recently, the first superconductor in MoAs-based ternary compounds family $K_2Mo_3As_3$ was discovered to be superconducting at 10.4 K [118], then superconductivity in $Rb_2Mo_3As_3$ and $Cs_2Mo_3As_3$ was also discovered with transition temperature at 10.6 K and 11.5 K, respectively [111]. Since all MoAs-based superconductors are extremely sensitive in air, a good quality sample of these compounds is difficult to be experimentally synthesized and is still lacking for researchers up to date. We synthesized the $K_2Mo_3As_3$ and $Rb_2Mo_3As_3$ polycrystalline samples, superconducting transitions were confirmed for both samples from the temperature dependence of magnetic susceptibility measurement. Resistivity measurement and magnetoresistance measurements were carried out on the $Rb_2Mo_3As_3$ sample to determine the upper critical field.

4.2.2 Experimental procedures

$K_2Mo_3As_3$ and $Rb_2Mo_3As_3$ polycrystalline samples were prepared through high temperature solid state reaction. Elemental K pieces (Alfa Aesar, 99.5%), Rb pieces (Alfa Aesar, 99.75%), Mo powders (Alfa Aesar, 99.9%), As lumps (Alfa Aesar, 99.999%) were used as starting materials. The surface of K and Rb was carefully scraped to remove the oxidation prior to use. Precursors KAs and RbAs were synthesized first by mixing elemental K or Rb and As with stoichiometric ratio in the alumina crucible, then vacuum sealed in quartz tube. The reaction was carried out at 250 °C for 20 hours in a box furnace. In order to prevent tubes breaking due to the violent reaction of K or Rb with As, the total amount of KAs and RbAs in one tube is limited to ~ 500 mg, and heating rate from room temperature to the reaction temperature 250 °C should be very slow. The obtained precursors KAs or RbAs was then finely ground to powder and mixed with elemental Mo and As with stoichiometric ratio of 2.3 : 3 : 0.7. The 15% excess of KAs or RbAs is necessary to compensate for the loss of KAs or RbAs during the reaction. The mixture then was pressed into a pellet. The pellet was placed into an Nb tube with arc welding in Ar atmosphere and the Nb tube was vacuum sealed into a quartz tube. The reaction was carried out at 850 °C for 50 hours and followed by furnace cool. Regrinding and annealing at 850 °C is necessary to improve the sample quality. Both $K_2Mo_3As_3$ and $Rb_2Mo_3As_3$ are extremely sensitive to moisture and air, all samples were kept and manipulated in the glove box Ar atmosphere before the measurement.

4.2.3 Results and discussion

The XRD patterns of the $K_2Mo_3As_3$ and $Rb_2Mo_3As_3$ powder samples are presented in Figure 4.13, show that both synthesized materials are XRD pure phase within the resolution of the measurement. All peaks can be indexed with the results from the theoretical pattern. The hump

between $\sim 15^\circ$ and 25° is due to the vacuum grease that protecting the powder during the measurement. The Both $\text{K}_2\text{Mo}_3\text{As}_3$ and $\text{Rb}_2\text{Mo}_3\text{As}_3$ compounds adopt quasi-1D hexagonal crystal structure and space group of $P\bar{6}m2$ (187), with lattice parameters $a = 10.145$ (5) Å and $c = 4.453$ (8) Å for $\text{K}_2\text{Mo}_3\text{As}_3$ and $a = 10.432$ (1) Å and $c = 4.4615$ (6) Å for $\text{Rb}_2\text{Mo}_3\text{As}_3$. The crystal structure of $\text{K}_2\text{Mo}_3\text{As}_3$ is presented in Figure 4.12 (b), the 1D chains of Mo_6As_6 are along the c -axis separated by K atoms.

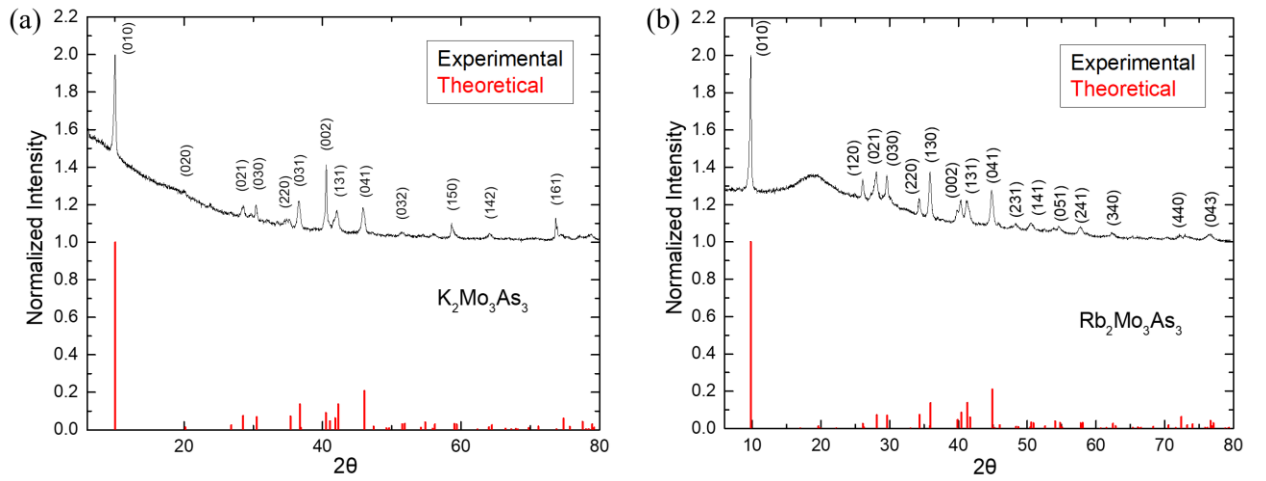


Figure 4.13: XRD patterns of $\text{K}_2\text{Mo}_3\text{As}_3$ and $\text{Rb}_2\text{Mo}_3\text{As}_3$ samples

The temperature dependencies of dc magnetization from 2 K to 12 K for $\text{K}_2\text{Mo}_3\text{As}_3$ and $\text{Rb}_2\text{Mo}_3\text{As}_3$ using ZFC and FC modes under the static magnetic field of 10 Oe are presented in Figure 4.14. A clear diamagnetic shift is observed below 10.4 K for $\text{K}_2\text{Mo}_3\text{As}_3$ and 10.6 K for $\text{Rb}_2\text{Mo}_3\text{As}_3$, which are consistent with previously reported transition temperatures. However, the transition is not as sharp as previous results, which may be to the slight oxidation of samples during transfer between glovebox and vacuum sealing line or arc-welding unit since both samples are extremely sensitive to air and moisture. The volume fraction derived from the ZFC curve is 180% for $\text{K}_2\text{Mo}_3\text{As}_3$ before the demagnetization correlation and 70% for $\text{Rb}_2\text{Mo}_3\text{As}_3$. The large shielding

volume indicates bulk superconductivity nature of these samples. There is an extra superconducting transition around 5 K for the $\text{K}_2\text{Mo}_3\text{As}_3$, which may come from some amorphous phases due to inhomogeneity of the sample, and the ~ 5 K transition is suppressed with longer time annealing. Future works need to be developed to identify and understand this extra transition.

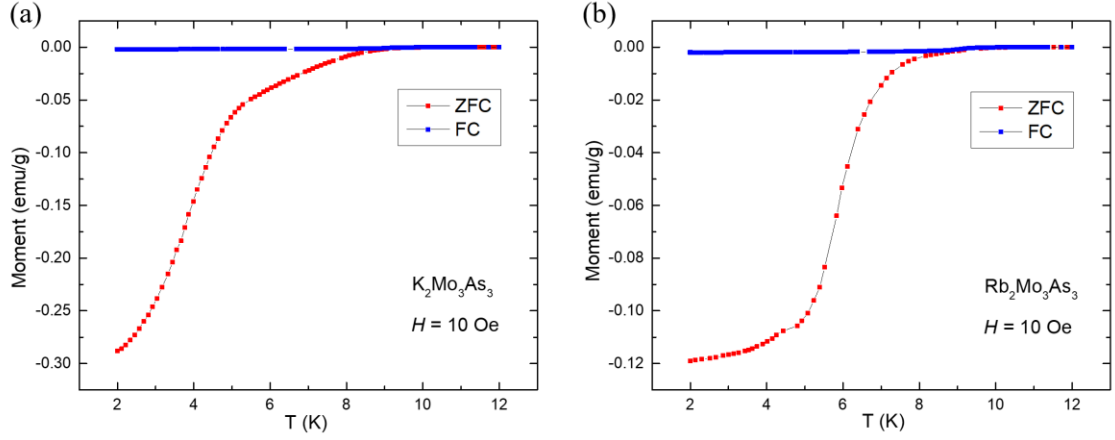


Figure 4.14: Temperature dependence of the DC magnetization measured in the ZFC and FC mode at 10 Oe for (a) $\text{K}_2\text{Mo}_3\text{As}_3$ (b) $\text{Rb}_2\text{Mo}_3\text{As}_3$ samples

The typical temperature dependence of electrical resistance for $\text{Rb}_2\text{Mo}_3\text{As}_3$ sample is presented in Figure 4.15. The sample exhibit sharp superconducting transition at low temperature with $T_c \sim 10.6$ K, which consistent with the dc magnetic susceptibility measurement. The sharp superconducting transition indicates a good quality of the $\text{Rb}_2\text{Mo}_3\text{As}_3$ sample.

The magnetoresistance $\rho(T, H)$ was further measured to determine the upper critical field. The electrical resistivity below 16 K was measured with temperature sweeping for $\text{Rb}_2\text{Mo}_3\text{As}_3$ sample under constant magnetic fields with the direction perpendicular to the electrical current. The magnetic fields were set from 0 T to 9 T with 1 T interval, the results are shown in Figure 4.16 (a). The superconducting transition temperature is decreasing with increases of the magnetic field. However, the magnetic field up to 9 T does not completely suppress the superconducting

transition, indicate a large upper critical field of the sample. We took 10% resistivity drop as criteria, using the WHH theory to extrapolate the H_{c2} . The calculated upper critical field is 27 T through WHH fitting, shown in Figure 4.16 (b), which is comparable with the Pauli limit about 19.5 T corresponding to $1.84T_c$, and higher than previously reported value of 23.4 T [111], further indicates a better quality of the sample. The high upper critical field in this compound is due to its quasi-1D crystal structure, since the bonding between Rb atoms and the Mo_6As_6 linear chains is very weak. The high upper critical indicates possible unconventional superconductivity in this $\text{Rb}_2\text{Mo}_3\text{As}_3$ compound. High pressure studies of both samples have also been tried to test whether superconducting transition temperatures will be enhanced under higher pressure. However, we did not succeed at this stage. The contact between leads and samples is poor and quickly degraded over time, which may due to the reaction between the high pressure medium Daphne 7373 we used and the samples.

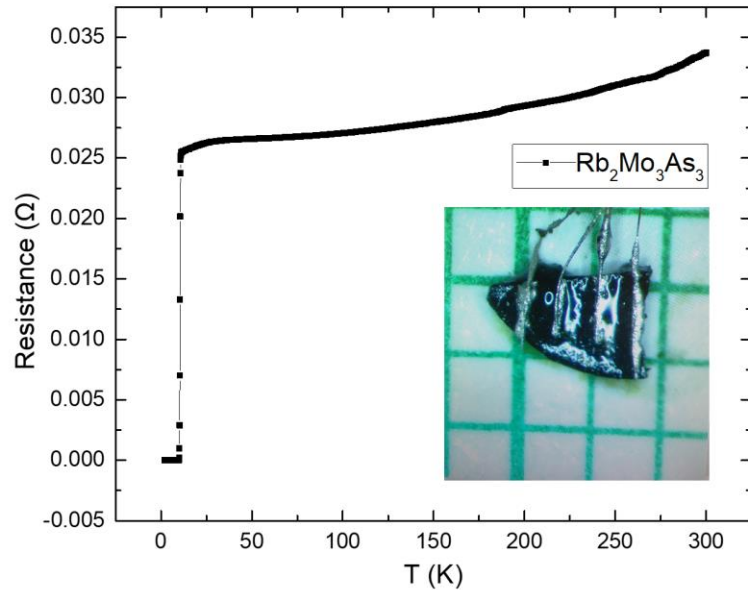


Figure 4.15: The temperature dependence of resistance for $\text{Rb}_2\text{Mo}_3\text{As}_3$ compound, clear superconducting transition can be observed at $T_c \sim 10.6$ K. The inset of Figure shows the four-probe technique for the resistance measurement.

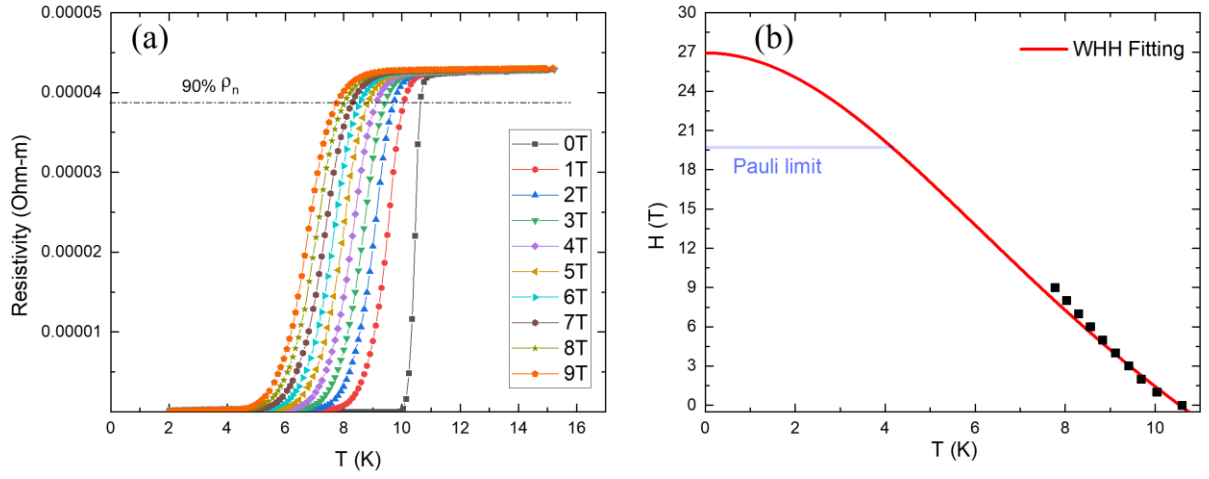


Figure 4.16: (a) The temperature dependence of resistivity at different fields from 0 T to 9 T with 1 T interval. (b) the WHH fitting of the temperature dependence of the critical field with $H_{c2}(T)$ ($90\% \rho_n$), where the straight line shows the Pauli limitation.

CHAPTER 5

SYNTHESIS AND CRYSTAL GROWTH OF QUASI-1D TOPOLOGICAL BI₄X₄ (X=I, BR) MATERIALS

5.1 Introduction

In recent years topological materials have attracted great interest after the discovery of bismuth and antimony chalcogenide (Bi_{1-x}Sb_x) bulk topological insulators (TIs) [58-60]. Topological insulators (TIs) are a class of materials that are electrically insulating in the bulk but host conductive surface states. Most topological insulators are either three-dimensional (3D) strongly bonded bulk materials, or quasi-2D layered vdW materials with only one surface Dirac cone. Despite their richness, fundamental obstacles and limitations exist in exhibiting the decisive properties and realizing the full promise of TIs. Recently, a new family of novel topological insulators with quasi-1D structure, bismuth halides Bi₄X₄ (X = Br, I), was reported to exhibit unique surface properties related to its special quasi-1D structure. They are typical van der Waals materials consisting of 1D chains along the *b*-axis held together by weak non-covalent interactions, the interchain bonding is much weaker than the intrachain bonding strength. Due to the distinct crystallographic structure of the materials, there exist multiple natural cleavage planes (e.g. (001) and (100) surfaces) with distinct surface states. There are different types of α and β phase of Bi₄X₄, which are different from each other in how their 1D chains are stacked. β -Bi₄X₄ was theoretically predicted to be weak topological insulators (WTIs) by C. Liu et. al. [63] and has been experimentally proved [119]. The α -Bi₄Br₄ was also predicted to be a topological insulator with 2D gapless Dirac cone surface states coexisting with 1D hinge states on the side [120-122]. The α phase is the low temperature phase of Bi₄I₄, stable below ~ 300 K, while high temperature β phase

is stable above ~ 300 K, a crystal transition from β -Bi₄I₄ to α -Bi₄I₄ can drive a topological phase transition from a non-trivial WTI to a trivial insulator around room temperature was reported [123]. These reports have attracted tremendous research interest in this quasi-1D topological system in the past few years. Currently, α -, β -Bi₄I₄, and α -Bi₄Br₄ crystals have been successfully grown [124-127], however, β -Bi₄Br₄ crystals still have not been experimentally achieved up to date.

Very recently, high pressure studies on both Bi₄I₄ and Bi₄Br₄ are studied. β -Bi₄I₄ was reported to be superconducting under pressure. Superconductivity was induced in β -Bi₄I₄ under the pressure of 10 GPa with $T_c \sim 4$ K [128]. Later on, α -Bi₄Br₄ was also reported to be superconducting under pressure, two superconducting transition was observed, one at 6.8 K under the pressure of 3.8 GPa, the other at 9 K under the pressure of 5.5 GPa [129]. The so-called topological superconductors have great potential applications in quantum computing and shown to be a potential material candidate for Majorana zero modes [130-132]. But the required high pressure for induced superconductivity in the β -Bi₄I₄ and α -Bi₄Br₄ will prevent further experiment investigation along this direction. Therefore, search for superconductivity in these quasi-1D Bi₄I₄ and Bi₄Br₄ systems under the ambient pressure through chemical doping/intercalation will be quite beneficial for this purpose. As it has been demonstrated in the other quasi-1D systems that superconductivity could also be possibly induced through intercalation of alkali metal, such as Li, Na, K, Rb, into the space between layers that held together by 1D molecular chains [133-139] beside applying high pressure, just like superconductivity has been induced in many of these Transition metal dichalcogenides (TMD) materials through intercalation [140-145]. We anticipate our success for inducing superconductivity in the Bi₄I₄ and Bi₄Br₄ once proper dopants and intercalation routes are identified.

In addition, considering the distinct topological properties and different crystal structures of Bi_4I_4 and Bi_4Br_4 , mixed $\text{Bi}_4\text{I}_{4-x}\text{Br}_x$ crystals will be a great candidate to investigate the possible structural and topological phase transition upon doping with different doping level x . Under such motivations, we have grown single crystals of $\beta\text{-Bi}_4\text{I}_4$, $\alpha\text{-Bi}_4\text{Br}_4$, and mixed $\text{Bi}_4\text{I}_{4-x}\text{Br}_x$ crystals. A hypothetical growth mechanism is proposed for $\alpha\text{-Bi}_4\text{Br}_4$.

5.2 Experimental Procedures

Single crystals of $\beta\text{-Bi}_4\text{I}_4$ and $\alpha\text{-Bi}_4\text{Br}_4$ and mixed $\text{Bi}_4\text{I}_{4-x}\text{Br}_x$ ($x = 0.1, 0.25, 0.4, 0.5, 0.6, 0.75, 1, 1.5, 1.75, 2, 2.5, 3$) were synthesized from chemical vapor transport reaction. The mixtures of Bi pieces (Alfa Aesar, 99.999%) and HgI_2 powders (Alfa Aesar, 99+%) or HgBr_2 powders (Acros Organics, 99+%) were used as starting materials with a stoichiometric ratio, with a total amount of ~ 2 g. Silica quartz tubes with a length of 10 – 15 cm and an inner diameter of 10 mm were used for crystal growth and placed horizontally in a two zones tube furnace. The temperature at the source end was set at 270 °C and 210 °C at the cold end. The reaction typically takes 170 hours, and the tube is heated to 300 °C first to achieve a homogeneous melt of starting materials then cool to 270 °C for the reaction. Black needle shape $\beta\text{-Bi}_4\text{I}_4$ crystals (up to $10 \times 1 \times 0.1 \text{ mm}^3$) are formed on the wall at the colder end of the tube. No $\alpha\text{-Bi}_4\text{Br}_4$ crystals are observed after taking the tube out of the tube furnace, the solid mixture of source materials stays at the hot end. The tube is clean and transparent, indicating there was no chemical transport taking place. Bi_4I_4 tubes were then placed in an oven with uniform temperature at 160 °C for a long-time annealing (2 ~ 10 weeks) to further improve crystal quality. $\alpha\text{-Bi}_4\text{Br}_4$ tubes were also placed in the same oven for long time annealing, single crystal of $\alpha\text{-Bi}_4\text{Br}_4$ then start to form as black needles (up to $6 \times 0.5 \times 0.1 \text{ mm}^3$) on top the solid mixture after few days, and crystal size of $\alpha\text{-Bi}_4\text{Br}_4$ is getting bigger with

increasing of annealing time. Mixed $\text{Bi}_4\text{I}_{4-x}\text{Br}_x$ crystals, similar to $\beta\text{-Bi}_4\text{I}_4$ crystals, formed on the wall at the cold end of the tube. Their crystal size depends on the doping level x , larger crystals (up to $10 \times 1 \times 0.1 \text{ mm}^3$) can be obtained for $x \leq 1$ compounds while smaller crystal (up to $5 \times 0.5 \times 0.1 \text{ mm}^3$) for $x \geq 1$ compounds. $\text{Bi}_4\text{I}_{4-x}\text{Br}_x$ tubes were also placed in the oven at 160°C for a long time annealing to improve crystal quality.

Li intercalation was carried out on both $\beta\text{-Bi}_4\text{I}_4$ and $\alpha\text{-Bi}_4\text{Br}_4$ crystals using organic solvents. Since the Li-intercalated samples are air sensitive, all the intercalation process was performed inside argon filled glovebox with total O_2 and H_2O levels $< 0.1\text{ppm}$. The n-butyl-lithium (n-BuLi) used was 2.6 M ($1\text{M} = 1 \text{ mol l}^{-1}$) concentration in hexane solution from Alfa Aesar and diluted to 0.25 M. The organic solvent hexane was vacuum distilled and dried with molecular sieve before usage. Li intercalated $\beta\text{-Bi}_4\text{I}_4$ and $\alpha\text{-Bi}_4\text{Br}_4$ samples were prepared by soaking the parent Bi_4I_4 and $\alpha\text{-Bi}_4\text{Br}_4$ in diluted 0.25 M n-BuLi solution for 17 hours. The samples were dried and placed into a gelatin capsule inside the glovebox for the magnetic measurement.

5.3 Results and discussion

The crystal structure of $\alpha\text{-}$, $\beta\text{-Bi}_4\text{I}_4$ and $\alpha\text{-Bi}_4\text{Br}_4$ are shown in Figure 5.1. They all adopt quasi-1D structure along b-axis crystallizing in a monoclinic space group $C12/m1$ (12), with $a = 14.245(3) \text{ \AA}$, $b = 4.428(1) \text{ \AA}$, $c = 19.968(4) \text{ \AA}$ and $\beta = 92.96(2)^\circ$ for $\alpha\text{-Bi}_4\text{I}_4$; $a = 14.386(3) \text{ \AA}$, $b = 4.430(1) \text{ \AA}$, $c = 10.493(3) \text{ \AA}$ and $\beta = 107.87(2)^\circ$ for $\beta\text{-Bi}_4\text{I}_4$; $a = 13.064(5) \text{ \AA}$, $b = 4.338(2) \text{ \AA}$, $c = 20.061(8) \text{ \AA}$ and $\beta = 107.42(3)^\circ$ for $\alpha\text{-Bi}_4\text{Br}_4$. The difference among the crystal structure of these compounds is how their 1D molecule chain stacking. $\alpha\text{-}$ and $\beta\text{-Bi}_4\text{I}_4$ are consisted of packing of a normal single layer, in contrast to the combined packing of normal and mirror-reflected single layer along the c-axis in $\alpha\text{-Bi}_4\text{Br}_4$.

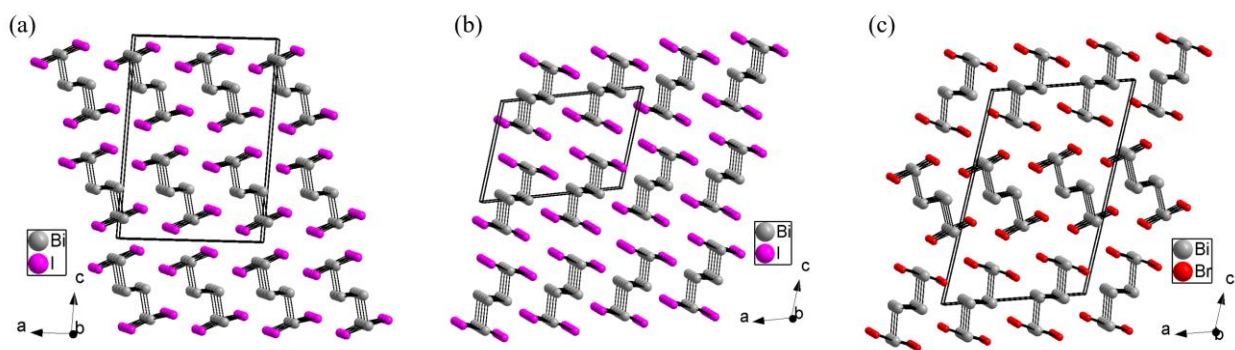


Figure 5.1: Crystal structure of (a) α - Bi_4I_4 , (b) β - Bi_4I_4 and (c) α - Bi_4Br_4 , both are composed of 1D molecular chains long b-axis held together by weaker non-covalent interactions. α -, β - Bi_4I_4 are consist of packing of normal single layer, while combined packing of normal and mirror-reflected single layer along c-axis in α - Bi_4Br_4 .

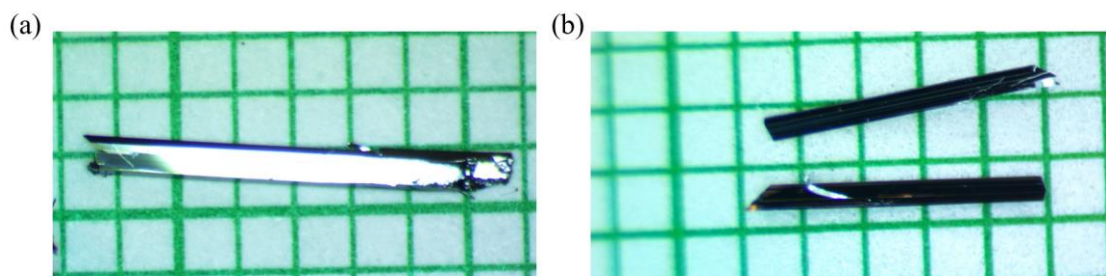


Figure 5.2: Photos of typical size (a) β - Bi_4I_4 and (b) α - Bi_4Br_4 crystals

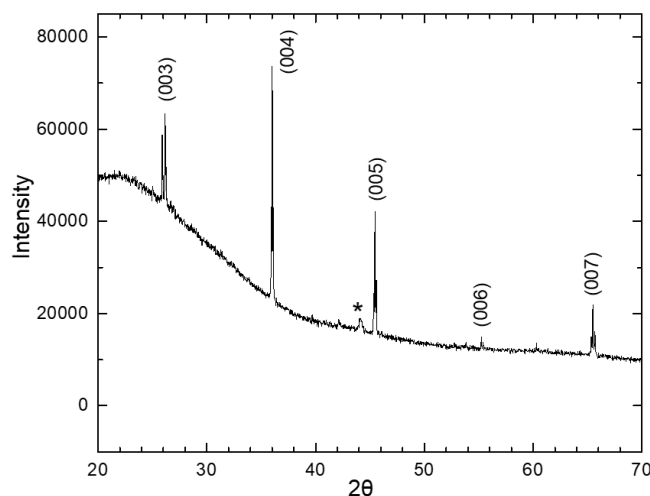


Figure 5.3: XRD pattern of obtained β - Bi_4I_4 crystal. The main diffraction peaks can be indexed as the (00 l) preferred orientation of β - Bi_4I_4

Due to the phase transition from β phase to α phase of Bi_4I_4 around 300 K, the Bi_4I_4 crystals we have at room temperature is the $\beta\text{-Bi}_4\text{I}_4$, which will transform to $\alpha\text{-Bi}_4\text{I}_4$ upon cooling when performing the low temperature transport measurement. The obtained $\beta\text{-Bi}_4\text{I}_4$ and $\alpha\text{-Bi}_4\text{Br}_4$ crystals are shown in Figure 5.2. The longest dimension corresponds to its b-axis which is the orientation of the 1D molecule chains in the crystal structure and cleavage planes can be clearly observed along that direction. XRD peaks collected from 20° to 80° of the obtained $\beta\text{-Bi}_4\text{I}_4$ crystal is presented in Figure 5.3, the main XRD peaks can be indexed as the $(00l)$ preferred orientation of $\beta\text{-Bi}_4\text{I}_4$, suggesting that the obtained crystal is indeed $\beta\text{-Bi}_4\text{I}_4$. An unidentified peak (*) at $\sim 44^\circ$ was also observed, and the extra peaks close to each $(00l)$ peaks of $\beta\text{-Bi}_4\text{I}_4$ are indexed as the $(00l)$ preferred orientation of $\alpha\text{-Bi}_4\text{I}_4$.

The observation that Bi_4I_4 crystals formed at the colder end of the tube proves that chemical vapor transport should be the growth mechanism for $\beta\text{-Bi}_4\text{I}_4$. By contrast, $\alpha\text{-Bi}_4\text{Br}_4$ crystals do not form under temperature gradient by placing the source materials in a tube furnace. The mixture of source materials (Bi metal and HgBr_2 powder) melt at 300°C and remain as liquid at 270°C , quickly solidified upon cooling. $\alpha\text{-Bi}_4\text{Br}_4$ crystals form on top of the solid mixture when placing the tube in an oven (almost uniform temperature) at 160°C . This observation indicates chemical vapor transport may not be the growth mechanism for $\alpha\text{-Bi}_4\text{Br}_4$ since the temperature gradient is not necessary for the growth of $\alpha\text{-Bi}_4\text{Br}_4$ crystals. Actually, such growth mechanism is very similar to the growth mechanism we proposed for 2D material black phosphorus in the latter chapter, the vapor - solid - solid (VSS) like growth mechanism. VSS mechanism is a primary growth mode for nanowires and nanotubes, where the vapor acts as the precursor of the final product (solid), and the catalyst is solid. The solid catalyst is either an alloy or a compound consisting of foreign and

final product elements. In this growth mechanism, the source materials Bi and HgBr₂ react at 270 °C and form a solid compound that acts as a catalyst. HgBr₂ or Br vapor slowly reacting with the solid catalyst forming α -Bi₄Br₄ crystals through some catalytic effect. However, this is only a speculation based on the evidence that all as-grown α -Bi₄Br₄ needles attach on the solid compound, and the chemical formula and exact catalytic mechanism is still elusive at this stage. Solid experimental evidences for this hypothetical growth model are needed in future work.

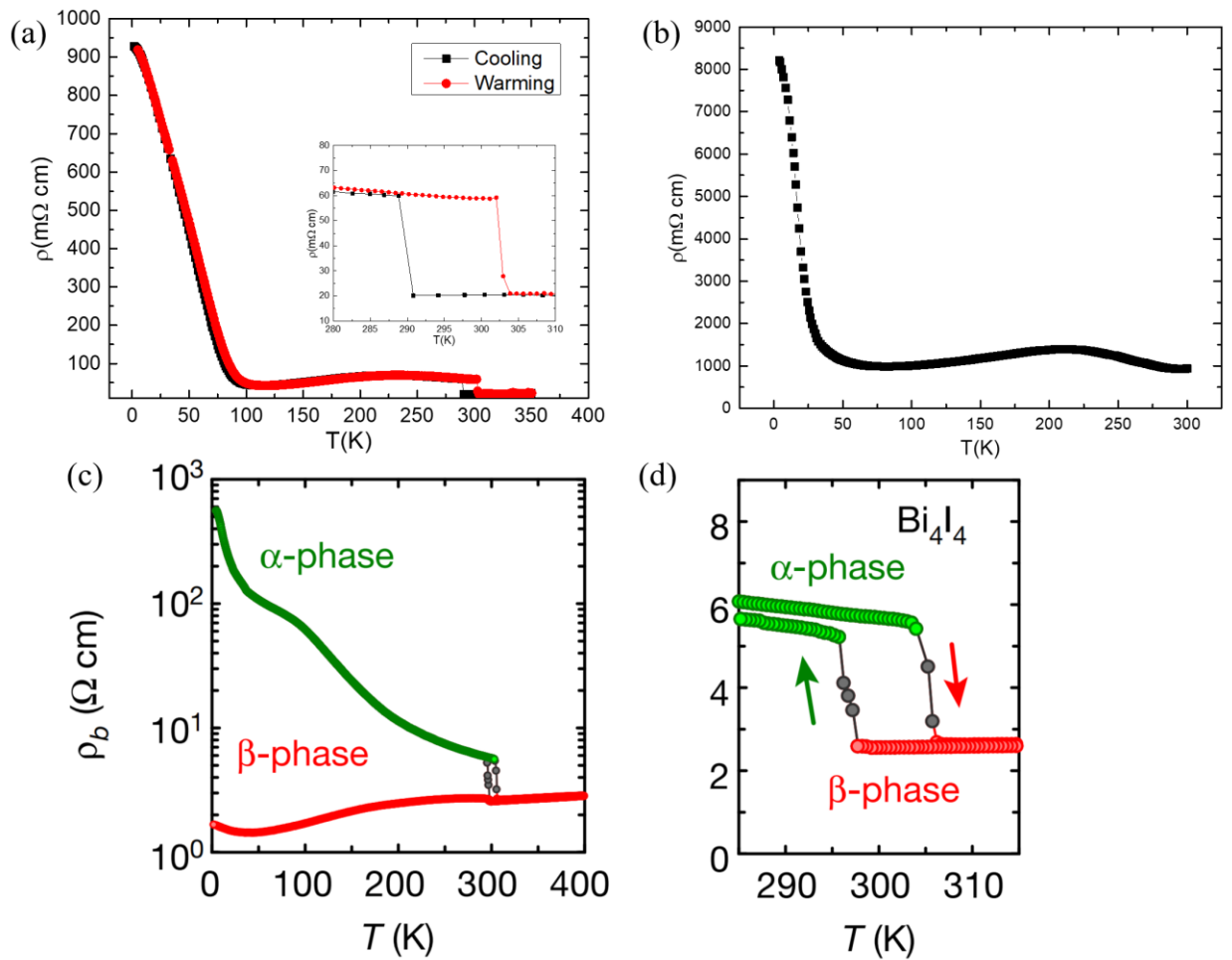


Figure 5.4: Temperature dependence of the electrical resistivity for (a) Bi₄I₄ and (b) α -Bi₄Br₄ crystals along the chain direction. A hysteresis was observed around 300 K for Bi₄I₄, showing the phase transition between α -Bi₄I₄ and β -Bi₄I₄. (c) temperature dependence of the electrical resistivity for Bi₄I₄ from [123]. (d) the hysteresis around 300 K from [123].

The temperature dependence of electrical resistivity for β -Bi₄I₄ and α -Bi₄Br₄ crystals along the chain direction is shown in Figure 5.4. A semiconducting property is observed in the overall behavior of both crystals. Three different regimes can be identified: for temperature above 250 K (220 K), Bi₄I₄ (α -Bi₄Br₄) displays semiconducting behavior, while at lower temperature $\rho(T)$ starts decreasing smoothly down to 100 K (50 K), then followed by a sharp insulating transition, which could be caused by a charge density wave (CDW) transition. In fact, the quasi-1D structure of these compounds would facilitate the appearance of such ordered state. Interestingly, a resistivity hysteresis loop was observed around 300 K for β -Bi₄I₄ crystal, revealing the phase transition between α -Bi₄I₄ and β -Bi₄I₄, consistent with [123], where are two independent reports simultaneously on this phase transition, as shown in reproduced Figure from [123] in Figure 5.4 (c) and (d).

Chemical composition of mixed Bi₄I_{4-x}Br_x crystals were examined by EDAX, using β -Bi₄I₄ and α -Bi₄Br₄ as internal standard, with the average atomic percentage of Bi (48.64%), I (51.36%) for β -Bi₄I₄, and Bi (48.33%), Br (51.67%) for α -Bi₄Br₄. We found out that all three elements are uniformly distributed throughout the samples, and no other binary or elemental phases are observed. The average composition of elements was obtained by taking the average of measurements from three different surface areas, with the distance of each point at $\sim 50 \mu\text{m}$. The results are listed in Table 5.1, we can clearly see the Br doped to the Bi₄I₄ system, even at the lowest doping level $x = 0.1$. The measured Br composition increases with increasing of doping level and is found in general exhibiting $\sim 30\%$ deviation from nominal doping level x . Figure 5.5 (a) shows a typical size Bi₄I₃Br crystal, which has a similar size compare to Bi₄I₄ crystal, and (b) is the EDAX analysis spectrum for the representative Bi₄I₃Br crystal.

Table 5.1: Normalized formula for mixed $\text{Bi}_4\text{I}_{4-x}\text{Br}_x$ crystals obtained from EDAX. $\beta\text{-Bi}_4\text{I}_4$ and $\alpha\text{-Bi}_4\text{Br}_4$ crystals were used as internal standard

$\text{Bi}_4\text{I}_{4-x}\text{Br}_x$	Bi atomic %	I atomic %	Br atomic %	Normalized
Samples	average	average	average	formula
x = 0.10	48.26	50.61	1.13	$\text{Bi}_4\text{I}_{3.91\pm0.17}\text{Br}_{0.08\pm0.01}$
x = 0.25	52.08	46.20	1.72	$\text{Bi}_4\text{I}_{3.63\pm0.01}\text{Br}_{0.15\pm0.02}$
x = 0.40	47.38	49.67	2.95	$\text{Bi}_4\text{I}_{3.78\pm0.03}\text{Br}_{0.21\pm0.01}$
x = 0.50	48.21	46.09	5.70	$\text{Bi}_4\text{I}_{3.56\pm0.14}\text{Br}_{0.44\pm0.07}$
x = 0.60	50.56	45.49	3.95	$\text{Bi}_4\text{I}_{3.68\pm0.16}\text{Br}_{0.32\pm0.02}$
x = 0.75	50.95	43.31	5.74	$\text{Bi}_4\text{I}_{3.53\pm0.09}\text{Br}_{0.47\pm0.03}$
x = 1.00	48.79	40.96	10.25	$\text{Bi}_4\text{I}_{3.21\pm0.03}\text{Br}_{0.78\pm0.01}$
x = 1.50	54.18	31.59	14.23	$\text{Bi}_4\text{I}_{2.72\pm0.07}\text{Br}_{1.27\pm0.01}$
x = 1.75	54.70	27.02	18.28	$\text{Bi}_4\text{I}_{2.46\pm0.01}\text{Br}_{1.53\pm0.06}$
x = 2.00	50.41	20.78	28.80	$\text{Bi}_4\text{I}_{1.68\pm0.03}\text{Br}_{2.32\pm0.04}$
x = 2.50	47.90	16.72	35.37	$\text{Bi}_4\text{I}_{1.29\pm0.03}\text{Br}_{2.71\pm0.04}$
x = 3.00	48.58	9.46	41.96	$\text{Bi}_4\text{I}_{0.74\pm0.04}\text{Br}_{3.26\pm0.08}$

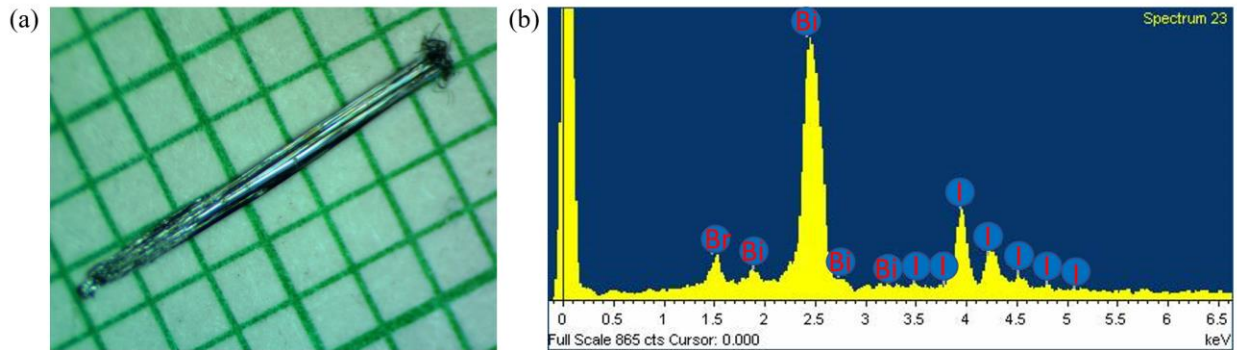


Figure 5.5: (a) Photo of typical size $\text{Bi}_4\text{I}_3\text{Br}$ crystal (b) EDAX spectrum for $\text{Bi}_4\text{I}_3\text{Br}$ crystal

The temperature dependent of electrical resistivity for $\text{Bi}_4\text{I}_{3.9}\text{Br}_{0.1}$ crystal is shown in Figure 5.6. We can clearly see a phase transition around 320 K, compared to α to β phase transition around 300 K in Bi_4I_4 . More crystals with different Br doping levels will be examined in the future to explore the topological phase transition in this system.

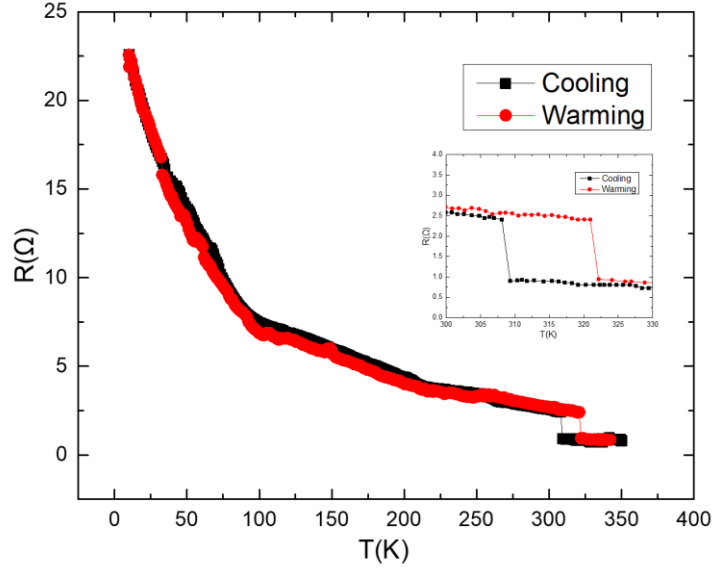


Figure 5.6: Temperature dependence of the electrical resistivity for $\text{Bi}_4\text{I}_{3.9}\text{Br}_{0.1}$ crystal. A hysteresis was observed around 320 K.

Possible superconductivity was observed in both Li intercalated β - Bi_4I_4 and α - Bi_4Br_4 crystals with T_c of ~ 2.45 K and ~ 2.5 K, respectively. The temperature dependence of the magnetic susceptibility was measured from 2 K to 3 K with ZFC and FC modes under a stable magnetic field of 10 Oe as shown in Figure 5.7. However, the superconducting volume fraction is very small on both compounds, which may due to the unoptimized intercalation method such as short soaking time or non-optimal concentration of organic solvent. Further intercalation studies with optimized methods need to be developed to achieve a larger volume fraction or higher superconducting transition temperature.

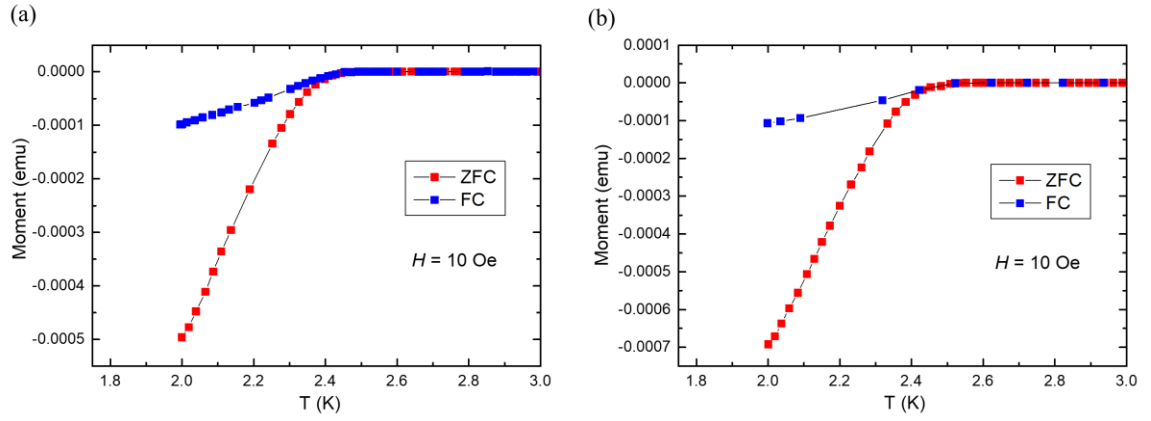


Figure 5.7: temperature dependence of dc magnetization from 2 K to 3 K for Li intercalated (a) Bi_4I_4 and (b) $\alpha\text{-Bi}_4\text{Br}_4$ crystals. A clear superconducting transition can be observed at 2.45 K and 2.5 K for Bi_4I_4 and $\alpha\text{-Bi}_4\text{Br}_4$, respectively.

CHAPTER 6

MECHANISM AND FILM GROWTH FOR 2D MATERIAL BLACK PHOSPHORUS²

6.1 Introduction

In the past decade, two-dimensional (2D) materials have burgeoned to be one of the most extensively studied class of nanomaterials [146,147]. The atomically thin nature leads to some exceptional and fascinating properties that their bulk counterparts do not possess. Graphene, the first 2D material, continues to be the most widely studied material since its emergence in 2004 [148-150]. However, although graphene possesses unique electrical, optical, and physical properties, the absence of a bandgap severely limits its application to the semiconductor industry. Hence, much effort has been devoted to the search of alternative 2D semiconductor which also adopt layered structure like graphite, such as transition metal dichalcogenides (TMDs) [151-154] and Black phosphorus (Black-P) [155-160].

Black-P and its monolayer counterpart, phosphorene, emerge as a promising candidate for two-dimensional (2D) materials owing to their comprehensive outstanding properties, especially the range of their band gaps and potentially high carrier mobilities. Therefore, they attract tremendous immediate interests from condensed matter physicists, chemists, semiconductor device engineers, and material scientists. Black-P was first synthesized in 1914 by Bridgman [161] and it is the most stable allotrope of phosphorus (P) with a puckered layer structure. The monolayer Black-P includes two atomic layers with two different kinds of P-P bonding patterns. The top view of

² Adapted with permission from S. Li, X. Liu, X. Fan, Y. Ni, J. Miracle, N. Theodoropoulou, J. Sun, S. Chen, B. Lv, and Q. Yu, *Cryst. Growth Des.* 17, 12, 6579-6585 (2017). Copyright 2020 American Chemical Society.

Black-P along the z -direction shows a hexagonal structure with bond angles of 96.3° and 102.1° , as shown in Figure 6.1.

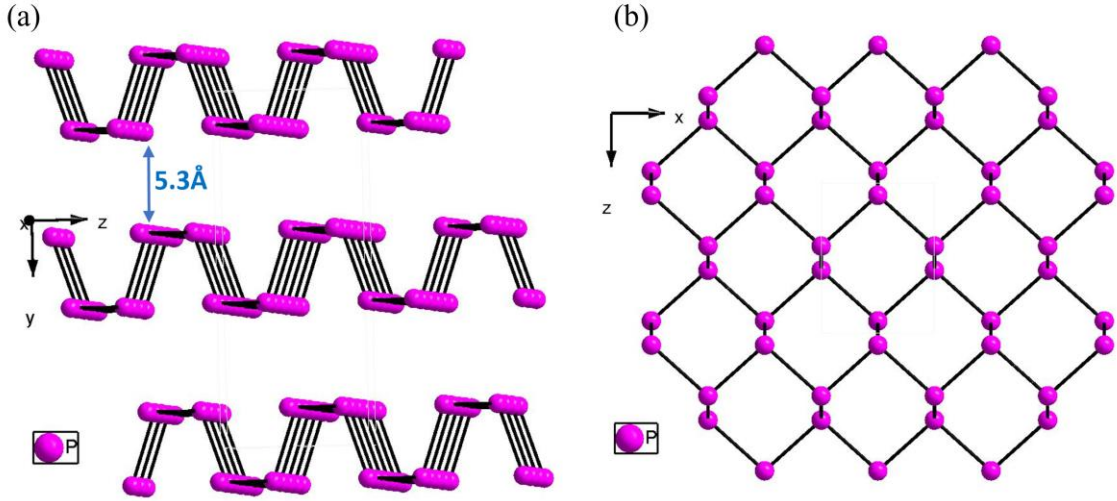


Figure 6.1: Crystal structure of Black-P. (a) Side view of the Black-P crystal lattice. The interlayer spacing is 5.3 Å. (b) Top view of the lattice of single-layer Black-P. x and z correspond to the zigzag and armchair directions of Black-P.

Recent theoretical studies have predicted that monolayer Black-P (phosphorene) can have an extremely high hole mobility ($10000 \text{ cm}^2\text{V}^{-1}\text{s}^{-1}$) [162]. Depending on the thickness, the band gap of Black-P can cover $\sim 0.3 - 2.0 \text{ eV}$, which bridges the zero band gap of graphene and the relatively large band gap ($\sim 1.5 - 2.5 \text{ eV}$) of many TMDs. The band gap of Black-P covers the near- and mid-infrared spectrum, thus making it an appealing candidate for near- and mid-infrared optoelectronics [163,164]. Moreover, the mobility/on-off ratio combination for Black-P falls into a region that could not be easily covered by graphene or TMDs. Figure 6.2 (Figure reproduced from Ref. [155]) represents the mobility/on-off ratio spectrum of nanomaterials with correspond performance regions indicated for Graphene, Black-P and TMDs.

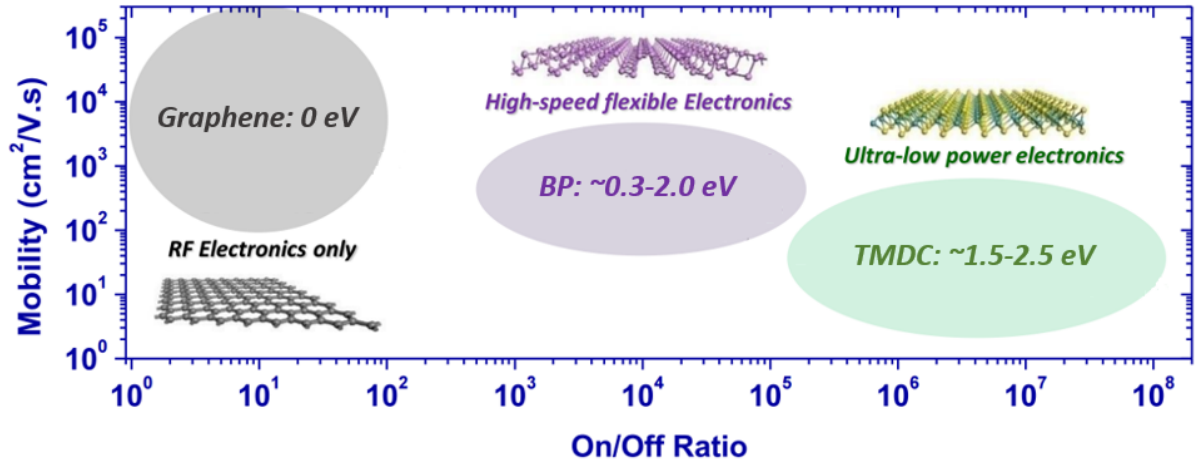


Figure 6.2: The mobility/on-off ratio spectrum of nanomaterials with corresponding performance regions indicated for Graphene, Black-P and TMDs. The shaded regions are the approximate possible ranges of performance reported for the respective materials in the literature. (Figure reproduced from Ref. [155]).

In 1914, Bridgman first converted white phosphorus (White-P) to Black-P at 200 °C and ~ 1.2 GPa. This high-pressure synthesis method was a common technique to obtain Black-P in the following 40 years. Afterward, Bridgman also converted red phosphorus (Red-P) to Black-P at room temperature at 4.5 GPa / 8 GPa with/without shear stress [165,166]. In the 1960s, Black-P was reported to be prepared from a solution of White-P in Mercury or Bismuth-flux [167,168]. Since readily stable Red-P does not dissolve in the flux, and the lack of high purity White-P due to its chemical activity, some sophisticated chemical treatment and apparatus are normally adopted for the synthesis, yet still yield deformed crystals, not to mention the potential high cost and high toxicity associated with the flux. In 2007, Black-P was reported to be synthesized at a lower pressure and a much cleaner controlled atmosphere without the use of toxic catalysts or “dirty” flux through mineralizer-assisted vapor transport reaction [169,170]. The mineralization additive reported initially was Au / Sn / SnI₄ [169], and then simplified to Sn / SnI₄ [171]. Because the

reaction temperature ($\sim 600\text{ }^{\circ}\text{C}$) is much higher than the sublimation temperature of SnI_4 ($\sim 200\text{ }^{\circ}\text{C}$), it is further simplified to use Sn / I_2 to grow Black-P ribbons with a box furnace (with less temperature gradient and large reaction space) [172]. Zhao et al. further extended their studies to investigate the growth mechanism and proposed some speculated growth models based on their results [172].

However, many questions regarding to Black-P crystal growth remain. For example, what is the exact role of these mineralization additives to promote the formation of Black-P and their specific mechanism at different temperature stages? What exactly is the formation temperature range and growth model for Black-P? Is it a slow growing process from the highest temperature ($> 600\text{ }^{\circ}\text{C}$) down to the lowest temperature ($\sim 200\text{ }^{\circ}\text{C}$), similar to the crystallization and crystal growth in the flux? Or it is a rather rapid process that occurs at a much narrower temperature range? Different precursors such as Sn , I_2 , SnI_2 , SnI_4 , and Au have been used in the past as necessary chemicals assisting the growth of Black-P. However, the exact functions of these chemicals are not well understood yet. At the reported highest temperature ($\sim 600\text{ }^{\circ}\text{C}$), the most thermodynamically stable species is the SnI_2 . Therefore, those additives such as Sn , I_2 , or SnI_4 will probably either react with each other or decompose to form SnI_2 (g): $\text{Sn} + \text{I}_2 \rightarrow \text{SnI}_2$; $\text{SnI}_4 \rightarrow \text{SnI}_2 + \text{I}_2$. The gaseous SnI_2 will react with P_4 vapor (sublimed from Red-P) upon cooling, which assists the formation of Black-P. Previous studies have ambiguously speculated that some gaseous ternary P-Sn-I compound formed before the formation of Black-P ribbons is crucial for the nucleation and continuous growth of the Black-P crystals. However, the exact composition of the solid-state material prior to the formation of Black-P, and its role to promote the reaction remain unknown.

6.2. Experimental results and discussion

We have carried out a series of control experiments to answer the unsolved problems with regards to Black-P growth and to understand the Black-P growth mechanism.

6.2.1 Necessity of the chemicals

From the previous works [169-172], different precursors such as Sn, I₂, SnI₂, SnI₄ have been used as necessary chemicals assisting the growth of Black-P. However, the exact functions of these chemicals are not well understood yet. We grew Black-P crystals through the elemental Red-P, Sn, I₂, SnI₂, and SnI₄ to investigate which chemicals are necessary for a successful growth of Black-P. At the reported highest temperature (~ 600 °C), the most thermodynamically stable species is the SnI₂. Therefore, those additives such as Sn, I₂, or SnI₄ will probably either react with each other or decompose to form SnI₂(g): $\text{Sn} + \text{I}_2 \rightarrow \text{SnI}_2$; $\text{SnI}_4 \rightarrow \text{SnI}_2 + \text{I}_2$. There are three possible chemicals combination at the highest temperature which was set to 600 °C: (1) SnI₂ (2) SnI₂ + I₂ (3) Sn + SnI₂, correspond to the ratios of the precursors (1) Sn : I₂ = 1 (2) Sn : I₂ < 1 (3) Sn : I₂ > 1 respectively. Therefore, Different Sn : I₂ ratios with the same amounts of Red-P were tested to grow Black-P. Two control experiments were carried out, one used SnI₂ and the other used SnI₄ as precursor. The results are listed in Table 6.1. None of these two experiments we observed Black-P formed. Since solely chemicals SnI₂ or SnI₄ does not work. The first two possible chemicals: (1) SnI₂ and (2) SnI₂ + I₂ should not be the necessary chemical for the growth. Therefore, (3) Sn + SnI₂ turns out to be the necessary chemicals at the highest temperature for a successful growth of Black-P. Sn : I₂ > 1 indicates that excess Sn besides the formation of SnI₂ is the crucial ingredient for Black-P growth.

Table 6.1: Control experiments for the investigation of the necessity of chemicals.

Reactants	Max. T (°C)	Possible species at 600 °C	Black-P formation
Red-P + SnI ₂	600	P ₄ , SnI ₂	No
Red-P + SnI ₄	600	P ₄ , SnI ₂ , I ₂	No

It is reasonable to speculate a chemical vapor transport mechanism since I₂ is used as a precursor. For a typical chemical vapor transport reaction, a solid is volatilized in the presence of a gaseous reactant (transport agent) and deposited elsewhere in the form of crystals. The temperature gradient plays an important role in such reaction. Several samples with different combinations of chemicals as precursors were prepared and both tube furnace which provides a temperature gradient (> 50 °C) along the length of the heated zones and box furnace which provides almost uniform temperature region were used. The results are listed in Table 6.2. It shows that the excess of Sn beside the formation of SnI₂ indeed plays an important role for a successful growth. Sn : I₂ > 2 : 1 atomic ratio was found out to work the best. We also found the temperature gradient is not necessary for a successful growth of Black-P crystals, in other words, the chemical vapor transport should not be the growth mechanism for Black-P since temperature gradient is not crucial. At the highest temperature 600 °C, the excess of Sn could only be in the liquid phase since the melting point of Sn is ~ 232 °C, that lead us to speculate a Vapor – Liquid – Solid (VLS) mechanism [173-178], which is a mechanism for the growth of one-dimensional (1D) structures, such as nanowires, from chemical vapor deposition. A characteristic feature of the VLS route for nanowire synthesis is the presence of a catalyst particle, usually a droplet, that mediates the mass transfer from the

vapor phase precursor to the growing nanowire. However, we carefully inspected the quartz tubes at 600 °C, no liquid Sn were found. Therefore, the VLS mechanism should also be eliminated.

Table 6.2: Control experiments for further investigation of the necessity of chemicals

Reactants	Max. T (°C)	Possible species at 600 °C	Black-P formation using tube furnace	Black-P formation using box furnace
Red-P + Au + Sn + SnI ₄	600	P ₄ , Sn, I ₂ , AuI, Sn(l)	Yes	Yes
Red-P + Sn + SnI ₂	600	P ₄ , SnI ₂ , Sn(l)	Yes	Yes
Red-P + Sn + I ₂ (Sn : I ₂ > 1 : 1)	600	P ₄ , SnI ₂ , Sn(l)	Yes	Yes
Red-P + Sn + I ₂ (Sn : I ₂ = 1 : 1)	600	P ₄ , SnI ₂	No	No
Red-P + Sn + I ₂ (Sn : I ₂ < 1 : 1)	600	P ₄ , SnI ₂ , I ₂	No	No

6.2.2 Formation temperature range for Black-P

The next question we want to understand is what is the formation temperature range for Black-P. Based on our aforementioned findings, we prepared several samples with a fixed ratio of precursors Red-P : Sn : I₂ = 100 : 2 : 1. These samples all followed the same temperature profile and quenched directly into cold water upon cooling at the different temperature. The results are listed in Table 6.3. Between 600 °C - 520 °C, we did not observe Black-P formed, but some solid Sn-P-I ternary phase formed between this temperature range. Below 520 °C, Black-P started to

form and completed at 420 °C with the evidence of that at 420 °C and 350 °C, the shape and morphology of the Black-P crystals are nearly identical, and the quartz tubes are clean and transparent. These results show that the formation temperature range of Black-P is between 520 °C to 420 °C upon cooling.

Table 6.3: Control experiments for the formation of Black-P at different quenching temperature

Quenching temperature (°C)	600	550	520	500	480	420	350
Black-P formation	No	No	No	Yes	Yes	Yes	Yes

The reported highest temperature of previous works from other groups that successfully grow Black-P crystals is 600 °C [169-172]. Since the Black-P formation temperature range is between 520 °C to 420 °C, then 520 °C should be sufficient as the highest temperature. If the highest temperature can be lowered from 600 °C to 520 °C, which will bring many benefits to the commercial production of Black-P, since lower temperature is easier to access and manipulate, also from the ideal gas law, the vapor pressure of P₄ that sublimated from Red-P at the highest temperature is proportional to the temperature inside the quartz tube. Lower temperature can ensure lower vapor pressure inside the quartz tube and provide a much safer synthesis environment. To verify it, several samples with a fixed ratio of Red-P : Sn : I₂ = 100 : 2 : 1 were prepared, and followed the same temperature profile but with the different highest temperature: 650 °C, 620 °C, 600 °C, and 520 °C. The results are listed in Table 6.4.

It shows that 600 °C is the minimum temperature required for the growth of Black-P, 520 °C is not enough for the growth. The cooling process from the highest temperature 600 °C to 520 °C is an essential step for Black-P growth although Black-P starts to form at 520 °C. This result is consistent with the reported highest temperature from the previous literature.

Table 6.4: Control experiments for required synthetic temperature

Max. T (°C)	Black-P formation
650	Yes
620	Yes
600	Yes
520	No

6.2.3 Hypothesis for growth mechanism for Black-P

A solid ternary Sn-P-I compound formed upon cooling from the highest temperature 600 °C to 520 °C, just before the formation of Black-P crystals. It remains as solid during the formation of Black-P. Consider the cooling process from the highest temperature 600 °C to 520 °C is an essential step for Black-P growth, Therefore, the Sn-P-I ternary compound should play an important role in the formation of Black-P. From the previous literature [179-183], $\text{Sn}_{24}\text{P}_{22-x}\text{I}_8$ turns out to be the sole ternary phase of Sn-P-I compound and it remains as a solid below 550 °C and decomposes irreversibly to Red-P, SnI_2 , and Sn above 620 °C. The $\text{Sn}_{24}\text{P}_{22-x}\text{I}_8$ belongs to a well-known type-I clathrate structure [181,183], with a 3D inversed network composed by Sn and P atoms as host framework, and I as guest atoms. The crystal structure of $\text{Sn}_{24}\text{P}_{22-x}\text{I}_8$ is shown in Figure 6.3. The compound crystallizes in the cubic structure with space group $\text{Pm}\bar{3}\text{n}$ (#233), with five different atomic Wyckoff positions. It has vacancies within the host framework, as stressed by the formulation $\text{Sn}_{24}\text{P}_{19.3\square 2.7}\text{I}_8$, where \square denotes a vacancy. Previous single crystal studies [180] have shown that the P vacancy in this material could be as high as 13% ($x \sim 2.7$). Sn atoms at the 24k

position, and P1 atoms at the 16i position, together form two pentagonal dodecahedra. Other P2 atoms, forming the hexagonal faces of the 6 tetrakaidecahedrons, partially occupy the 6c atomic positions ($1/4, 0, 1/2$), which causes the vacancy structures in the framework. Two of the 8 iodide atoms are located at the center of the 2 pentagonal dodecahedrons (I1 in the 2a position) and the 6 others at the center of the 6 slightly larger tetrakaidecahedrons (I2 at the 6d position). Previous lattice dynamics analysis has indicated that the host-guest interaction in this inverse-clathrate compound is weak and that the dynamics of the guest atoms can be treated independently of that of the host framework.

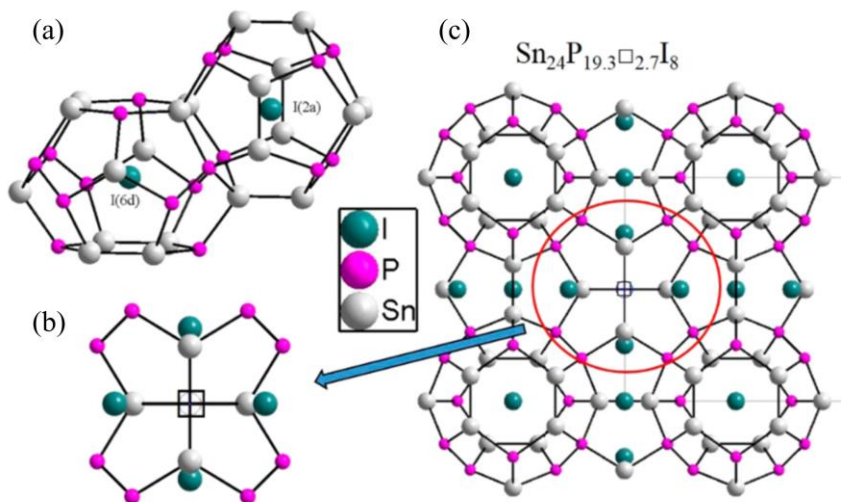


Figure 6.3: Crystal structure of $\text{Sn}_{24}\text{P}_{22-x}\text{I}_8$. (a) Pentagonal dodecahedra and tetrakaidekahedron framework formed by Sn and P atoms in the clathrate $\text{Sn}_{24}\text{P}_{22-x}\text{I}_8$, where two different types of I atoms (2a and 6d) are located at the centers of each polyhedron. (b, c) The crystal structure of $\text{Sn}_{24}\text{P}_{22-x}\text{I}_8$, where the vacancy \square caused by partially occupied P2 atom is highlighted.

The unique structure vacancies at the P sites in the framework of $\text{Sn}_{24}\text{P}_{19.3}\square_{2.7}\text{I}_8$ might hold the glue for its catalytic effect to grow Black-P crystals through the direct interaction of phosphorus vapor with this solid ternary precursor. This is likely to be another popular vapor-phase mechanism, the Vapor – Solid – Solid (VSS) mechanism [173-178], similar to VLS

mechanism, is also a primary growth mode for nanowires and nanotubes, where the vapor is the precursor of the final product (solid), and the catalyst is solid. The solid catalyst is either an alloy or a compound consisting of foreign and final product elements.

On the basis of our aforementioned findings, three hypothetical growth models for the Black-P crystal growth were proposed, as shown in Figure 6.4:

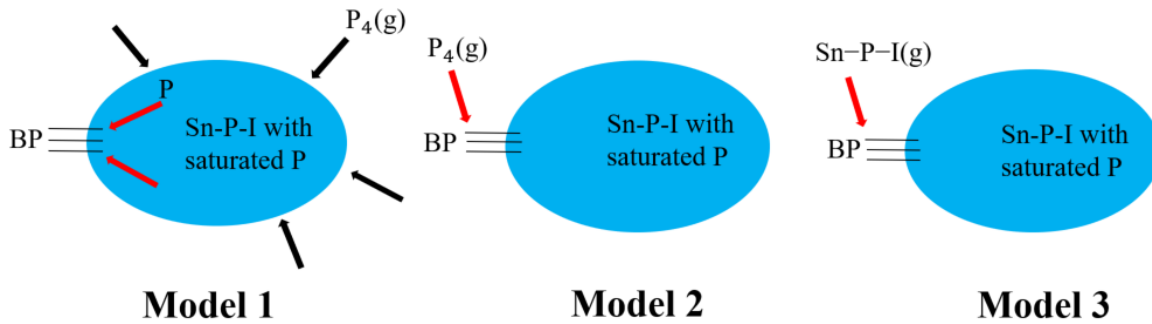


Figure 6.4: Hypothesis for three different growth models for Black-P crystal growth.

(1) In model 1, Sn-P-I ternary compound works not only as the nucleation center but also as a catalyst, the gaseous $P_4(g)$ which is the vapor phase of solid Red-P: $\text{Red-P (s)} \xrightarrow{\text{evaporation}} P_4(g)$, work as vapor precursor. P_4 vapor diffuses into Sn-P-I ternary compound, when the P concentration is high enough, it segregates on the surface of Sn-P-I ternary compound to form Black-P crystal.

(2) In model 2, the Sn-P-I ternary compound only works as a nucleation center, and it has no catalytic effect on the formation of Black-P, $P_4(g)$ work as vapor precursor. One Black-P crystal is formed, the P_4 vapor will continue to deposit to the free end of those formed Black-P edge to grow bigger size crystals. In this model, the role of Sn-P-I ternary compound will be minimal once the Black-P crystals start to form.

(3) In model 3, the Sn-P-I ternary compound only works as a nucleation center, the difference between model 2 is instead of vapor P_4 (g) precursor, the vapor Sn-P-I phase now works as a precursor. The vapor Sn-P-I phase decomposes at the free end of Black-P to provide P atom and SnI_2 (g). SnI_2 (g) will be recycled for continuous reaction: SnI_2 (g) + P_4 (g) + Sn (g) \rightarrow Sn-P-I (g), $Sn-P-I$ (g) + Black-P (s) \rightarrow Sn (g) + SnI_2 (g) + Black-P (s).

6.2.4 Experimental verification of hypothesis for growth mechanism for Black-P

Several control experiments were performed to verify the three different hypothetical growth models. The results are listed in Table 6.5. Red-P and Black-P seed crystals on the $Sn_{24}P_{22-x}I_8$ ternary compound at 600 °C or 520 °C were tested, but no Black-P crystals formed, which eliminate the model 2 and confirm that the $Sn_{24}P_{22-x}I_8$ ternary phase has to be involved in the formation of Black-P. Below 550 °C, the $Sn_{24}P_{22-x}I_8$ ternary phase should remain as solid, and decompose irreversibly to Red-P, SnI_2 , and Sn above 620 °C. During the Black-P formation temperature range: 520 °C - 420 °C, the $Sn_{24}P_{22-x}I_8$ ternary phase should remain as solid phase, so there is no vapor $Sn_{24}P_{22-x}I_8$ ternary phase would exist. Model 3 should also be excluded. Therefore, the model 1 turns out to be the mechanism for the Black-P growth.

To verify it, we synthesized the $Sn_{24}P_{22-x}I_8$ ternary compound directly from Red-P, SnI_4 , and Sn at 550 °C for 5 days. The XRD pattern of our synthesized $Sn_{24}P_{22-x}I_8$ ternary compound shows the high purity of the sample. The scanning electron microscopy (SEM) and energy-dispersive X-ray spectroscopy (EDX) analysis are also consistent with the previous studies from other groups. The synthesized $Sn_{24}P_{22-x}I_8$ ternary compound was then used to grow Black-P crystals directly. ~ 20 mg of $Sn_{24}P_{22-x}I_8$ powder was sealed in the silica tube under vacuum with 300 mg of Red-P loaded on top of the $Sn_{24}P_{22-x}I_8$ powder. The assembly was then put into the box furnace where the reactant

end was at the center of the furnace, slowly heated up (0.5 °C/min) to 550 °C for 20 h where $\text{Sn}_{24}\text{P}_{22-x}\text{I}_8$ remained as a solid, and then rapidly cooled down (in 10 – 20 h) to 350 °C, followed by furnace quenching of the sample, the results are listed in Table 6.5. Layered square size of Black-P crystals were observed formed at the exact place of the $\text{Sn}_{24}\text{P}_{22-x}\text{I}_8$, which further proves that the model 1 should be the growth model for Black-P.

Table 6.5: Control experiments to verify the three different hypothetical growth models for Black-P

Reactants	Max. T (°C)	Black-P formation
Red-P + Black-P seed crystals	600	No
Red-P + Black-P seed crystals + I_2	600	No
Red-P + Black-P seed crystals	520	No
Red-P + Black-P seed crystals + I_2	520	No
Red-P + $\text{Sn}_{24}\text{P}_{22-x}\text{I}_8$	600	Yes
Red-P + $\text{Sn}_{24}\text{P}_{22-x}\text{I}_8$	520	Yes
Red-P + $\text{Sn}_{24}\text{P}_{22-x}\text{I}_8$	480	No

The as-grown Black-P crystals in the quartz tube are shown in Figure 6.5(a). It can be clearly seen that the Black-P crystals form at the site where the ternary clathrate $\text{Sn}_{24}\text{P}_{22-x}\text{I}_8$ originally resides, and no Black-P forms at the other end of the quartz tube, indicating the effective catalytic role of ternary clathrate $\text{Sn}_{24}\text{P}_{22-x}\text{I}_8$ for the Black-P growth. Both the optical image (Figure 6.5(b)) and SEM image (Figure 6.5(c)) indicate that these crystalline Black-P have a micro ribbon morphology with uniform thickness and width. From the side view, the well-aligned layered structure is clearly

observed, and these crystals are easily exfoliated into a layered structure as shown in the SEM image (Figure 6.5(d)). The XRD pattern shows the preferential orientation of (0k0) of the selected crystals, and the peaks are well indexed with no peaks from the $\text{Sn}_{24}\text{P}_{22-x}\text{I}_8$ phase nor other impurities are observed. The Raman spectroscopy of the crystals shows sharp peaks at 362.4, 440.2, and 466.8 cm^{-1} , which match well with the Raman shifts attributed to vibrations of the crystalline lattice of Black-P: A_g^1 (out-of-plane mode), B_{2g} (in-plane mode), and A_g^2 (in-plane mode) phonon modes.

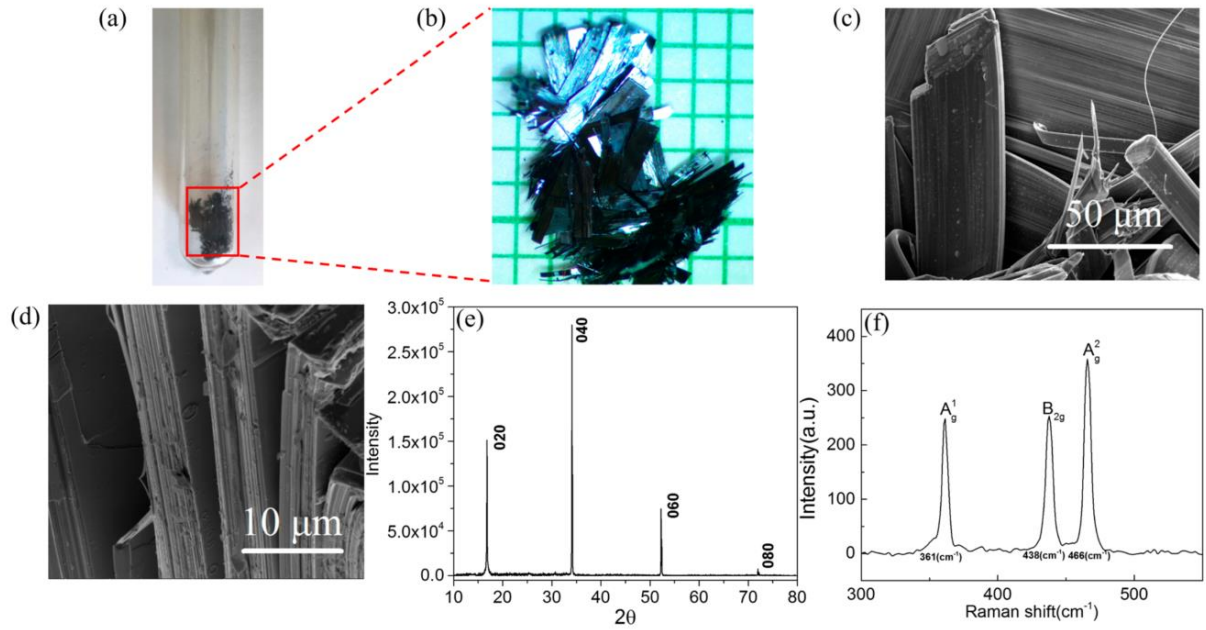


Figure 6.5: Photo of Black-P crystals in the ampule tube grown directly from ternary $\text{Sn}_{24}\text{P}_{22-x}\text{I}_8$ compound; (b) enlarged view of Black-P crystals on the mm scale. (c) Top view of SEM image of selected crystals showing ribbon-sharp morphology; (d) side view of SEM image showing the layered nature of the grown crystal. (e) XRD patterns, and (f) Raman spectrum of the grown Black-P crystals.

6.2.5 Proposed VSS model for growth of Black-P

From the aforementioned results, the roles of individual elements at different temperature stages are identified. In the growth of Black-P with elements or Sn-I binary compounds, the initial

materials of Sn, I₂, and Red-P are readily vaporized to form gaseous SnI₂, and P₄ upon heating from room temperature to 600 °C. The excess of Sn remains as a liquid at this stage but could be transported to the cold side through vapor transport reactions ($\text{Sn} + \text{I}_2 \rightarrow \text{SnI}_2$). Upon cooling, from 600 to 520 °C, these gaseous species react with each other and form the solid Sn₂₄P_{22-x}I₈ ternary phase first, and the excess of P element remains as the P₄ vapor. During this stage, the chemical vapor transport reaction does help with the formation of the solid phase of Sn₂₄P_{22-x}I₈, but no Black-P crystal has formed yet. Upon further cooling below ~ 520 °C, the P₄ vapor steadily transfers to Black-P crystals through a likely VSS mechanism via Sn₂₄P_{22-x}I₈ phase. During this stage, the Sn₂₄P_{22-x}I₈ not only provides the nucleation center for Black-P crystals but also acts as a media to transport elemental P for the continuous Black-P crystal growth. The host-guest and P-site vacancy structure features in the clathrate Sn₂₄P_{22-x}I₈ phase allow chemical reactions of P₄ vapor with the host structure where the excess P then could diffuse out from the host structure to form Black-P crystals.

In the growth of Black-P by Sn₂₄P_{22-x}I₈ catalyst, VSS is the possible growth mechanism with the evidence:

- (1) all as-grown Black-P belts attach on Sn₂₄P_{22-x}I₈ particles.
- (2) in the growth temperature of Black-P, Sn₂₄P_{22-x}I₈ is a solid.
- (3) in the lattice of Sn₂₄P_{22-x}I₈, P vacancies can vary from x₁ % to x₂ %, depending on the partial pressure of P₄. The vacancies in a solid may greatly enhance the diffusion of certain atoms in it [184].

Therefore, we have proposed that Black-P growth is governed by the VSS model, as shown in Figure 6.6. When the temperature is lower than 520 °C, Sn₂₄P_{22-x}I₈ is stable; then P₄ can decompose

at the surface of $\text{Sn}_{24}\text{P}_{22-x}\text{I}_8$ and P atoms diffuse into $\text{Sn}_{24}\text{P}_{22-x}\text{I}_8$. When the P concentration is high enough in $\text{Sn}_{24}\text{P}_{22-x}\text{I}_8$, P begins to segregate at some locations on the surface of $\text{Sn}_{24}\text{P}_{22-x}\text{I}_8$ as Black-P crystals, the most stable phase for phosphorus in thermodynamics.

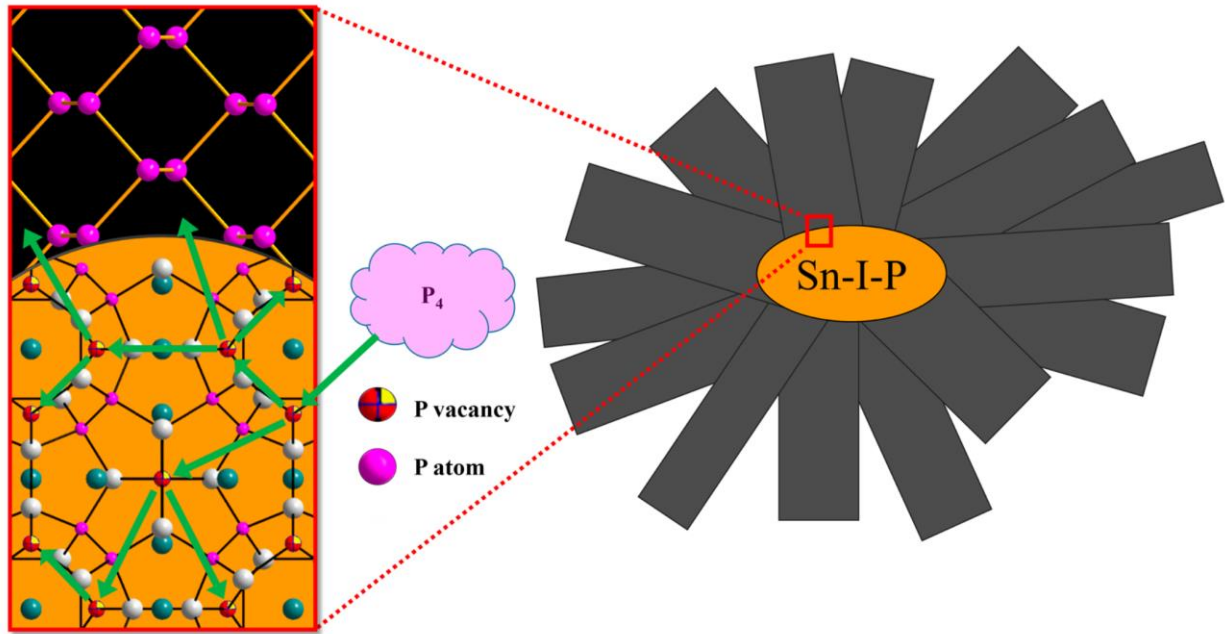


Figure 6.6: Proposed growth mechanism. The orange part represents the ternary compound of $\text{Sn}_{24}\text{P}_{22-x}\text{I}_8$; the black part represents Black-P; the purple dots represent P atoms; the colorful dots represent P vacancies; the green dots represent I atoms; and gray dots represent Sn atoms. The green arrows indicate the possible diffusion path of P atoms with the assistance of P vacancies.

CHAPTER 7

GENERAL CONCLUSIONS AND FUTURE PROSPECTS

In this dissertation, several materials with distinct quasi-1D or pseudo-quasi-1D structural features and hosting rather interesting magnetic, superconducting, and topological properties have been investigated. High quality powder or single crystals have been synthesized through various methods and characterized through XRD, EDAX, magnetic, electrical transport and thermal transport studies at low temperatures and under high magnetic fields. Their unique magnetic, superconducting, and possible topological properties are presented with their future implications further discussed.

In the first part of this dissertation, two iron-based chalcogenides with quasi-1D structure: BaFe_2Se_4 and $\text{K}_3\text{Fe}_2\text{Se}_4$, have been investigated for the magnetic properties and superconductivity. Both compounds consist of 1D chains of edge sharing FeSe_4 tetrahedra, similar to the fundamental building block FeAs_4 in the iron-based superconductors. However, the FeSe_4 in these two compounds is edge-shared forming 1D chain structure, instead of 2D Fe_2As_2 square lattice structure formed by FeAs_4 in common iron-based superconductors. XRD powder pure phases of both compounds were obtained using solid-state method and found to be semiconducting and magnetic. Intuitively chemical doping study based on the nominal iron valence states were also carried out. However, no superconductivity was detected on all doped compounds at this stage. The absence of superconductivity may due to the poor quality of the doped samples using the unoptimized synthetic method, since the XRD peaks of all doped samples are short and broad. An optimized synthetic method with optimal reaction temperature should be developed in the future.

Different charge carrier elements with similar atomic sizes of Ba / K with an accessible melting temperature can also be tested later on.

In the second part of this dissertation, the transition metals doped pseudo-quasi-1D Zr_5Ge_3 system was investigated using arc melting method, various transition metals were doped to the Zr, Ge, and interstitial sites of parent compound Zr_5Ge_3 . Interestingly, superconductivity was successfully induced through Ru and Pt doping, but only at Ge site. The highest superconducting temperature T_c of doped samples is found to be $T_c \sim 5.7$ K in $\text{Zr}_5\text{Ge}_{2.5}\text{Ru}_{0.5}$ and $T_c \sim 2.8$ K in $\text{Zr}_5\text{Ge}_{2.5}\text{Pt}_{0.5}$. Superconductivity remains absent with the same amounts of carrier doping at Zr or interstitial site. Bulk superconductivity was confirmed on both compounds through detailed transport and magnetic studies. Superconducting phase diagram was also proposed for $\text{Zr}_5\text{Ge}_{3-x}\text{Pt}_x$ system. The high upper critical field, enhanced electron correlation and extremely small electron-phonon coupling have indicated possible unconventional superconductivity in this system. In addition, we also investigated the superconducting properties of the $\text{A}_2\text{Mo}_3\text{As}_3$ ($\text{A}=\text{K}, \text{Rb}$), which also adopt a 1D chain structure that very close to Zr_5Ge_3 but has a more 1D-like Mo_3As_3 chain structure. The superconducting transition temperature T_c is ~ 10.6 K, and the electrical transport studies suggested a much higher upper critical field ~ 27 T, exceeding the Pauli limit based on conventional criteria. In many cases, the Mn_5Si_3 type materials have to bind interstitial atoms to stabilize the host structure. The extensive electron-number of A_5B_3 allows various interstitial atoms such as O, Br, C and Si. These interstitial atoms occupy the 2b site in $P6_3/mcm$ and $\text{A}_5\text{B}_3\text{Z}$ is called as the Ti_5Ga_4 -type structure or Hf_5CuSn_3 -type structure. Although the physical properties of numerous Mn_5Si_3 or Ti_5Ga_4 -type compounds have been investigated [185-188], the superconductivity is reported only in several compounds. The Nb_5Ir_3 was reported to be superconducting at 9.3 K [189] and the

oxygen added $\text{Nb}_5\text{Ir}_3\text{O}$ exhibits a rather enhanced superconducting transition temperature T_c of 10.5 K. It should be noted that this result is debatable, the reported superconductivity with $T_c \sim 9.3$ K in Nb_5Ir_3 could cause by the small Nb impurities in their samples since Nb is also superconducting at $T_c \sim 9.5$ K, or actually comes from Nb_3Ir_2 , which has the similar stoichiometric ratio of Nb : Ir to Nb_5Ir_3 and was reported to be superconducting at $T_c \sim 9.8$ K. As for Zr-based Mn_5Si_3 type compounds, the superconducting transition temperature T_c of the first superconductor in this type of family Zr_5Sb_3 is 2.3 K [190]. Zr_5Sb_3 allows interstitial oxygen atoms fully occupying the 2b site. Contrary to the enhancement of T_c in $\text{Nb}_5\text{Ir}_3\text{O}$, the added oxygen atoms reduce T_c and $\text{Zr}_5\text{Sb}_3\text{O}$ is a normal metal down to 1.8 K [190]. Another Zr-based Mn_5Si_3 compound Zr_5Pt_3 is also a superconductor at 7.2 K [191]. Very recently, the superconducting transition temperature T_c of oxygen-added $\text{Zr}_5\text{Pt}_3\text{O}_x$ is reported reduced with increasing oxygen-content (x is increased from 0 to 0.6) and down to 3.2 K in $\text{Zr}_5\text{Pt}_3\text{O}_{0.6}$ [192]. As x is further increased from 0.6 to 2.5, exceeding the full occupancy of oxygen site ($x = 1$), samples become multi-phases composed of $\text{Zr}_5\text{Pt}_3\text{O}_{\sim 0.5-0.6}$, ZrPt , and ZrO_2 . These reports show interstitial sites offer a rich playground to search for new superconductors.

We have successfully synthesized two superconductors $\text{Zr}_5\text{Ge}_{2.5}\text{Ru}_{0.5}$ and $\text{Zr}_5\text{Ge}_{2.5}\text{Pt}_{0.5}$, atoms added to the interstitial site of these compounds could change the electronic structure and may enhance the superconducting transition temperature. We tried added Si to the interstitial site of $\text{Zr}_5\text{Ge}_{2.5}\text{Ru}_{0.5}$ compound using the arc melting method. From our preliminary result of Si-added compound $\text{Zr}_5\text{Ge}_{2.5}\text{Ru}_{0.5}\text{Si}_{0.5}$, a clear superconducting transition at ~ 9.2 K was observed from $M(T)$ measurement, as shown in Figure 7.1, which is enhanced from the parent compound $\text{Zr}_5\text{Ge}_{2.5}\text{Ru}_{0.5}$ with $T_c \sim 5.7$ K. This transition temperature does not match with any reported Zr-

Ge-Ru-Si based binary, ternary or quaternary compounds, indicating possible a new superconductor was obtained. However, the superconducting volume fraction is rather small, further studies should be carried out to exam the bulk nature of this superconducting transition. Different doping levels or other interstitial atoms can also be tested to search for higher transition temperature or new superconductors in this system.

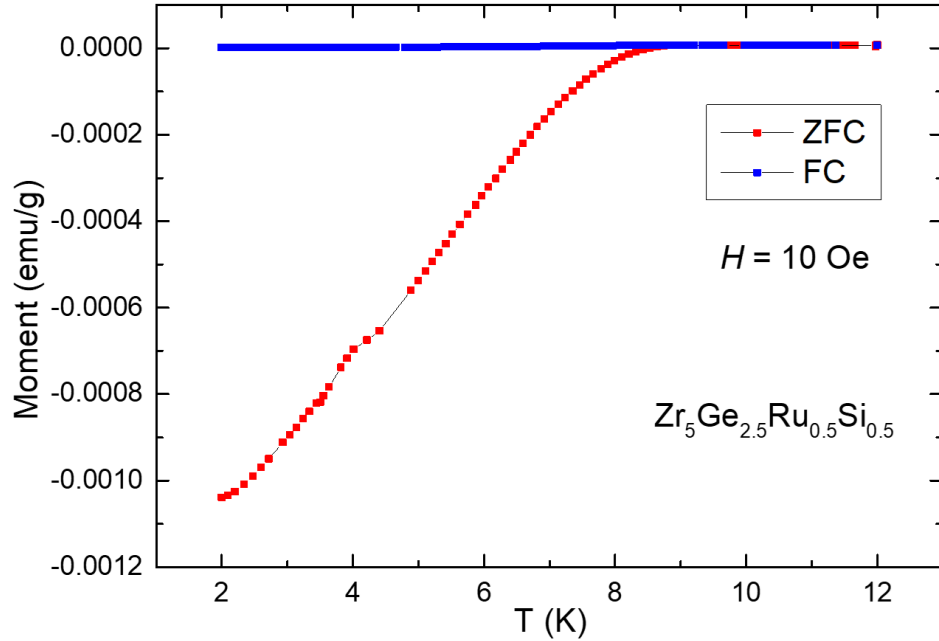


Figure 7.1: The preliminary result of dc magnetic susceptibility measurement for Si-added $\text{Zr}_5\text{Ge}_{2.5}\text{Ru}_{0.5}\text{Si}_{0.5}$ compound. The transition temperature was enhanced from 5.7 K to 9.2 K.

In the third part of this dissertation, we have presented a study of synthesis and crystal growth of α , β - Bi_4X_4 ($\text{X} = \text{I}, \text{Br}$) materials with different stacking of 1D BiX chains and various topological properties. Different growth methods have been tested for the high quality crystal growth and large Bi_4X_4 crystals (up to 10 mm) were obtained. A hypothetical VSS like growth mechanism was proposed for Bi_4Br_4 . A topological phase transition from β - Bi_4I_4 as a topological insulator to α - Bi_4I_4 with hinge state around room temperature 300 K was detected by transport measurements.

Systematical Br doping studies were also carried out in Bi_4I_4 , single crystals of mixed $\text{Bi}_4\text{I}_{4-x}\text{Br}_x$ ($0.1 \leq x \leq 3$) were synthesized to investigate the possible topological phase transition among crystals with different Br doping levels, and the chemical composition for different doping level compounds were examined by EDAX. A resistivity hysteresis around 320 K was observed on $\text{Bi}_4\text{I}_{3.9}\text{Br}_{0.1}$ crystal, indicating a structural transformation in this compound. Further studies are needed to fully understand the topological phase transitions in this system. Last but not least, chemical intercalation studies were also carried out to induce possible superconductivity in this system, our preliminary results show superconductivity was successfully induced. A clear superconducting transition at ~ 2.45 K and ~ 2.5 K were detected on Li-intercalated Bi_4I_4 and Bi_4Br_4 , respectively. However, the superconducting volume fraction is rather small on both compounds, which may due to the unoptimized intercalation method such as short soaking time or non-optimal concentration of organic solvent. Further systematical intercalation studies with an optimized method need to be developed to achieve a larger volume fraction or higher superconducting transition temperature in this system.

In the last part of this dissertation, the growth mechanism for 2D material Black-P was investigated. We carried out systematic experimental studies to investigate the growth mechanism for Black-P aiming to facilitate its future layer-by-layer thin film growth. A new synthetic strategy to grow large size of Black-P crystals through a ternary clathrate $\text{Sn}_{24}\text{P}_{22-x}\text{I}_8$ under lower temperature and pressure was reported. The chemical vapor transport mechanism was found not to play a critical role in the growth of Black-P. A new vapor-solid-solid (VSS) like growth mechanism was proposed where the ternary clathrate $\text{Sn}_{24}\text{P}_{22-x}\text{I}_8$ acts as the solid catalyst and the P vacancies in $\text{Sn}_{24}\text{P}_{22-x}\text{I}_8$ was found plays an important role in this mechanism.

REFERENCES

- [1] H. Onnes and W. Keesom, (Nov, 1911).
- [2] C. Kittel, *Introduction to solid state physics*. (Wiley New York, 1976).
- [3] W. Meissner and R. Ochsenfeld, *Naturwissenschaften* **21** (44), 787 (1933).
- [4] J. Bardeen, L. N. Cooper, and J. R. Schrieffer, *Phys. Rev.* **106** (1), 162 (1957).
- [5] L. N. Cooper, *Phys. Rev.* **104** (4), 1189 (1956).
- [6] M.-K. Wu, J. R. Ashburn, C. Torng, P. H. Hor, R. L. Meng, L. Gao et al., *Phys. Rev. Lett.* **58** (9), 908 (1987).
- [7] J. G. Bednorz and K. A. Müller, *Z. Phys. B Con. Mat.* **64** (2), 189 (1986).
- [8] Y. Kamihara, H. Hiramatsu, M. Hirano, R. Kawamura, H. Yanagi, T. Kamiya, and H. Hosono, *J. Am. Chem. Soc.* **128** (31), 10012 (2006).
- [9] Y. Kamihara, T. Watanabe, M. Hirano, and H. Hosono, *J. Am. Chem. Soc.* **130** (11), 3296 (2008).
- [10] H. Takahashi, K. Igawa, K. Arii, Y. Kamihara, M. Hirano, and H. Hosono, *Nature* **453** (7193), 376 (2008).
- [11] Z.-A. Ren, W. Lu, J. Yang, W. Yi, X.-L. Shen, Z.-C. Li et al., *arXiv preprint arXiv:0804.2053* (2008).
- [12] K. Sasmal, B. Lv, B. Lorenz, A. M. Guloy, F. Chen, Y.-Y. Xue, and C.-W. Chu, *Phys. Rev. Lett.* **101** (10), 107007 (2008).
- [13] M. Rotter, M. Tegel, and D. Johrendt, *Phys. Rev. Lett.* **101** (10), 107006 (2008).
- [14] X. Wang, Q. Liu, Y. Lv, W. Gao, L. Yang, R. Yu et al., *Solid State Commun.* **148** (11-12), 538 (2008).
- [15] J. H. Tapp, Z. Tang, B. Lv, K. Sasmal, B. Lorenz, P. C. Chu, and A. M. Guloy, *Phys. Rev. B* **78** (6), 060505 (2008).
- [16] M. J. Pitcher, D. R. Parker, P. Adamson, S. J. Herkelrath, A. T. Boothroyd, R. M. Ibberson et al., *Chem. Commun. (Cambridge, U. K.)* (45), 5918 (2008).
- [17] F.-C. Hsu, J.-Y. Luo, K.-W. Yeh, T.-K. Chen, T.-W. Huang, P. M. Wu et al., *Proc. Natl. Acad. Sci. U. S. A.* **105** (38), 14262 (2008).

- [18] S. Medvedev, T. McQueen, I. Troyan, T. Palasyuk, M. Eremets, R. J. Cava et al., *Nat. Mater.* **8** (8), 630 (2009).
- [19] J. Guo, S. Jin, G. Wang, S. Wang, K. Zhu, T. Zhou et al., *Phys. Rev. B* **82** (18), 180520 (2010).
- [20] A. Wang, J. Ying, Y. Yan, R. Liu, X. Luo, Z. Li et al., *Phys. Rev. B* **83** (6), 060512 (2011).
- [21] Y. Mizuguchi, H. Takeya, Y. Kawasaki, T. Ozaki, S. Tsuda, T. Yamaguchi, and Y. Takano, *Appl. Phys. Lett.* **98** (4), 042511 (2011).
- [22] A. Krzton-Maziopa, Z. Shermadini, E. Pomjakushina, V. Pomjakushin, M. Bendele, A. Amato et al., *J. Phys.: Condens. Matter* **23** (5), 052203 (2011).
- [23] M.-H. Fang, H.-D. Wang, C.-H. Dong, Z.-J. Li, C.-M. Feng, J. Chen, and H. Yuan, *EPL (Europhysics Letters)* **94** (2), 27009 (2011).
- [24] D. Liu, W. Zhang, D. Mou, J. He, Y.-B. Ou, Q.-Y. Wang et al., *Nat. Commun.* **3** (1), 1 (2012).
- [25] W. Qing-Yan, L. Zhi, Z. Wen-Hao, Z. Zuo-Cheng, Z. Jin-Song, L. Wei et al., *Chin. Phys. Lett.* **29** (3), 037402 (2012).
- [26] S. He, J. He, W. Zhang, L. Zhao, D. Liu, X. Liu et al., *Nat. Mater.* **12** (7), 605 (2013).
- [27] S. Tan, Y. Zhang, M. Xia, Z. Ye, F. Chen, X. Xie et al., *Nat. Mater.* **12** (7), 634 (2013).
- [28] J. Lee, F. Schmitt, R. Moore, S. Johnston, Y.-T. Cui, W. Li et al., *Nature* **515** (7526), 245 (2014).
- [29] Z. Zhang, Y.-H. Wang, Q. Song, C. Liu, R. Peng, K. Moler et al., *Science bulletin* **60** (14), 1301 (2015).
- [30] K. Miyazawa, K. Kihou, P. M. Shirage, C.-H. Lee, H. Kito, H. Eisaki, and A. Iyo, *J. Phys. Soc. Jpn.* **78** (3), 034712 (2009).
- [31] A. S. Sefat, R. Jin, M. A. McGuire, B. C. Sales, D. J. Singh, and D. Mandrus, *Phys. Rev. Lett.* **101** (11), 117004 (2008).
- [32] S. Jiang, H. Xing, G. Xuan, C. Wang, Z. Ren, C. Feng et al., *J. Phys.: Condens. Matter* **21** (38), 382203 (2009).
- [33] B. C. Sales, A. Sefat, M. A. McGuire, R. Jin, D. Mandrus, and Y. Mozharivskyj, *Phys. Rev. B* **79** (9), 094521 (2009).
- [34] R. Hu, E. S. Bozin, J. Warren, and C. Petrovic, *Phys. Rev. B* **80** (21), 214514 (2009).

- [35] Y. Mizuguchi, F. Tomioka, S. Tsuda, T. Yamaguchi, and Y. Takano, *Appl. Phys. Lett.* **94** (1), 012503 (2009).
- [36] D. Jérôme, *Science* **252** (5012), 1509 (1991).
- [37] K. Bechgaard, C. Jacobsen, K. Mortensen, H. Pedersen, and N. Thorup, *Solid State Commun.* **33** (11), 1119 (1980).
- [38] D. Jérôme, A. Mazaud, M. Ribault, and K. Bechgaard, *J. Phys. (Paris), Lett.* **41** (4), 95 (1980).
- [39] A. Hebard, M. Rosseinsky, R. Haddon, D. Murphy, S. Glarum, T. Palstra et al., *Nature* **350** (6319), 600 (1991).
- [40] K. Tanigaki, T. Ebbesen, S. Saito, J. Mizuki, J. S. Tsai, Y. Kubo, and S. Kuroshima, *Nature* **352** (6332), 222 (1991).
- [41] M. Greenblatt, W. McCarroll, R. Neifeld, M. Croft, and J. Waszczak, *Solid State Commun.* **51** (9), 671 (1984).
- [42] M. H. Whangbo and E. Canadell, *J. Am. Chem. Soc.* **110** (2), 358 (1988).
- [43] R. Chevrel, M. Sergent, and J. Prigent, *J. Solid State Chem.* **3** (4), 515 (1971).
- [44] B. T. Matthias, M. Marezio, E. Corenzwit, A. Cooper, and H. Barz, *Science* **175** (4029), 1465 (1972).
- [45] M. Marezio, P. Dernier, J. Remeika, E. Corenzwit, and B. Matthias, *Mater. Res. Bull.* **8** (6), 657 (1973).
- [46] M. Ishikawa and Ø. Fischer, *Solid State Commun.* **23** (1), 37 (1977).
- [47] D. Johnston, R. Shelton, and J. Bugaj, *Solid State Commun.* **21** (10), 949 (1977).
- [48] M. Pelizzone, A. Treyvaud, P. Spitzli, and Ø. Fischer, *J. Low Temp. Phys.* **29** (5-6), 453 (1977).
- [49] M. Sergent, Ø. Fischer, M. Decroux, C. Perrin, and R. Chevrel, *J. Solid State Chem.* **22** (1), 87 (1977).
- [50] J. Tarascon, J. Waszczak, G. Hull Jr, F. DiSalvo, and L. Blitzer, *Solid State Commun.* **47** (12), 973 (1983).
- [51] J. Tarascon, F. DiSalvo, D. Murphy, G. Hull, and J. Waszczak, *Phys. Rev. B* **29** (1), 172 (1984).

- [52] H. W. Meul, *Helv. Phys. Acta* **59** (3), 417 (1986).
- [53] O. Peña, *Physica C (Amsterdam, Neth.)* **514**, 95 (2015).
- [54] B. Seeber, M. Decroux, and Ø. Fischer, *Physica B Condens. Matter* **155** (1-3), 129 (1989).
- [55] A. P. Petrović, D. Ansermet, D. Chernyshov, M. Hoesch, D. Salloum, P. Gougeon et al., *Nat. Commun.* **7** (1), 1 (2016).
- [56] A. Petrović, R. Lortz, G. Santi, M. Decroux, H. Monnard, Ø. Fischer et al., *Phys. Rev. B* **82** (23), 235128 (2010).
- [57] M. McElfresh, *Quantum Design* **11578**, 132 (1994).
- [58] L. Fu, C. L. Kane, and E. J. Mele, *Phys. Rev. Lett.* **98** (10), 106803 (2007).
- [59] D. Hsieh, D. Qian, L. Wray, Y. Xia, Y. S. Hor, R. J. Cava, and M. Z. Hasan, *Nature* **452** (7190), 970 (2008).
- [60] M. Z. Hasan and J. E. Moore, *Annu. Rev. Condens. Matter Phys.* **2** (1), 55 (2011).
- [61] H. Zhang, C.-X. Liu, X.-L. Qi, X. Dai, Z. Fang, and S.-C. Zhang, *Nat. Phys.* **5** (6), 438 (2009).
- [62] Y. Xia, D. Qian, D. Hsieh, L. Wray, A. Pal, H. Lin et al., *Nat. Phys.* **5** (6), 398 (2009).
- [63] C.-C. Liu, J.-J. Zhou, Y. Yao, and F. Zhang, *Phys. Rev. Lett.* **116** (6), 066801 (2016).
- [64] V. I. Posypaiko and E. Alekseeva, *Phase equilibria in binary halides*. (Ifi/Plenum Data Corp, 1987).
- [65] A. R. West, *Solid state chemistry and its applications*. (John Wiley & Sons, 2014).
- [66] P. Schmidt, M. Binnewies, R. Glaum, and M. Schmidt, *Chemical vapor transport reactions—methods, materials, modeling*. (InTech Rijeka, Croatia, 2013).
- [67] P. D. File, *The Newtown Square, PA (USA)* (1995).
- [68] L. Krause, R. Herbst-Irmer, G. M. Sheldrick, and D. Stalke, *J. Appl. Crystallogr.* **48** (1), 3 (2015).
- [69] G. M. Sheldrick, *Acta Cryst. A* **71** (1), 3 (2015).
- [70] G. M. Sheldrick, *Acta Cryst. C* **71** (1), 3 (2015).
- [71] N. W. Ashcroft and N. D. Mermin, *Google Scholar* (1976).

- [72] M. McElfresh, *Quantum Design* (1994).
- [73] T. McQueen, A. Williams, P. Stephens, J. Tao, Y. Zhu, V. Ksenofontov et al., *Phys. Rev. Lett.* **103** (5), 057002 (2009).
- [74] A. Böhmer, F. Hardy, F. Eilers, D. Ernst, P. Adelman, P. Schweiss et al., *Phys. Rev. B* **87** (18), 180505 (2013).
- [75] K.-W. Yeh, T.-W. Huang, Y.-I. Huang, T.-K. Chen, F.-C. Hsu, P. M. Wu et al., *EPL (Europhysics Letters)* **84** (3), 37002 (2008).
- [76] M. Fang, H. Pham, B. Qian, T. Liu, E. Vehstedt, Y. Liu et al., *Phys. Rev. B* **78** (22), 224503 (2008).
- [77] Y. Mizuguchi, F. Tomioka, S. Tsuda, T. Yamaguchi, and Y. Takano, *J. Phys. Soc. Jpn.* **78** (7), 074712 (2009).
- [78] M. Burrard-Lucas, D. G. Free, S. J. Sedlmaier, J. D. Wright, S. J. Cassidy, Y. Hara et al., *Nat. Mater.* **12** (1), 15 (2013).
- [79] T. Ying, X. Chen, G. Wang, S. Jin, T. Zhou, X. Lai et al., *Scientific reports* **2** (1), 1 (2012).
- [80] E.-W. Scheidt, V. Hathwar, D. Schmitz, A. Dunbar, W. Scherer, F. Mayr et al., *The European Physical Journal B* **85** (8), 1 (2012).
- [81] T. Ying, X. Chen, G. Wang, S. Jin, X. Lai, T. Zhou et al., *J. Am. Chem. Soc.* **135** (8), 2951 (2013).
- [82] J. Caron, J. Neilson, D. Miller, A. Llobet, and T. McQueen, *Phys. Rev. B* **84** (18), 180409 (2011).
- [83] A. Krzton-Maziopa, E. Pomjakushina, V. Pomjakushin, D. Sheptyakov, D. Chernyshov, V. Svitlyk, and K. Conder, *J. Phys.: Condens. Matter* **23** (40), 402201 (2011).
- [84] Y. Nambu, K. Ohgushi, S. Suzuki, F. Du, M. Avdeev, Y. Uwatoko et al., *Phys. Rev. B* **85** (6), 064413 (2012).
- [85] J. Ying, H. Lei, C. Petrovic, Y. Xiao, and V. V. Struzhkin, *Phys. Rev. B* **95** (24), 241109 (2017).
- [86] H. Takahashi, A. Sugimoto, Y. Nambu, T. Yamauchi, Y. Hirata, T. Kawakami et al., *Nat. Mater.* **14** (10), 1008 (2015).
- [87] D. Berthebaud, O. Perez, J. Tobola, D. Pelloquin, and A. Maignan, *J. Solid State Chem.* **230**, 293 (2015).

- [88] W. Bronger, H. Genin, and P. Müller, *Z. Anorg. Allg. Chem.* **625** (2), 274 (1999).
- [89] S. Arrhenius, *Z. Phys. Chem. (Muenchen, Ger.)* **4** (1), 96 (1889).
- [90] S. Arrhenius, *Z. Physik. Chem* **4**, 226 (1889).
- [91] J. Gopalakrishnan and K. Nanjundaswamy, *Bull. Mater. Sci.* **5** (3-4), 287 (1983).
- [92] A. Charnukha, *J. Phys.: Condens. Matter* **26** (25), 253203 (2014).
- [93] S. Avci, O. Chmaissem, D.-Y. Chung, S. Rosenkranz, E. A. Goremychkin, J.-P. Castellán et al., *Phys. Rev. B* **85** (18), 184507 (2012).
- [94] B. Lv, X. Zhu, B. Lorenz, F. Wei, Y. Xue, Z. Yin et al., *Phys. Rev. B* **88** (13), 134520 (2013).
- [95] W. Xie, H. Luo, B. F. Phelan, and R. J. Cava, *J. Mater. Chem. C* **3** (31), 8235 (2015).
- [96] J.-K. Bao, J.-Y. Liu, C.-W. Ma, Z.-H. Meng, Z.-T. Tang, Y.-L. Sun et al., *Physical Review X* **5** (1), 011013 (2015).
- [97] Z.-T. Tang, J.-K. Bao, Y. Liu, Y.-L. Sun, A. Ablimit, H.-F. Zhai et al., *Phys. Rev. B* **91** (2), 020506 (2015).
- [98] Z.-T. Tang, J.-K. Bao, Z. Wang, H. Bai, H. Jiang, Y. Liu et al., *Sci. China Mater.* **58** (1), 16 (2015).
- [99] M. Rudometkina, Y. D. Seropegin, and E. Schvyryaeva, *J. Less. Common. Met.* **138** (2), 263 (1988).
- [100] R. Waterstrat, R. Kuentzler, and J. Muller, *J. Less. Common. Met.* **167** (1), 169 (1990).
- [101] W. Xie, H. Luo, B. F. Phelan, T. Klimczuk, F. A. Cevallos, and R. J. Cava, *Proc. Natl. Acad. Sci. U.S.A.* **112** (51), E7048 (2015).
- [102] E. Garcia and J. D. Corbett, *Inorg. Chem.* **29** (18), 3274 (1990).
- [103] J. Armici, M. Decroux, Ø. Fischer, M. Potel, R. Chevrel, and M. Sergent, *Solid State Commun.* **33** (6), 607 (1980).
- [104] M. Potel, R. Chevrel, M. Sergent, J. Armici, M. Decroux, and Ø. Fischer, *J. Solid State Chem.* **35** (2), 286 (1980).
- [105] S.-M. Huang, C.-H. Hsu, S.-Y. Xu, C.-C. Lee, S.-Y. Shiau, H. Lin, and A. Bansil, *Phys. Rev. B* **97** (1), 014510 (2018).

- [106] H. W. Meul, *Helv. Chim. Acta* **59** (3), 417 (1986).
- [107] Q.-G. Mu, B.-B. Ruan, B.-J. Pan, T. Liu, J. Yu, K. Zhao et al., *Phys. Rev. Mater.* **2** (3), 034803 (2018).
- [108] W. Xian-Xin, L. Cong-Cong, Y. Jing, F. Heng, and H. Jiang-Ping, *Chin. Phys. Lett.* **32** (5), 057401 (2015).
- [109] J. Hu, *Sci. Bull.* **60** (24), 2140 (2015).
- [110] T. Kong, S. L. Bud'ko, and P. C. Canfield, *Phys. Rev. B* **91** (2), 020507 (2015).
- [111] K. Zhao, Q.-G. Mu, T. Liu, B.-J. Pan, B.-B. Ruan, L. Shan et al., *arXiv preprint arXiv:1805.11577* (2018).
- [112] X. Wu, F. Yang, C. Le, H. Fan, and J. Hu, *Phys. Rev. B* **92** (10), 104511 (2015).
- [113] J. Yang, Z. Tang, G. Cao, and G.-q. Zheng, *Phys. Rev. Lett.* **115** (14), 147002 (2015).
- [114] H. Zhong, X.-Y. Feng, H. Chen, and J. Dai, *Phys. Rev. Lett.* **115** (22), 227001 (2015).
- [115] Y. Zhou, C. Cao, and F.-C. Zhang, *arXiv preprint arXiv:1502.03928* (2015).
- [116] Q.-G. Mu, B.-B. Ruan, B.-J. Pan, T. Liu, J. Yu, K. Zhao et al., *Phys. Rev. B* **96** (14), 140504 (2017).
- [117] T. Liu, Q.-G. Mu, B.-J. Pan, J. Yu, B.-B. Ruan, K. Zhao et al., *EPL (Europhysics Letters)* **120** (2), 27006 (2018).
- [118] Q.-G. Mu, B.-B. Ruan, K. Zhao, B.-J. Pan, T. Liu, L. Shan et al., *Sci. Bull.* **63** (15), 952 (2018).
- [119] G. Autès, A. Isaeva, L. Moreschini, J. C. Johannsen, A. Pisoni, R. Mori et al., *Nat. Mater.* **15** (2), 154 (2016).
- [120] F. Tang, H. C. Po, A. Vishwanath, and X. Wan, *Nat. Phys.* **15** (5), 470 (2019).
- [121] J.-J. Zhou, W. Feng, C.-C. Liu, S. Guan, and Y. Yao, *Nano Lett.* **14** (8), 4767 (2014).
- [122] C.-H. Hsu, X. Zhou, Q. Ma, N. Gedik, A. Bansil, V. M. Pereira et al., *2D Materials* **6** (3), 031004 (2019).
- [123] R. Noguchi, T. Takahashi, K. Kuroda, M. Ochi, T. Shirasawa, M. Sakano et al., *Nature* **566** (7745), 518 (2019).

- [124] H. G. von Schnering, H. von Benda, and C. Kalveram, *Z. Anorg. Allg. Chem.* **438** (1), 37 (1978).
- [125] H. von Benda, A. Simon, and W. Bauhofer, *Z. Anorg. Allg. Chem.* **438** (1), 53 (1978).
- [126] E. Dikarev, B. Popovkin, and A. Shevelkov, *Russ. Chem. Bull.* **50** (12), 2304 (2001).
- [127] T. Filatova, P. Gurin, L. Kloo, V. Kulbachinskii, A. Kuznetsov, V. Kytin et al., *J. Solid State Chem.* **180** (3), 1103 (2007).
- [128] A. Pisoni, R. Gaál, A. Zeugner, V. Falkowski, A. Isaeva, H. Huppertz et al., *Phys. Rev. B* **95** (23), 235149 (2017).
- [129] X. Li, D. Chen, M. Jin, D. Ma, Y. Ge, J. Sun et al., *Proc. Natl. Acad. Sci. U. S. A.* **116** (36), 17696 (2019).
- [130] J. C. Teo and T. L. Hughes, *Phys. Rev. Lett.* **111** (4), 047006 (2013).
- [131] Y. Ueno, A. Yamakage, Y. Tanaka, and M. Sato, *Phys. Rev. Lett.* **111** (8), 087002 (2013).
- [132] F. Zhang, C. Kane, and E. Mele, *Phys. Rev. Lett.* **111** (5), 056403 (2013).
- [133] F. A. Lévy, *Intercalated layered materials*. (Springer Science & Business Media, 2012).
- [134] R. Friend and A. Yoffe, *Adv. Phys.* **36** (1), 1 (1987).
- [135] X.-L. Li and Y.-D. Li, *J. Phys. Chem. B* **108** (37), 13893 (2004).
- [136] A. Ambrosi, Z. Sofer, and M. Pumera, *Small* **11** (5), 605 (2015).
- [137] K. Takada, H. Sakurai, E. Takayama-Muromachi, F. Izumi, R. A. Dilanian, and T. Sasaki, *Nature* **422** (6927), 53 (2003).
- [138] S. Yamanaka, K.-i. Hotehama, and H. Kawaji, *Nature* **392** (6676), 580 (1998).
- [139] N. Emery, C. Hérold, J.-F. Marêché, and P. Lagrange, *Sci. Technol. Adv. Mat.* **9** (4), 044102 (2009).
- [140] R. A. Klemm, *Physica C (Amsterdam, Neth.)* **514**, 86 (2015).
- [141] R. Zhang, I.-L. Tsai, J. Chapman, E. Khestanova, J. Waters, and I. V. Grigorieva, *Nano Lett.* **16** (1), 629 (2016).
- [142] E. Morosan, H. W. Zandbergen, B. Dennis, J. Bos, Y. Onose, T. Klimczuk et al., *Nat. Phys.* **2** (8), 544 (2006).

- [143] X. Miao, S. Nishiyama, L. Zheng, H. Goto, R. Eguchi, H. Ota et al., *Sci. Rep.* **6**, 29292 (2016).
- [144] K. Sato, T. Noji, T. Hatakeda, T. Kawamata, M. Kato, and Y. Koike, *J. Phys. Soc. Jpn.* **86** (10), 104701 (2017).
- [145] K. Sato, T. Noji, T. Hatakeda, T. Kawamata, M. Kato, and Y. Koike, *J. Phys. Soc. Jpn.* **87** (5), 054704 (2018).
- [146] K. S. Novoselov, A. K. Geim, S. Morozov, D. Jiang, M. I. Katsnelson, I. Grigorieva et al., *Nature* **438** (7065), 197 (2005).
- [147] C. Tan, X. Cao, X.-J. Wu, Q. He, J. Yang, X. Zhang et al., *Chem. Rev.* **117** (9), 6225 (2017).
- [148] A. K. Geim and K. S. Novoselov, in *Nanoscience and technology: a collection of reviews from nature journals* (World Scientific, 2010), pp. 11.
- [149] A. K. Geim, *Science* **324** (5934), 1530 (2009).
- [150] F. Bonaccorso, Z. Sun, T. Hasan, and A. Ferrari, *Nat. Photonics* **4** (9), 611 (2010).
- [151] M. Xu, T. Liang, M. Shi, and H. Chen, *Chem. Rev.* **113** (5), 3766 (2013).
- [152] Q. H. Wang, K. Kalantar-Zadeh, A. Kis, J. N. Coleman, and M. S. Strano, *Nat. Nanotechnol.* **7** (11), 699 (2012).
- [153] V. K. Sangwan, D. Jariwala, I. S. Kim, K.-S. Chen, T. J. Marks, L. J. Lauhon, and M. C. Hersam, *Nat. Nanotechnol.* **10** (5), 403 (2015).
- [154] Q. Tang and Z. Zhou, *Prog. Mater.* **58** (8), 1244 (2013).
- [155] X. Ling, H. Wang, S. Huang, F. Xia, and M. S. Dresselhaus, *Proc. Natl. Acad. Sci. U. S. A.* **112** (15), 4523 (2015).
- [156] H. Liu, Y. Du, Y. Deng, and D. Y. Peide, *Chem. Soc. Rev.* **44** (9), 2732 (2015).
- [157] V. Eswaraiyah, Q. Zeng, Y. Long, and Z. Liu, *Small* **12** (26), 3480 (2016).
- [158] A. Castellanos-Gomez, *J. Phys. Chem. Lett.* **6** (21), 4280 (2015).
- [159] L. Kou, C. Chen, and S. C. Smith, *J. Phys. Chem. Lett.* **6** (14), 2794 (2015).
- [160] V. Sorkin, Y. Cai, Z. Ong, G. Zhang, and Y.-W. Zhang, *Crit. Rev. Solid State Mater. Sci.* **42** (1), 1 (2017).

- [161] P. Bridgman, *J. Am. Chem. Soc.* **36** (7), 1344 (1914).
- [162] H. Liu, A. T. Neal, Z. Zhu, Z. Luo, X. Xu, D. Tománek, and P. D. Ye, *ACS Nano* **8** (4), 4033 (2014).
- [163] M. Long, A. Gao, P. Wang, H. Xia, C. Ott, C. Pan et al., *Sci. Adv.* **3** (6), e1700589 (2017).
- [164] M. Zhu, Y. Osakada, S. Kim, M. Fujitsuka, and T. Majima, *Appl. Catal. B Environ.* **217**, 285 (2017).
- [165] P. Bridgman, *Phys. Rev.* **48** (11), 893 (1935).
- [166] P. W. Bridgman, presented at the Proc. Am. Acad. Arts Sci., 1937 (unpublished).
- [167] Y. Maruyama, S. Suzuki, K. Kobayashi, and S. Tanuma, *Physica B+ c* **105** (1-3), 99 (1981).
- [168] A. Brown and S. Rundqvist, *Acta Crystallogr.* **19** (4), 684 (1965).
- [169] S. Lange, P. Schmidt, and T. Nilges, *Inorg. Chem.* **46** (10), 4028 (2007).
- [170] T. Nilges, M. Kersting, and T. Pfeifer, *J. Solid State Chem.* **181** (8), 1707 (2008).
- [171] M. Köpf, N. Eckstein, D. Pfister, C. Grotz, I. Krüger, M. Greiwe et al., *J. Cryst. Growth* **405**, 6 (2014).
- [172] M. Zhao, H. Qian, X. Niu, W. Wang, L. Guan, J. Sha, and Y. Wang, *Cryst. Growth Des.* **16** (2), 1096 (2016).
- [173] C.-Y. Wen, M. Reuter, J. Bruley, J. Tersoff, S. Kodambaka, E. Stach, and F. Ross, *Science* **326** (5957), 1247 (2009).
- [174] Y.-C. Chou, C.-Y. Wen, M. C. Reuter, D. Su, E. A. Stach, and F. M. Ross, *ACS Nano* **6** (7), 6407 (2012).
- [175] J. E. Allen, E. R. Hemesath, D. E. Perea, J. L. Lensch-Falk, Z. Li, F. Yin et al., *Nat. Nanotechnol.* **3** (3), 168 (2008).
- [176] Y. Wang, V. Schmidt, S. Senz, and U. Gösele, *Nat. Nanotechnol.* **1** (3), 186 (2006).
- [177] S. Noor Mohammad, *J. Chem. Phys.* **131** (22), 224702 (2009).
- [178] H. Cui, Y. Lu, G. Yang, Y. Chen, and C. Wang, *Nano Lett.* **15** (5), 3640 (2015).
- [179] M. M. Shatruk, K. A. Kovnir, A. V. Shevelkov, I. A. Presniakov, and B. A. Popovkin, *Inorg. Chem.* **38** (15), 3455 (1999).

- [180] V. V. Novikov, A. V. Matovnikov, D. V. Avdashchenko, N. V. Mitroshenkov, E. Dikarev, S. Takamizawa et al., *J. Alloys Compd.* **520**, 174 (2012).
- [181] M. A. Kirsanova and A. V. Shevelkov, *Z. Kristallogr. - Cryst. Mater.* **228** (5), 215 (2013).
- [182] D. Pfister, K. Schäfer, C. Ott, B. Gerke, R. Pöttgen, O. Janka et al., *Adv. Mater.* **28** (44), 9783 (2016).
- [183] J. Lipkowski, *Annu. Rep. Prog. Chem., Sect. C: Phys. Chem.* **92**, 307 (1995).
- [184] E. Boehm, J.-M. Bassat, P. Dordor, F. Mauvy, J.-C. Grenier, and P. Stevens, *Solid State Ionics* **176** (37-38), 2717 (2005).
- [185] C. Zheng, H. Mattausch, and A. Simon, *J. Alloys Compd.* **347** (1-2), 79 (2002).
- [186] C. Sürgers, M. Gajdzik, G. v. Fischer, H. v. Löhneysen, E. Welter, and K. Attenkofer, *Phys. Rev. B* **68** (17), 174423 (2003).
- [187] A. Mar, O. Tougait, M. Potel, H. Noël, and E. B. Lopes, *Chem. Mater.* **18** (18), 4533 (2006).
- [188] V. Goruganti, K. Rathnayaka, and J. H. Ross Jr, *J. Appl. Phys.* **105** (7), 07E118 (2009).
- [189] Y. Zhang, B. Wang, Z. Xiao, Y. Lu, T. Kamiya, Y. Uwatoko et al., (DOI).
- [190] B. Lv, X. Zhu, B. Lorenz, F. Wei, Y. Xue, Z. Yin et al., *Phys. Rev. B* **88** (13), 134520 (2013).
- [191] R. Waterstrat, R. Kuentzler, and J. Muller, *J. Less-Common Met.* **167** (1), 169 (1990).
- [192] S. Hamamoto and J. Kitagawa, *Mater. Res. Express* **5** (10), 106001 (2018).

BIOGRAPHICAL SKETCH

Xiaoyuan Liu was born in Jian, Jiangxi Province, China in May 1992 and raised in Shenzhen, Guangdong Province, China. After completing his classwork in The Affiliated High School of Shenzhen University in Shenzhen in 2010, he attended University of Science and Technology of China (USTC) in Hefei, Anhui Province, China. He received a Bachelor of Science with a major in Applied Physics in 2014. He entered The University of Texas at Dallas in Richardson, Texas to pursue a PhD in Physics in 2014, and received a Master of Science in Physics in 2016.

CURRICULUM VITAE

Xiaoyuan Liu

CONTACT INFORMATION

Department of Physics
The University of Texas at Dallas
800 W. Campbell Rd.
Richardson, TX 75080-3021, U. S. A.
Email: xxl147030@utdallas.edu

EDUCATION

- 2010 – 2014 **BS in Physics**, University of Science and Technology of China – Hefei, Anhui, China
- 2014 – 2016 **MS in Physics**, The University of Texas at Dallas – Dallas, Texas, United States
- 2016 – 2020 **PhD candidate in Physics**, The University of Texas at Dallas – Dallas, Texas, United States

RESEARCH EXPERIENCE

- 2013 Summer, Laboratory of Plasma Physics of USTC

Experimental measurement and Analysis of magnetized sheet plasma

- 2014 – 2016, Dr. Chuanwei Zhang's group at UT Dallas

Theoretical calculation and analysis modeling for Bose-Einstein Condensates in low dimensions

- 2016 – 2020, Dr. Bing Lv's lab at UT Dallas

Our study is mainly focused on searching for new superconductors, 2D materials, high thermal conductivity materials and topological materials. My research in Black Phosphorus growth mechanism investigation has led to a published paper in the cover letter of Crystal growth & design in 2017. Research in Searching for new superconductors in Zr_5Ge_3 system has led to two published papers in New Journal of Physics and Superconductor Science and Technology in 2017 and 2018. Research in synthesis of high thermal conductivity Boron Arsenide and Boron Phosphide has led to a paper in Science and a paper in Advanced function materials in 2018. Our work in high thermal conductivity Boron Arsenide has stimulated extensive interest in the condense matter community.

RELEVANT COURSEWORK

- **Physics:** Mechanics, Electromagnetism, Thermal Physics, Optics, Atomic Physics, Classical Mechanics, Electrodynamics, Quantum Mechanics, Thermodynamics and Statistical Physics, Solid State Physics.
- **Math:** Calculus, Complex Variables, Probability Theory and Mathematical Statistics, Mathematical Physics, Math Methods of Physics.
- **Programming:** Programming in C, Scientific Computing.

PUBLICATION LISTS

1. **Xiaoyuan Liu**[#], Sheng Li[#], X. Fan, Y. Ni, J. Miracle, N. Theodoropoulou, J. Sun, S. Chen. Bing Lv*, and Q. K. Yu*, "New strategy for black phosphorus crystal growth through ternary clathrate", *Cryst. Growth Des.* 17(12), 6579 (2017) (# The first two authors contributed equally to this work).
2. Sheng Li, **Xiaoyuan Liu**, Varun Anand, Bing Lv*, "Superconductivity from site-selective Ru doping studies in Zr₅Ge₃ system", *New. J. Phys.* 20, 013009 (2018).
3. Sheng Li, **Xiaoyuan Liu**, Varun Anand, Bing Lv*, "Superconductivity and phase diagram in a transition metal doped Zr₅Ge₃ compound", *Supercond. Sci. Technol.* 31, 085001 (2018).
4. Sheng Li, Qiye Zheng, Yinchuan Lv, **Xiaoyuan Liu**, Xiqu Wang, Pinshane Y. Huang, David G. Cahill*, and Bing Lv*, "High Thermal Conductivity in Cubic Boron Arsenide Crystals", *Science*, 361, 579 (2018).
5. Qiye Zheng, Sheng Li, Chunhua Li, Yinchuan Lv, **Xiaoyuan Liu**, David Broido, Pinshane Y. Huang, Bing Lv*, and David G. Cahill*, "High thermal conductivity in the isotopically enriched cubic boron phosphide", *Adv. Funct. Mater.* 28, 1805116 (2018).
6. Sheng Li, Keith M. Taddei, Xiqu Wang, Hanlin Wu, Jorg Neuefeind, Davis Zackaria, **Xiaoyuan Liu**, Clarina Dela Cruz, and Bing Lv*, "Thermal expansion coefficients of high thermal conducting BAs and BP materials", *Appl. Phys. Lett.* 115, 011901 (2019).
7. Sheng Li, **Xiaoyuan Liu**, Maurice Sorolla, II, Gregory T. McCandless, Hanlin Wu, Huifei Zhai, Julia Y. Chan, and BingLv*, "Synthesis and structure of a nonstoichiometric Zr_{3.55}Pt₄Sb₄ compound", *Inorg. Chem.* 58, 12017 (2019).

SKILLS

- Software: C, Matlab, LaTeX, Origin Pro, Jade, Diamond, Microsoft office
- High quality material synthesis and crystals growth through various methods (e. g. Solid-State Reaction, Chemical Vapor Transport Reaction, Flux Growth, Arc Melting Technique, Chemical Vapor Deposition Reaction)
- Manipulation of various chemicals within special environments (e.g. Glovebox, Cleanroom)
- Materials characterization using various equipment (e. g. X-ray diffractometer, Scanning Electron Microscope, Energy Dispersive X-ray Spectroscopy, Physical Property Measurement System, Magnetic Property Measurement System)

AWARDS

- 2016 Margie Renfrow Scholarship (UTD)
- 2010 & 2013 Scholarship of USTC
- 2010 First Prize in National High School Students Physics Contest (China)

PROFESSIONAL MEMBERSHIP

- American Physics Society (APS), 2016 – present

CONTRIBUTED PRESENTATIONS

1. **Xiaoyuan Liu**, Sheng Li, Qingkai Yu, Bing Lv, “Synthesis and growth mechanism investigation for black phosphorus”, APS March 2017 National Meeting, New Orleans, LA, United States, March 13-17, 2017.
2. Sheng Li, **Xiaoyuan Liu**, Varun Anand, Bing Lv, “Doping studies and superconductivity in the transition metal doped Zr_5Ge_3 system”, APS March 2017 National Meeting, New Orleans, LA, United States, March 13-17, 2017.
3. **Xiaoyuan Liu**, Sheng Li, Varun Anand, Bing Lv, “Doping studies and superconductivity in Ru-doped Zr_5Ge_3 system”, APS Texas 2017 Meeting, Dallas, TX, United States, October 20-21, 2017.
4. Sheng Li, Qiye Zheng, Yinchuan Lv, **Xiaoyuan Liu**, Xiqu Wang, Pinshane Y. Huang, David G. Cahill*, and Bing Lv*, “Synthesis and high thermal conductivity in cubic BAs and BP crystals”, APS Texas 2017 Meeting, Dallas, TX, United States, October 20-21, 2017.
5. Sheng Li, Qiye Zheng, Yinchuan Lv, **Xiaoyuan Liu**, Xiqu Wang, Pinshane Y. Huang, David G. Cahill*, and Bing Lv*, “Crystal growth, and high thermal conductivity in cubic zinc-blende BAs and BP”, APS March 2018 National Meeting, Los Angeles, CA, United States, March 5-9, 2018.
6. **Xiaoyuan Liu**, Sheng Li, Varun Anand, Bing Lv, “Superconductivity and phase diagram in a transition metal doped Zr_5Ge_3 compound”, APS March 2019 National Meeting, Boston, MA, United States, March 4-8, 2019.
7. Sheng Li, Qiye Zheng, Yinchuan Lv, **Xiaoyuan Liu**, Xiqu Wang, Pinshane Y. Huang, David G. Cahill*, and Bing Lv*, “High thermal conductivity in cubic arsenide crystals”, APS March 2019 National Meeting, Boston, MA, United States, March 4-8, 2019.
8. Yulu Liu, Ruoyu Chen, Sheng Li, **Xiaoyuan Liu**, Takashi Taniguchi, Kenji Watanabe, Bing Lv*, Fan Zhang*, and Chun Ning Lau*, “Electronic properties of Bismuth Iodide (Bi_4I_4)”, APS March 2019 National Meeting, Boston, MA, United States, March 4-8, 2019.